HIGHLY PARALLEL MAGNETIC RESONANCE IMAGING WITH A FOURTH GRADIENT CHANNEL FOR COMPENSATION OF RF PHASE PATTERNS

A Dissertation

by

JOHN CARL BOSSHARD

Submitted to the Office of Graduate Studies of
Texas A&M University
in partial fulfillment of the requirements for the degree of

DOCTOR OF PHILOSOPHY

Approved by:

Chair of Committee,	Steven M. Wright
Committee Members,	Mary P. McDougall
	Jim Xiuquan Ji
	Robert D. Nevels
Head of Department,	Costas N. Georghiades

December 2012

Major Subject: Electrical Engineering

ABSTRACT

A fourth gradient channel was implemented to provide slice dependent RF coil phase compensation for arrays in dual-sided or “sandwich” configurations. The use of highly parallel arrays for single echo acquisition magnetic resonance imaging allows both highly accelerated imaging and capture of dynamic and single shot events otherwise inaccessible to MRI. When using RF coils with dimensions on the order of the voxel size, the array coil element phase patterns adversely affect image acquisition, requiring correction. This has previously been accomplished using a pulse of the gradient coil, imparting a linear phase gradient across the sample opposite of that due to the RF coil elements. However, the phase gradient due to the coil elements reverses on opposite sides of the coils, preventing gradient-based phase compensation with sandwich arrays. To utilize such arrays, which extend the imaging field of view of this technique, a fourth gradient channel and coil were implemented to simultaneously provide phase compensation of opposite magnitude to the lower and upper regions of a sample, imparting opposite phase gradients to compensate for the opposite RF coil phase patterns of the arrays.

The fourth gradient coil was designed using a target field approach and constructed using printed circuit boards. This coil was integrated with an RF excitation coil, dual-sided receive array, and sample loading platform to form a single imaging probe capable of both ultra-fast and high resolution magnetic resonance imaging. By employing the gradient coil, this probe was shown to simultaneously provide improved

phase compensation throughout a sample, enabling simultaneous SEA imaging using arrays placed below and above a sample. The fourth gradient coil also improves the acquisition efficiency of highly accelerated imaging using both arrays for receive. The same imaging probe was shown to facilitate accelerated MR microscopy over the field of view of the entire array with no changes to the hardware configuration. The spatio-temporal imaging capabilities of this system were explored with magnetic resonance elastography.

Ad Iesum per Mariam

ACKNOWLEDGEMENTS

I acknowledge my mother and father for the sacrifices they made in raising me, for their constant love, and for providing the opportunity for me to have a world-class education. I thank them most for preserving and transmitting to me the Catholic and Apostolic faith, which alone sustains me. Also important are the vast life skills I learned from both of them, aiding in my work and helping in my relationships with others. Working with and learning from my father has provided the foundation of any technical skills I have. I also thank my brother for his friendship and for many good conversations.

I gratefully acknowledge Dr. Steve Wright for sharing his scientific and technical expertise, along with the benefits of his vast experience. I am especially grateful for his patience with me in carrying out this work. The Magnetic Resonance Systems Laboratory at Texas A&M is a unique and privileged environment for exploring the technical aspects of MRI. Building this lab has taken years of dedicated work by Dr. Wright along with the efforts of his many past and current students, all of whom are acknowledged. Dr. Mary McDougall is also acknowledged for her contribution to the development of SEA imaging on which this work is based and for co-developing this project. I acknowledge my current and past labmates for our many enjoyable conversations.

Lastly, I acknowledge Rev. David Konderla of St. Mary's Catholic Center for serving as my pastor and spiritual father for these years.

TABLE OF CONTENTS

Page

LIST OF FIGURES

1. INTRODUCTION

The need to non-invasively see inside the human body for diagnosis of disease has led to the advent and development of spatially localized nuclear magnetic resonance, referred to as Magnetic Resonance Imaging or MRI. Over the past thirty years this imaging method has matured, becoming a routine diagnostic tool in most hospitals in developed countries. As costs have come down, there is increased interest in using MRI for non-clinical applications, such as in measurement of flow [1, 2], in non-destructive testing of agricultural products [3], in study of porous media [4], and for histology [5]. While the clinical interest in MRI has centered around its ability to image non-invasively, non-clinical applications such as MR microscopy may benefit most from the range of contrast available [6], such as relaxation times and chemical shift.

There is a degree of mutual enrichment that occurs between the advancement of MRI technology and the rise of new applications. For instance, the development of functional magnetic resonance imaging which is capable of detecting and localizing brain activation benefited from the image quality provided by homogeneous superconducting magnets and the acquisition speeds enabled by advancements in gradient technology. Highly parallel MRI using an array of detection coils and receiver channels likewise allows access to imaging modes otherwise impossible or inaccessible. Our group has developed technology to explore this area, capturing MR images in a single echo [7] and performing highly accelerated MR microscopy over a wide field of view [8]. One of the complications arising in this method is the influence of the phase

patterns of the RF coils on the acquired images [9, 10]. While the vast majority of MRI scanners utilize three independent gradient channels, this work investigates the use of a fourth gradient channel specifically for compensation of RF coil phase patterns, extending single echo acquisition and highly accelerated imaging techniques to dual-planar arrays placed above and below a sample. A probe was developed allowing use of dual-planar or "sandwich" arrays over a range of spatio-temporal regimes, from single echo imaging to microscopy.

1.1 Parallel MRI

Fast imaging sequences such as fast low angle shot (FLASH) [11], echo planar imaging (EPI) [12], and those employing spiral *k*-space trajectories [13] accelerate image acquisition by manipulation of the physics of MRI [14]. By using fast switching magnetic field gradients, more data is acquired per excitation, allowing collection of a complete image in times on the order of milliseconds. There are however both hardware, and in clinical imaging, physiological constraints limiting this method of acceleration. Fast switching is only possible using gradient coils of low inductance and stored energy. Such coils with low efficiencies require amplifiers capable of switching high currents and voltages [15]. Physiological limits of fast switched gradients arise due to peripheral nerve stimulation [16], in which the time changing magnetic fields of the gradient coils stimulate nerves causing patient discomfort and inducing motion.

Parallel MRI describes a method by which data is simultaneously acquired using multiple RF detector coils [17, 18]. In the implementation of the "NMR Phased Array" described by Rohmer et al., signals from an array of decoupled RF coils are combined

such that the signal to noise ratio benefit arising from the use of surface coils is retained without the loss of field of view associated with smaller coils [19]. Parallel MRI takes advantage of the additional information arising from the spatially confined field patterns of each of the surface coils to supplement or entirely eliminate gradient encoding. As gradient encoding is a time consuming process, reducing the number of encoding steps necessary to fully reconstruct an image allows reduction of scan time, as the time between encoding steps is dependent on the relaxation time of the sample. The concept of using spatial information from multiple coils to partially eliminate gradient encoding was noted early in the MR literature [20, 21]. Also an early approach to eliminate phase encoding altogether using an array of coils was proposed by Hutchinson and Raff [22], although it was only tested in software. The publication of the Simultaneous Acquisition of Spatial Harmonics (SMASH) by Sodickson and Manning [23] and Sensitivity Encoding (SENSE) [24] by Pruessmann et al. opened the way for partially parallel MRI to become standard in clinical scanners, making image accelerations of a factor of two or more standard practice.

Single Echo Acquisition (SEA) [7] was demonstrated by our group in 2002 as completely parallel MR imaging method in which an array of 64 narrow coils, each responsible for imaging the region of the sample directly above it, and a 64 channel receiver are used to obtain an MR image in a single echo by eliminating gradient phase encoding steps entirely. This has been used to capture dynamic processes such as non-periodic flow [25-27] and in highly accelerated MR elastography [28, 29]. The highly parallel nature of the 64 channel array and receiver also allows simultaneous collection

of MR microscopy images from each array element. By combining these high resolution images, an MR microscopy image is obtained over the field of view of the entire array while only requiring enough gradient spatial encoding to cover the field of view of one array element [8].

1.2 RF Coil Phase

One complication that arises in SEA imaging is the necessity to correct for the phase gradient due to the RF coil elements. As the imaged voxels approach the dimension of the array coil elements, the RF phase gradient due to the coils causes cancellation of the signals received from each voxel or volume element. In order to obtain a SEA image this phase gradient must be corrected, which has hitherto been accomplished by applying a pulse from the main gradient coil of the MR scanner [9]. The gradient pulse creates a linear phase gradient across the voxel approximately opposite of that caused by the RF coil, restoring the lost signal. However, the RF coil phase gradient varies with distance from the coils and reverses on opposite sides of dual-sided receive arrays [10], precluding the use of a single gradient pulse to simultaneously correct for RF coil phase for both sides of a dual-sided array.

1.3 Dissertation Organization

This dissertation describes the implementation of an imaging platform incorporating a highly parallel dual-sided RF coil array for receive and an independent fourth gradient coil and output channel for compensation of RF coil phase patterns of dual-sided arrays. This platform is used for imaging over a range of spatio-temporal regimes, from single echo acquisition and highly accelerated imaging to MR

microscopy. After this Introduction section, the second section entitled Background discusses some of the theoretical framework necessary to understand parallel MRI and the problem of phase gradients due to RF coils and how the brief application of a gradient in the magnetic field can be used to compensate. The problem of using the main gradient coil for phase compensation for a dual-sided array is developed and some of the benefits of highly parallel imaging are discussed. The third section entitled Fourth Gradient Coil shows how a non-standard gradient in the main magnetic field can produce a phase gradient in the sample compensating for RF coil phase of dual-sided arrays. The process of developing a prototype gradient coil capable of generating the desired phase distribution is discussed, with calculated fields of uniplanar and biplanar coils shown along with some measurements. A significant limitation in this approach is also treated in this section. The fourth section entitled Wide Field of View Imaging System presents the prototype imaging probe with integrated fourth gradient coil, volume excitation coil, and receive array. The system which controls the fourth gradient coil is shown, along with results obtained from a phantom and assessment of performance. Applications, the fifth section, discusses the spatio-temporal capabilities of the system, discusses several potential applications, and shows its use in magnetic resonance elastography. Finally, the sixth section entitled Conclusions reviews the capabilities of this imaging platform as well as possible future work.

2. BACKGROUND

2.1 Magnetic Resonance Imaging

The concept of using nuclear magnetic resonance (NMR) to form tomographic images was first reported by Paul Lauterbur in 1973 [30]. Lauterbur noted that by introducing a linear gradient in the magnetic field of an NMR spectrometer, spatial location could be mapped onto the frequency spectrum of the response from a sample. This proceeds from the Larmor relationship in NMR between the resonant frequency of a sample and the external static magnetic field

$$\omega = \gamma B_0$$

where ω is the frequency in rad/s, γ is the gyromagnetic ratio (2π x 42.57 x 10^6 rad/T for hydrogen), and B_0 is the external static magnetic field strength. The first application of this imaging technique involved taking several projections, each with a different angle between the field gradient and sample, and forming an image by back projection. Later, more advanced Fourier encoding techniques were developed.

2.1.1 Gradient Encoding and k-space

Typical MRI scanners employ a three axis linear gradient system capable of creating a gradient in the main z-directed magnetic field B_0 along the x, y, and z directions. The three gradient fields can be expressed as

$$G_x = \frac{\partial B_z}{\partial x}, \qquad G_y = \frac{\partial B_z}{\partial y}, \qquad G_z = \frac{\partial B_z}{\partial z},$$

where B_z is the z component of the magnetic field produced by the x, y, or z "gradient coil" and G is the gradient field, conventionally expressed in G/cm or mT/m. In the presence of these gradient fields, the Larmor frequency acquires a position dependence given by

$$\omega(x, y, z) = \gamma\left(B_0 + G_x x + G_y y + G_z z\right)$$

such that the frequency at a point (x, y, z) is due to the sum of the static and gradient magnetic fields. Imaging is performed using a pulse sequence which precisely controls the timing of the gradient and RF pulses as well as the reception and sampling of the response. A typical spin-echo pulse sequence is shown in Fig. 1.

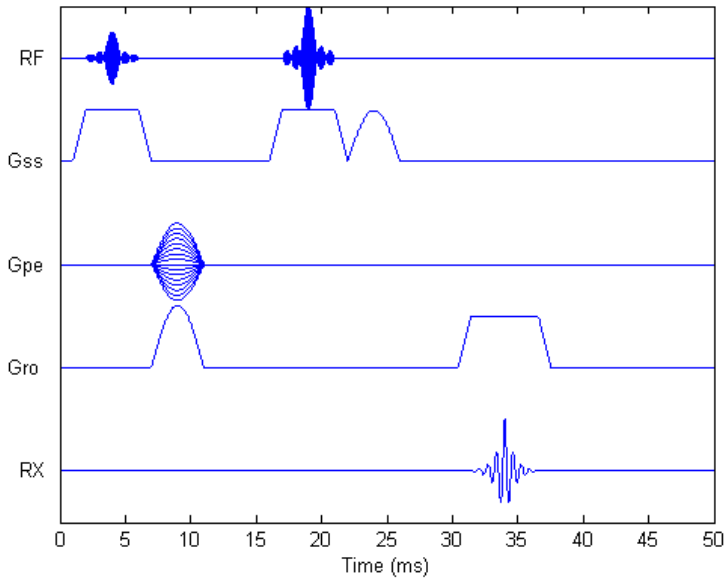

Fig. 1. Typical spin echo pulse sequence. The RF trace represents the transmitted RF (excitation) pulses. The Gss, Gpe, and Gro traces are the slice selection, phase encoding, and readout (frequency encoding) gradient current waveforms, respectively. The phase encoding gradient is stepped through a table of values to acquire all of *k*-space. The RX line represents a signal received from the sample.

In 2D Fourier MR imaging, a single slice at a desired location and of desired thickness is excited by applying a slice selection gradient while transmitting a narrow bandwidth radiofrequency (RF) pulse, thereby exciting a slice normal to the direction of the gradient. The spectral content of the RF pulse determines which spatial locations are excited, such that a sinc modulated RF pulse will result in a rectangular slice profile. By shifting the frequency of the RF pulse, the slice is offset from the center of the gradient field and by changing the bandwidth of the RF pulse or the strength of the gradient, the slice thickness is controlled. Once the desired slice is excited, position information is encoded allowing image formation by a 2D inverse Fourier transformation as shown in Fig. 2. This is done by both frequency and phase encoding gradients such that with each echo one line of *k*-space is acquired, each line having a different phase encoding gradient value.

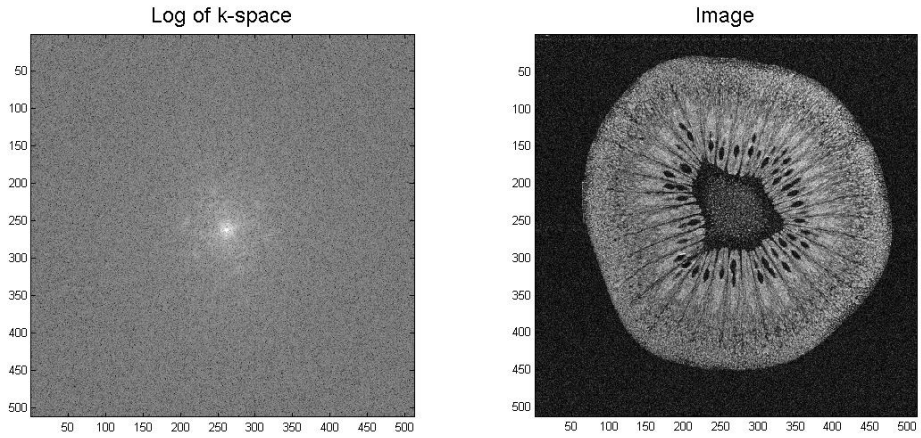

Fig. 2. Example *k*-space and resulting image. Log plot of *k*-space acquired from a slice of kiwi fruit (left) and image (right) following a 2D inverse Fourier transform. Each row or line of the *k*-space matrix represents an echo acquired with a particular phase encode gradient amplitude.

For the following explanation, a slice along the y direction, with frequency encoding along the z direction, and phase encoding along the x direction is assumed. In the presence of a frequency encoding gradient G_z and a phase encoding gradient G_x the time domain received signal $S(t)$ after demodulation can be expressed as

$$S(t) = \iint_{slice} I(x,z) e^{j\gamma G_x x\, T_p + j\gamma G_z z t} dx dz$$

where T_p is the phase encoding pulse duration and $I(x,z)$ is the image intensity at point (x,z). This equation can be rewritten, applying the following substitutions:

$$k_x = \gamma G_x T_p, \qquad k_z = \gamma G_z t.$$

The image can then be found by a 2D inverse Fourier transform as follows

$$I(x,z) = \int_{-\infty}^{\infty} \int_{-\infty}^{\infty} S(k_x, k_z)\, e^{jk_x x} e^{jk_z z} dk_x dk_z$$

where $S(k_x, k_z)$ is the acquired Fourier transform of the image, referred to as *k*-space. In the *k*-space formulation, acquisition of an MR image is considered as a noisy observation of a spatial frequency distribution which is the Fourier transformation of the spatial distribution of the unknown sample [31]. Because the Fourier transform is computed numerically, a Fast Fourier Transform (FFT) algorithm is used to compute the Discrete Fourier Transform (DFT). In this method only discrete values of *k*-space are sampled and used in the reconstruction. The *k*-space step size determines the field of view of the image, given by $\Delta k = 2\pi/FOV$. Along the frequency encoding direction, the step size is determined by the frequency encoding gradient strength and digitizer sampling rate, while along the phase encoding direction, the step size is determined by the duration and step size of the phase encoding gradient pulse. The resolution of the

image is determined by the extent of *k*-space sampled. From this formulation, a spatial frequency distribution can also be obtained over a volume, with phase encoding in two directions and with a volumetric image given by an inverse 3D Fourier transform. Such is called a 3D sequence and is often useful for MR microscopy of a volume.

Other groups have proposed an additional gradient coil for novel applications in MR imaging. In 1988, a nonlinear gradient pulse was proposed as a method to compress the dynamic range of the received signal so that there is no single line of *k*-space in which all of the sample is in phase [32]. While having a negligible impact on image magnitude, the gradient pulse significantly reduces the amplitude of the peak echo. Parker et al. reported using custom gradient coils to create several imaging regions, extending gradient field of view while limiting the extent of the B_z field at the edges of the field of view, thus reducing the propensity for peripheral nerve stimulation [33]. In a method termed Patloc, Zaitsev's group has used a set of localized gradients in combination with an array of receive coils to reduce peripheral nerve stimulation [34]. Use of non-linear spatial encoding fields has also been discussed [35], with the introduction of the concept of local *k*-space, in which the acquired spatial frequency components of the sample vary with position. Another method called O-Space imaging seeks to use gradient encoding fields that better compliment the spatial localization performed by the B_1 sensitivity patterns of an array of surface RF coils [36]. A fourth gradient insert coil specifically for improved diffusion weighted imaging has also be implemented by Feldman, et al. [37].

2.1.2 RF Coils and Arrays

In MRI, the RF coil is typically a resonant structure capable of creating or detecting a time changing magnetic field, called the B_1 field, in a plane transverse to the main field of the magnet. The resonant frequency of the structure is determined by the field strength of the magnet, given by the Larmor relation above. Traditionally, it has been desirable to build RF coils which create a uniform magnetic field over the extent of the sample, allowing uniform excitation of a slice or volume and giving uniform sensitivity for signal reception. One of the most ubiquitous coil geometries used for this with solenoidal superconducting magnets is called a birdcage coil [38]. Its cylindrical geometry is convenient because it can be placed inside the cylindrical bore of a magnet with a patient inside the coil while creating an RF magnetic field transverse to the axis of the magnet bore. Several figures of merit for an RF coil are the field uniformity, sensitivity (B_1/i), and the quality factor or Q.

Another type of coil called a surface coil can provide a higher sensitivity over a limited spatial region. Such coils were traditionally used when studying a particular anatomy. However, with the advent of the NMR phased array [19] it has become standard to combine the signals received by multiple surface coils to extend their SNR benefits over the field of view of the entire array. It has been shown that combining multiple loop surface coils always results in an improvement in SNR near the array surface, with no loss of SNR deeper within the sample [39]. It has long been noted that using the additional information provided by multiple receiver coils could allow reduction of the image acquisition time [20, 21]. When using arrays of surface coils,

each coil element detects signals from a different region of the sample, thus additional spatial information is collected by using arrays and multiple receivers. If the coil elements are placed along the phase encoding direction, this additional information can supplement or replace the spatial information provided by gradient phase encoding, reducing the number of time consuming phase encode steps required to reconstruct an MR image.

One implementation of such parallel imaging in the *k*-space domain is called Simultaneous Acquisition of Spatial Harmonics, or SMASH [23]. This technique uses linear combinations of the signals received by several array elements to synthesize different *k*-space offsets, thus several *k*-spaces each offset from one another, are acquired in parallel. These are then combined, yielding the full *k*-space from a reduced dataset from which an image is obtained. In another implementation of parallel imaging called Sensitivity Encoding or SENSE [24], the reconstruction is performed in the image domain. In this method a sensitivity map is initially obtained from each array element. Images are then acquired with a reduced number of phase encode steps, producing an aliased image from each coil. These aliased images are weighted by the coil sensitivity maps and combined to produce a full FOV image without aliasing.

Another technique called Partially Parallel Imaging with Localized Sensitivities (PILS) describes a parallel image reconstruction method which relies on the localized sensitivity patterns of the individual coils to avoid acquiring highly accurate field maps [40]. Using the known width of the sensitive region of each coil and each coil's sensitive region within the full field of view, an image can be constructed with a reduced number

of phase encode steps. A similar technique has been used by our group for accelerated reconstructions using an array of planar pair coils [41] since each array element has a highly confined field pattern and known position within the full field of view.

In a recent review article by Larkman and Nunes [18], a number of established and emerging applications have been listed as beneficiaries of parallel MRI. Three dimensional MR imaging particularly benefits from parallel imaging as it is inherently a time consuming technique [42]. Acceleration can be applied in both phase encoding directions for improved efficiency. Likewise, imaging of dynamic processes such as in MR angiography and cardiac MRI benefits from parallel imaging [43, 44]. Parallel MRI has also been applied to functional brain imaging (fMRI) [45].

2.2 Single Echo Acquisition Imaging

Single Echo Acquisition or SEA imaging is a technique developed by our group which enables acquisition of an MR image in a single echo, eliminating the need for a phase encoding table, while retaining the standard slice selection and frequency encoding gradients [7]. By using an array of narrow coils with spatially confined B_1 field patterns, each coil element is responsible for detecting the signal from the region of the sample directly above it [41]. By applying a frequency encoding gradient along the long axis of the coil elements and computing the 1D Fourier transform of the detected signals, a projection along each coil is obtained, as shown in Fig. 3. By stacking the projections side by side, an image of a slice parallel to and near the array surface is displayed. This system employs a custom built receiver capable of demodulating, digitizing, and storing the signals detected from 64 coils upon each echo [46].

This system has enabled MR imaging at unprecedented frame rates and has been used to image turbulent flow [25, 26] and for highly accelerated MR elastography [28, 29]. Furthermore, by using a modified EPI sequence images have been acquired at one thousand frames per second [47]. While standard gradient encoding alone can achieve high frame rates, the SEA technique is unique in that it offers the advantage of having an extremely fast "shutter" speed, in which non-periodic or transient events can be captured. Such events may otherwise be obscured in a standard *k*-space acquisition strategy. A particular constraint in the implementation of arrays for SEA imaging is that the B_1 field patterns of adjacent coil elements must be isolated and coupling between coils must be minimal, otherwise the signal detected by each coil will come from regions other than that which is directly above the coil element, introducing artifacts in the SEA reconstructions. For these reasons, planar pair coils were selected in the original

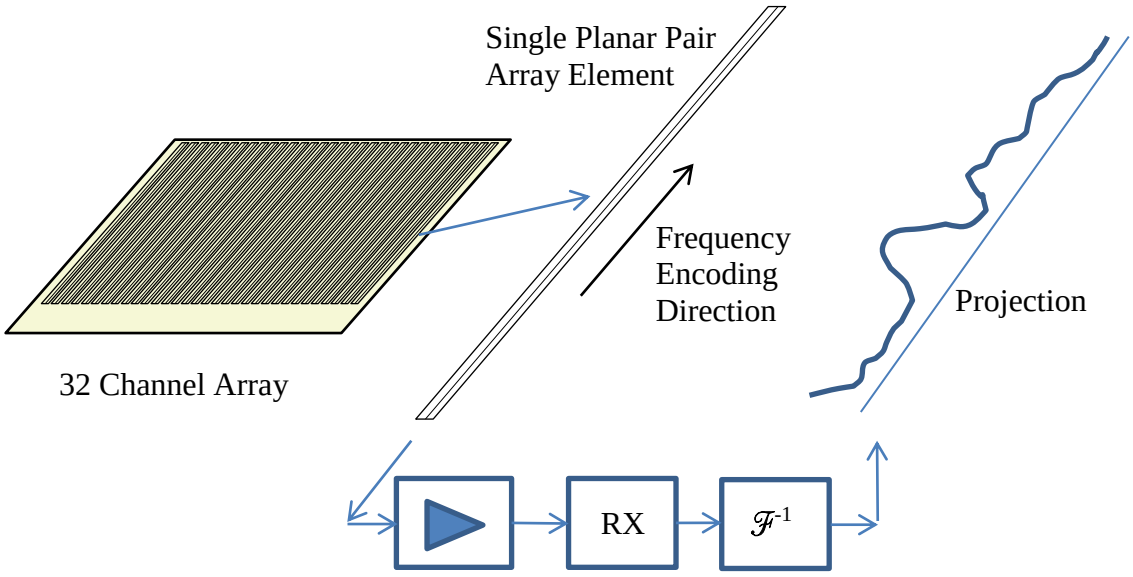

Fig. 3. Diagram of the SEA imaging technique. The 1D projection along each coil element provides a column of the SEA image.

implementation of this method. The demand for a confined field pattern restricts the SEA technique to regions very near the array surface as the pattern broadens with distances from the coils [41, 48].

2.3 RF Coil Phase Gradient

2.3.1 Effect and Compensation

It was noted in 1987 that when using a different RF coil for transmission and reception while acquiring only the center line of *k*-space, the location of the peak of *k*-space was offset due to the phase gradient introduced by the B_1 pattern of the RF coils [49]. In SEA imaging, the RF coil dimension and voxel size are roughly the same, so this effect is particularly pronounced, causing intravoxel signal cancellation. However, because the phase gradient due to a planar pair coil element is approximately linear, a linear magnetic field gradient pulse has been used to impart a phase gradient in the sample opposite of that due to the RF coil, refocusing the signal from each voxel [9, 50]. The phase gradient due to the RF coil can be calculated at different positions and distances from the coil by using the Biot-Savart law for an infinitely long conductor as a quasi-static approximation the magnetic field due to the RF coil element. The phase due to the RF coil at a position (x, y) is estimated from the x and y components of the magnetic field due to the coil,

$$\phi_{coil}(x, y) = \text{atan}\frac{B_{1,y}(x, y)}{B_{1,x}(x, y)}$$

from which the x phase gradient can be calculated

$$\frac{\partial \phi_{coil}}{\partial x}.$$

This x phase gradient can be corrected for a slice at a distance $y = a$ from the array surface by applying an appropriate pulse of the main gradient which satisfies the following

$$\left.\frac{\partial \phi_{coil}}{\partial x}\right|_{y=a} = -\gamma G_x T_p.$$

Assuiming a uniform phase distribution within the sample following the slice selection gradient and RF excitation pulses, the phase distribution effectively seen by a planar pair coil element can be plotted in the region above one coil element, as shown in Fig. 4. Because the voxel size along x in SEA imaging is equal to the coil width, a phase variation along x will lead to signal cancelation within the voxel. Fig 5 shows the phase distribution within the sample upon application of 15 rad/cm and 25 rad/cm gradient

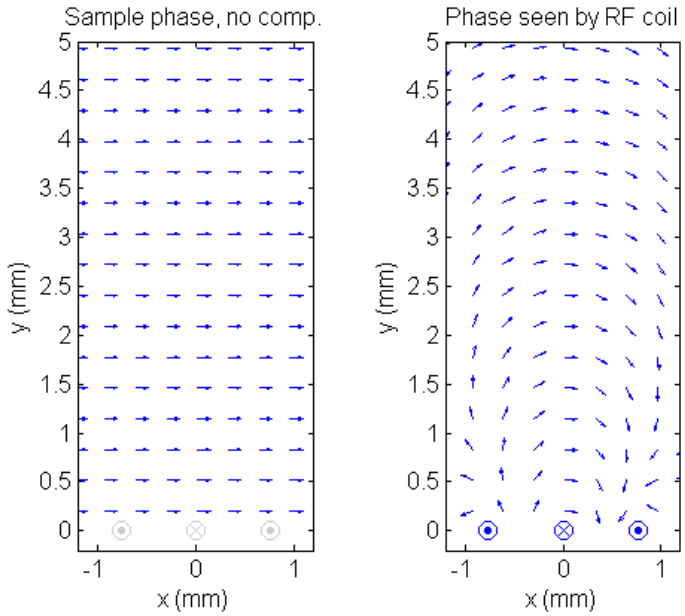

Fig. 4. Phase distribution due to a planar pair RF coil. Phase distribution within a sample above a single RF coil (left) and phase distribution detected by the RF coil. Although the sample has a uniform phase distribution, the RF coil detects signals coming from different positions as having different phase due to its B1 field pattern.

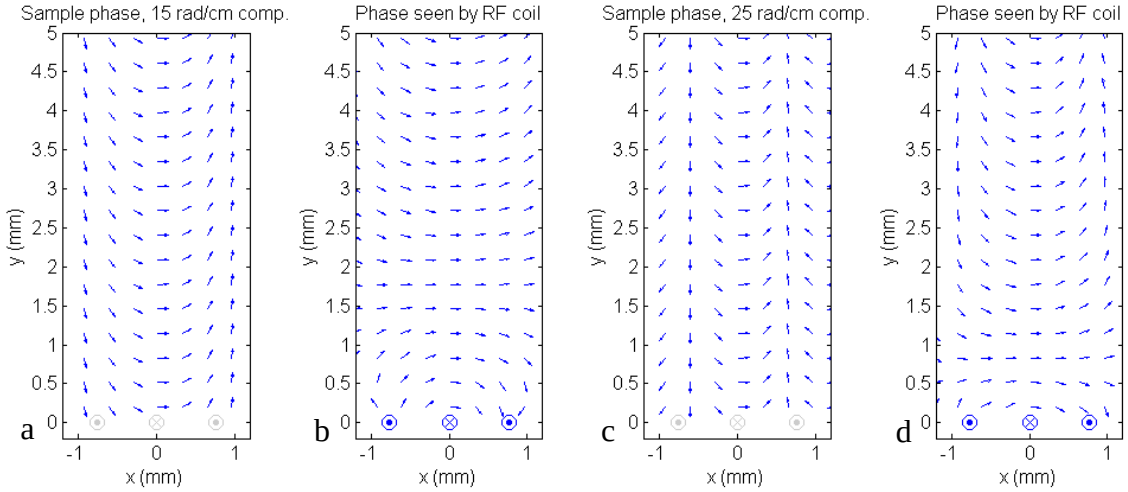

Fig. 5. Phase distribution following a phase compensation gradient pulse. Shown after application of compensation gradient of 15 rad/cm (a) and phase seen by planar pair RF coil (b). Phase in the sample after 25 rad/cm compensation (c), Phase seen by the coil (d). With 15 rad/cm compensation, the slice 1.5 mm from the coil surface is properly corrected, while with 25 rad/cm, the slice 0.6 mm from the coil is corrected.

pulses. The stronger phase compensation gradient cancels the phase ramp seen by the coils nearer to the coil surface, while the weaker pulse corrects the phase further away.

2.3.2 Dual Sided Arrays

When using planar receive arrays placed above and below a sample, the phase gradient due to the coils has opposite magnitude at the top and bottom array surfaces, as shown in Fig. 6 [51]. The effect of the RF coil phase gradient on the acquired *k*-space can be computed [10]. The signal received from a uniform sample in the presence of a linear phase gradient for a thin slice at a distance $y = a$ from the array plane can be calculated as a function of the applied phase compensation gradient strength

$$S(\phi_x) = \int_{-\infty}^{\infty} |B_1(x, y = a)|\, e^{j\phi_{coil,x}(x,y=a)} e^{j\phi_x x} dx.$$

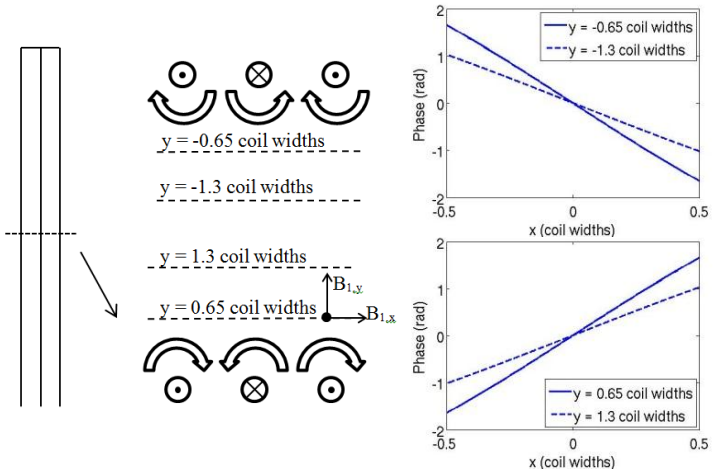

Fig. 6. Layout and cross section of a planar pair coil element and calculated phase gradients. The components of the vector sum of the magnetic fields from the three conductors allow approximation of the phase due to the RF coil element (ϕ_{coil}). The phase gradient decreases with distance from the array plane and reverses on opposite sides of the array elements [51]. (© 2012 IEEE)

Evaluating this integral at different distances above and below the bottom and top planes of a dual-sided array composed of 1.52 mm (60 mil) wide planar pair elements, a plot of peak signal for different compensation gradient strengths is obtained, shown in Fig. 7.

Thus, *k*-space is shifted by a different amount at different distances from the array, requiring a different compensation gradient pulse, which has been shown to result in a loss of SNR when using a compromise gradient value for highly accelerated 3D imaging [52, 53]. Furthermore, the phase gradient is opposite for different sides of a dual-sided array, requiring a compensation pulse of opposite magnitude. The plot shows that while a single compromise phase compensation gradient value can be selected to give signal from several slices using either the bottom or the top array for receive, there is no compensation gradient value that yields peak signal from both arrays simultaneously.

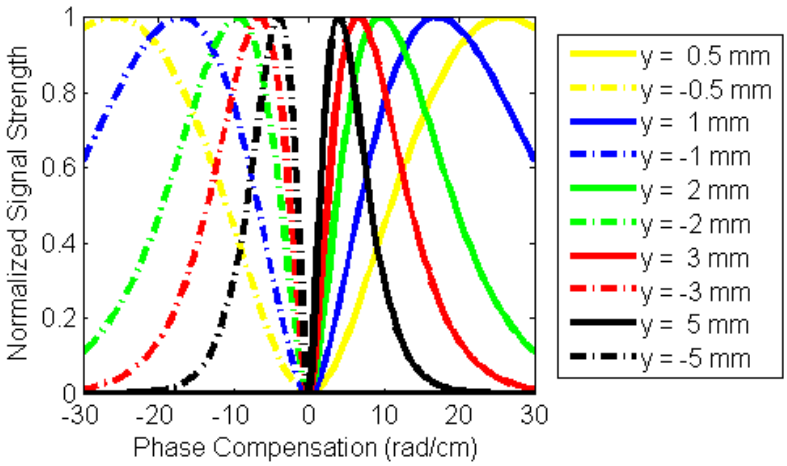

Fig. 7. Normalized peak signal strength vs compensation gradient pulse from a dual-sided array. The array planes are separated by 1 cm.

An additional feature of SEA imaging using different compensation gradient values is that the images can be sensitized to different spatial frequencies along the x direction. For instance, if a compensation gradient is used other than that which gives peak signal, an image will be acquired containing higher spatial frequencies. Combining echoes acquired with different phase compensation gradient values has been used to enhance resolution while keeping a high apparent frame rate [54]. Consideration of RF coil phase is not unique to SEA imaging. Another group has developed a method called transmit array spatial encoding (TRASE) in which the RF phase gradient is used to acquire an image without gradient encoding [55]. This method utilizes the RF coil phase as a way to traverse *k*-space and acquire an image.

2.4 MR Microscopy

In MRI, the term microscopy is not intended to refer to the same resolutions obtained using optical microscopy, but to a higher resolution than that typically obtained

by MR imaging. After a survey of conference papers, Glover and Mansfield reported in 2002 that most MR imaging applications labeled "microscopy" by their authors had pixel resolutions of better than 100 μm [56]. However, they added that voxel volume on the order of nanoliters is a better indicator and that users accept resolutions giving the required information in a reasonable time. The authors give a number of factors which limit the achievable resolution in MR microscopy. Spin-spin (T2) relaxation causes intra-voxel phase variation, exponentially reducing the magnetization due to random spin flips. Gradients other than the imaging gradients de-phase spins during signal acquisition. Movement within the sample due to flow, self-diffusion, or vibration also reduces the signal.

Image SNR largely determines what resolution is achievable. Doubling the resolution in two dimensions will reduce SNR by a factor of four, as signal scales linearly with voxel volume. This loss can be recovered by acquiring sixteen averages, but the measurement repetition rate is limited by the T1 relaxation time of the sample, making many averages time consuming and impractical. Another method of improving SNR, which is related most to this work, is to use smaller RF coils. The SNR in the MR experiment is given by

$$\psi = \nu^2 / \left[\alpha a^2 \nu^{1/2} + \beta b^5\right]^{1/2}$$

where a is the coil radius and b is the sample radius [5]. The first term in the denominator is related to noise from the coil while the second term includes sample noise. In large samples, such as in human imaging, the noise due to the sample dominates, while in very small samples the noise due to the coil becomes more

significant. In most MR microscopy applications, the noise due to both sample and coil are considered. Peck et al. provides a theoretical analysis and discusses some of the design considerations when building microcoils [57]. It is shown that use of microcoils always improves SNR for volume limited samples but that other difficulties such as B_0 distortion due to the proximity of the coil to the sample may create additional constraints.

A number of researchers have successfully performed magnetic resonance microscopy using small coils to provide adequate SNR [58]. NMR microscopy was first reported by Aguayo et al. in 1986 [59], who used a 5 mm solenoid RF coil to image a single cell with a resolution of 10 x 13 μm, but with slice thickness of 250 μm. Johnson et al. developed the concept of magnetic resonance microscopy as a tool for histological studies, citing advantages due to its non-invasiveness, the multitude of proton contrasts it provides, and its 3D nature. Ciobanu et al. improved resolution, achieving voxel dimensions of 3.7 x 3.3 x 3.3 μm [60] by using a solenoid microcoil wrapped around a 73 μm diameter quartz tube. A number of other researchers have pursued imaging of biological cells [61], however some imaging applications demand a wider field of view than that allowed by using a single small coil.

Webb's group constructed a four channel phased array of small saddle coils for microscopy at 14.1 T, achieving an approximately 70% increase in SNR [62]. The same group used an array of four arc shaped coils around a cylinder for microscopy for SENSE and GRAPPA accelerated imaging [63]. The greater field of view provided by an array of small coils was noted by Laistler et al. in an application of MR microscopy

of human skin vasculature [64]. The authors obtained images at 100 μm isotropic resolution using a 15 mm surface coil but cited the small imaging area as the greatest limitation, suggesting future use of arrays of small coils.

The 64 channel array and receiver employed in this work have previously been used for accelerated MR microscopy over the entire field of view of the array [8]. Just as SEA imaging is enabled by the spatially confined field patterns of the coil elements, parallel microscopy also benefits from this isolation. Each narrow coil element functions as an independent microcoil responsible for imaging the region of the sample above it. The planar pair geometry provides a significant SNR benefit at the surface of the array while also having a spatially confined field pattern to facilitate improved parallel imaging performance. Combining the high resolution images from each array element gives a "wide field of view" microscopy image. Likewise, by adding an array above a sample, high resolution microscopy can be obtained simultaneously from planes near the bottom and top of the sample. While correction for the RF phase gradient due to the array coils is essential for the most accelerated cases such as SEA imaging from both sides of the array, the *k*-space offset due to the planar pair coils becomes less significant in higher resolution imaging.

3. FOURTH GRADIENT COIL

3.1 Desired Gradient Field

Because a standard gradient pulse from the MR scanner can compensate for the RF phase gradient due to only one side of a dual-sided or "sandwich" array at a time, a fourth gradient coil has been implemented to allow simultaneous phase compensation for the bottom and top planes of the array. Using this gradient coil, a single compensation pulse allows simultaneous SEA imaging from slices at the bottom and top array surfaces, which would otherwise require two separate echoes with compensation pulses of opposite magnitude. In order to achieve this, the gradient coil must produce a z directed magnet field B_z having a linear x gradient which also varies linearly in y, reversing midway between the planes of the dual-sided receive array. An ideal B_z field with a gradient in x which reverses at the $y = 0$ plane is expressed as

$$B_z = kxy$$

$$\frac{\partial B_z}{\partial x} = ky = G_x(y)$$

where k is the gradient variation in G/cm^2 and $G_x(y)$ is the x gradient evaluated at plane y in G/cm. The x phase gradient $\partial\phi/\partial x$ at plane y created by a half-sine gradient pulse is calculated

$$\frac{\partial \phi}{\partial x} = \gamma G_x(y) T_p \frac{2}{\pi}$$

where γ is the gyromagnetic ratio ($2\pi \times 4257$ Hz/G), G_x(y) is the gradient amplitude at plane y in G/cm, T_p is the pulse duration in seconds, and the factor of $2/\pi$ accounts for

the area of a half-sine pulse. In discussing the fourth gradient coil, a desired phase gradient variation of +/- 25 rad/cm over a 1 cm slab due to a 4 ms half sine pulse will be assumed. There are other pulse durations and shapes which would also work, and different RF coil configurations may demand more or less phase compensation, but it was necessary to select one set of parameters for all calculations and comparisons. Therefore the gradient amplitude needed to compensate for an RF coil phase gradient of +/- 25 rad/cm over a 1 cm slab at the surfaces of dual sided planar pair array is +/- 0.367 G/cm. Contour plots of the desired B_z field, x gradient field G_x, and phase gradient $\partial\phi/\partial x$ are shown in Figs. 8 and 9. In Fig. 10, the signal acquired from a dual sided planar pair array as a function of phase compensation from the main gradient with the addition of a pulse from this desired fourth gradient is calculated. The signal peaks from the top and bottom arrays are moved towards a compensation value of zero, meaning that a single echo with no phase compensation from the main gradient will return signal from both sides of the dual-sided array.

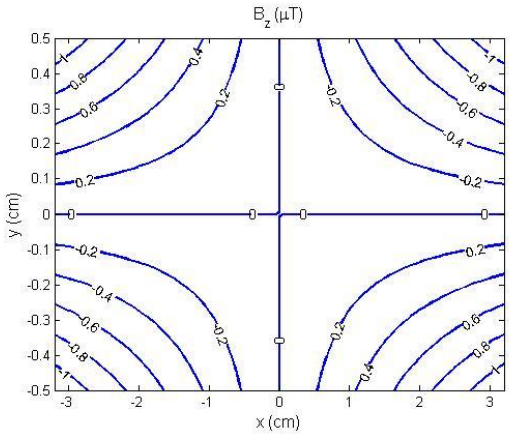

Fig. 8. Desired fourth gradient coil magnetic field. Desired B_z field yielding an x gradient field of +/- 0.367 G/cm which reverses along y. Ideally, there is no variation along z.

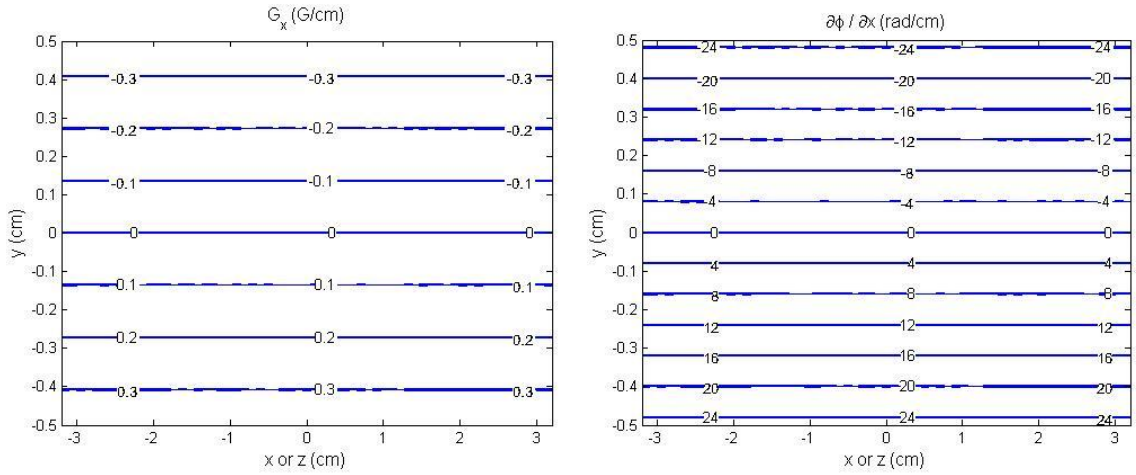

Fig. 9. Desired gradient field and phase gradient. Gradient field (left) and phase gradient field (right) due to a 4 ms, half sine pulse of the B_z field shown above.

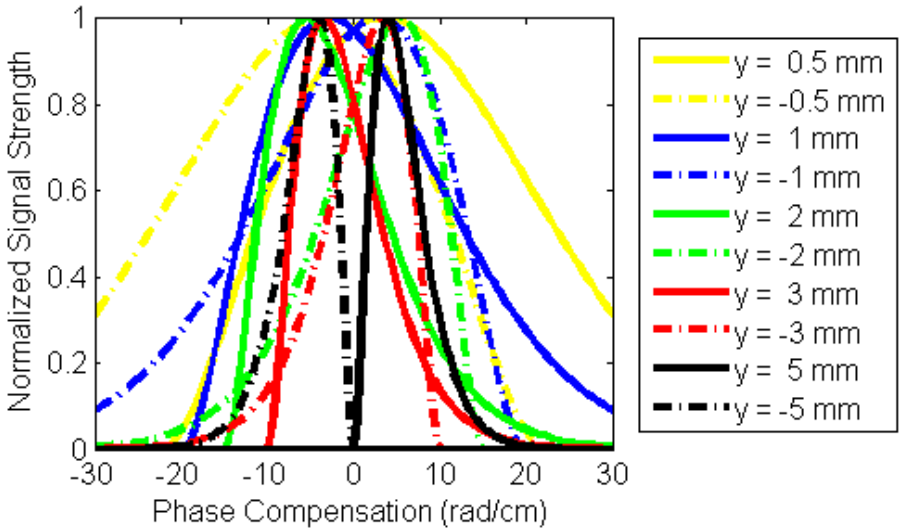

Fig. 10. Normalized signal vs main gradient phase compensation from the dual sided array with a pulse of the fourth gradient. The positive slices are above the bottom array, while the negative slices are below the top array With a fourth gradient pulse producing a slice dependent phase gradient of +/- 25 rad/cm over a 1 cm slab moves the signal peaks together. With the fourth gradient, fewer echoes are necessary to receive peak signal from both arrays.

Potential gradient coil designs were evaluated using a Biot-Savart law calculation for a magnetic field generated by straight, finite-length, current filaments, given in [65],

$$\mathbf{B} = \frac{\mu_0 I \hat{\mathbf{a}}_\phi}{4\pi\rho}(\cos\alpha_2 - \cos\alpha_1)$$

where **B** is the resultant magnetic field, μ_0 is the permeability of free space, α_1 and α_2 are the angles between the calculation point and the ends of the current filament, and ρ is the distance between the calculation point and the line containing the current filament. All simulations were carried out in MATLAB (The Mathworks, Natick, MA).

3.2 Cho-type Uniplanar Coil

The first gradient coil investigated was the three-axis uniplanar or surface gradient coil published by Cho [66, 67]. This coil was reported to create strong gradient fields over a limited field of view for high resolution imaging, with the strength of the three gradient fields decreasing with distance from the coil surface. The decrease of the x gradient field with distance from the coil made the design attractive for providing slice dependent RF coil phase compensation. With an additional offset pulse of the standard x gradient, a reversal of the total x gradient field can be created midway between the planes of a dual-array receive coil. The x gradient coil described by Cho was scaled to 20 x 40 cm and the B_z field and its x gradient were computed using the Biot-Savart law given above. An initial attempt to extend the field of view of this coil by moving the inner z directed conductors further apart yielded a variation of +/- 3.5% over the desired 6.4 x 6.4 cm imaging region at a distance of 4 cm above the surface of the coil. The simulated coil and calculated fields are shown in Fig. 11.

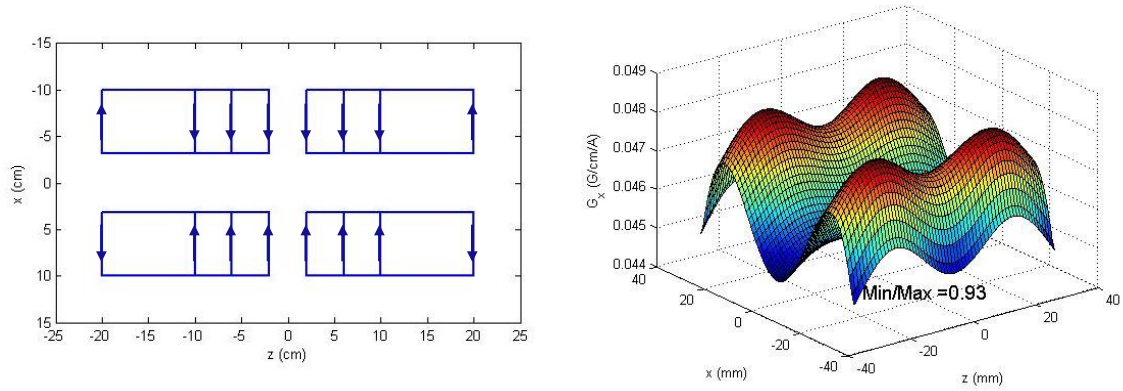

Fig. 11. Layout and calculated gradient field of uniplanar x gradient coil. The coil shown is based on the geometry reported by Cho, scaled to 20 x 40 cm with inner z directed conductors moved outward by 60% (left) and gradient field calculated 4 cm above the coil surface (right). The x-directed current, which contributes to the gradient field is indicated by arrows.

The coil was constructed using an in-house milling machine (LPKF Laser & Electronics AG, Garbsen, Germany) with 4 oz double sided copper clad circuit boards, as shown in Fig. 12 [68]. While the printed circuit board implementation resulted in some deviation from the ideal conductor placement due to the width of the traces, simulations with the varied conductor lengths revealed little impact on the resulting fields. Four identical sections having two turns on each side were milled and affixed to a half-inch acrylic board by epoxy glue. The four pieces were connected using coaxial cable to contain the magnetic flux of the conductors, which is important to prevent cable deflection during gradient current pulses or corruption of the gradient field. The field of the coil was initially measured using a positioning system and hall effect sensor previously developed in the lab [69], however imaging was ultimately selected as the validation method of the gradient field for convenience and accuracy.

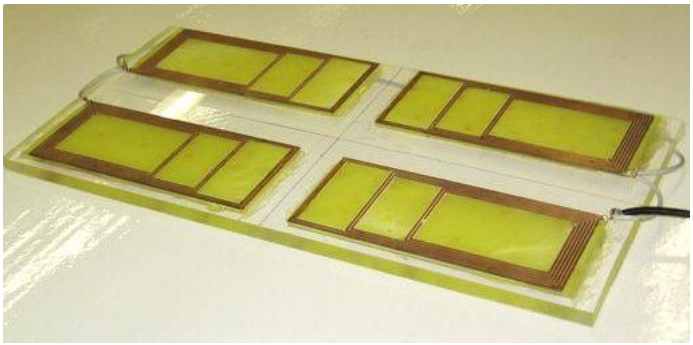

Fig. 12. Printed circuit board implementation of Cho-type uniplanar gradient coil [68].

The sensitivity of the PCB uniplanar coil was calculated at distances of 3.5, 4.0, and 4.5 cm from the surface of the coil to be 0.0555, 0.0514, and 0.0469 G/cm/A. The rate of decay is approximately 0.0086 G/cm^2/A. Therefore, to achieve the desired gradient fall off of 0.734 G/cm over a 1 cm slab (calculated above as +/- 0.367 G/cm), a uniplanar gradient pulse of 85.4 A is required. This will produce an x gradient of 4.74 G/cm at a distance of 3.5 cm from the coil surface, falling to 4.01 G/cm at a distance 1 cm farther from the coil. If the sample and RF dual-array are centered at a distance of 4.0 cm above the surface gradient, an offset pulse of -4.4 G/cm is required from the main x gradient to achieve a total x gradient field of approximately +/- 0.37 G/cm over a 1 cm slab centered at 4 cm above the gradient coil, realizing the desired +/- 25 rad/cm. Despite the +/- 3.5 % linearity shown above, the need to offset the uniplanar gradient field significantly increases the error of the total field, with greater than 100% error in the top and bottom planes. The error evident at the edges of the field of view, shown in Fig. 13, will have a deleterious effect on phase compensation in those regions of the sample. However initial results acquired in the center of the gradient field, shown in Fig. 14,

indicate that a uniplanar gradient pulse is able to collect the peaks of *k*-space of the different slices towards the middle of the acquired *k*-space, validating the potential of this method.

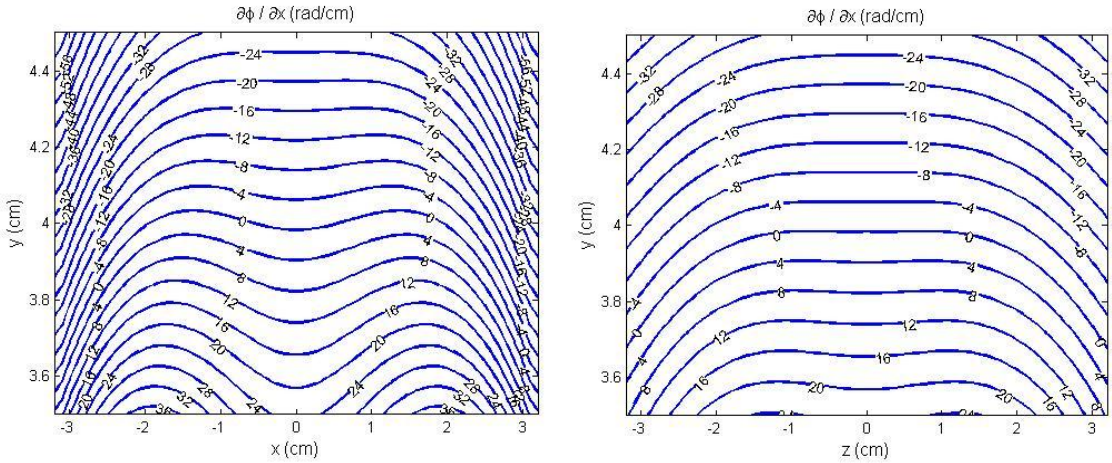

Fig. 13. Contour plots of the phase gradient resulting from the uniplanar gradient offset by the main gradient. The linearity over the desired 6.4 x 6.4 x 1 cm field of view is not sufficient.

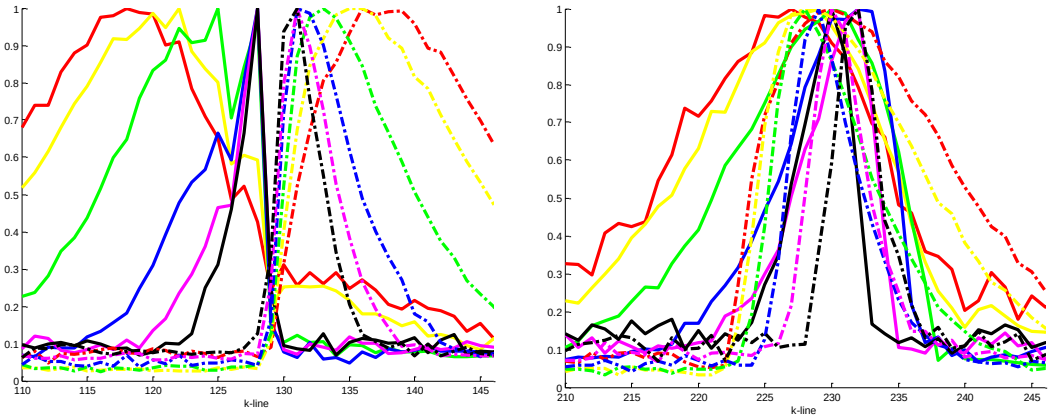

Fig. 14. Normalized signal vs phase compensation with uniplanar gradient pulse. Plots without (left) and with (right) a pulse from the uniplanar fourth gradient coil over a range of slice offsets using a single planar pair coil placed above and below the center of the sample for receive. The fourth gradient collects the peaks together, although with an offset [68].

Several attempts were made to improve the linearity of the uniplanar coil by modifying the conductor spacing in simulations, but little improvement was achieved. One attempt which gave a more uniform field along the x direction involved a combination of two Cho-type uniplanar coils of different inner conductor spacing and number of turns stacked together. The conductors of this coil are shown in Fig. 15, and the calculated phase gradients are shown in Fig. 16. A prototype was constructed, however the non-linearity in both the x and z directions remains too great to use this coil for slice dependent phase compensation.

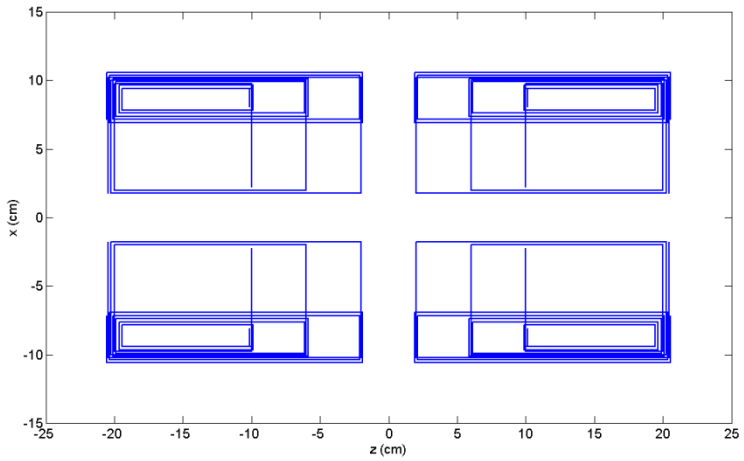

Fig. 15. Conductor layout of modified Cho-type uniplanar gradient coil.

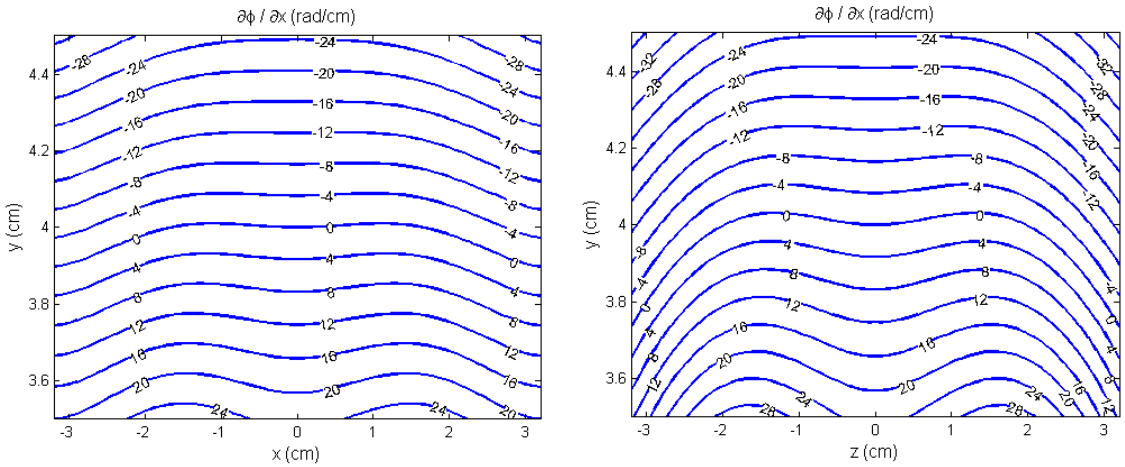

Fig. 16. Phase produced by the modified Cho-type uniplanar gradient coil. Shown in the in the xy (left) and yz (right) planes.

3.3 Mirrored Cho-type Biplanar Coil

In the process of attempting to improve the linearity of the uniplanar gradient coil by applying the target field method, which is described in detail in the next section, it was found that a biplanar gradient coil creates a more linear field reversal due to the symmetry of the geometry. By placing planar x gradient coils of equal current above and below the imaging region, the gradient field inherently reverses along y midway between the current planes, eliminating the need for a strong offset pulse from the main gradient coil. While this design was not implemented, before discussing the biplanar target field coil, some calculated fields are given in Fig. 17 to show the improvement of placing two uniplanar coils as described above and below the phantom at y = +/- 4 cm. The inner z directed conductors were also moved together by 12.5% for better field linearity. The calculated sensitivity of this coil at y = +/- 0.5 cm (the location of the RF receive array planes) is +/- 0.0114 G/cm. The rate of decay is 0.0227 G/cm^2/A, meaning that a pulse

of 32.3A with no offset pulse from the main gradient will result in the desired phase gradient of +/- 25 rad/cm over a 1 cm slab. The error in the top and bottom planes is approximately 40%.

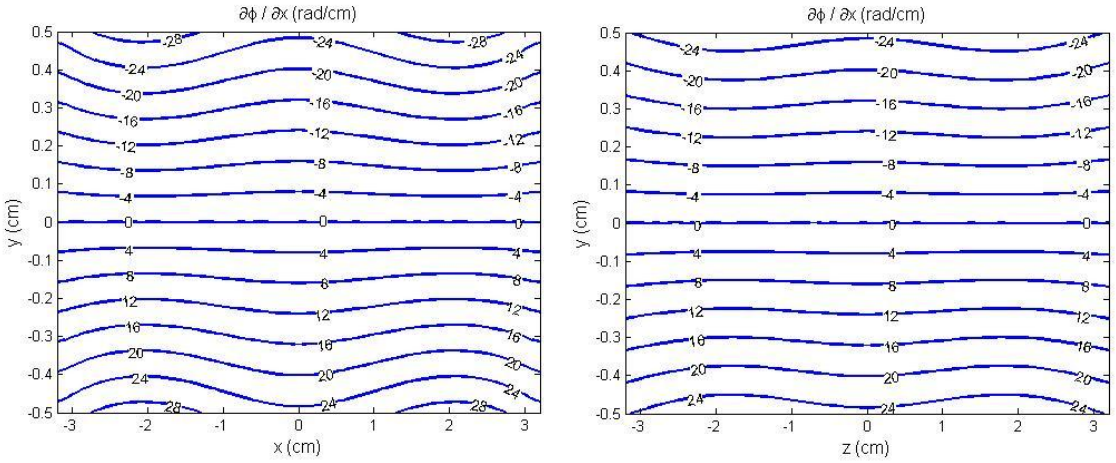

Fig. 17. Contour plots of the phase gradient resulting from the biplanar implementation of a modified Cho-type gradient coil. The linearity over the desired 6.4 x 6.4 x 1 cm field of view is improved over the uniplanar coil.

3.4 Target Field Biplanar Coil

A number of methods have been reported for designing the gradient coils used in MRI [70]. There are many constraints designers face in optimizing gradient coils, including linearity, minimum inductance for fast imaging, high coil sensitivity for strong gradient fields, heat dissipation, acoustic noise, and mechanical stability. One of the key developments enabling construction of optimized gradient coils was the target field method reported by Turner [71]. This method produces winding or cutting patterns often referred to as "fingerprint" patterns because of the concentric current paths. Turner's analytical approach to the design problem for cylindrical gradient coils inverts the Biot-

Savart law, finding the current distribution yielding the desired magnetic field. Using a Green's function expansion [72], the magnetic field due to current distribution on a cylindrical surface is expressed as a Fourier-Bessel series. The "target" magnetic field is specified on an inner cylinder, which allows solving for the current distribution on an outer cylinder by an inverse Fourier transform. The distribution is then apodized and converted into a discrete cutting or winding pattern for fabrication.

3.4.1 Calculation of Current Density

Martens et al. applied the target field technique to biplanar gradient coils [73], which is the approach followed here. The total current density $\mathbf{J}(\mathbf{r})$ is the sum of the current densities at two planes located at y = ± a, such that the planes are separated by a distance of 2a, as follows:

$$\mathbf{J}(\mathbf{r}) = [J_x^a(x,z)\hat{x} + J_z^a(x,z)\hat{z}]\delta(y-a) + [J_x^{-a}(x,z)\hat{x} + J_z^{-a}(x,z)\hat{z}]\delta(y+a).$$

As in the approach for a cylindrical coil, a Green's function expansion is employed

$$G(\mathbf{r},\mathbf{r}') = \frac{1}{|\mathbf{r}-\mathbf{r}'|}$$

$$= \frac{1}{2\pi}\int_{-\infty}^{\infty}\int_{-\infty}^{\infty}\frac{d\alpha\, d\beta}{\sqrt{\alpha^2+\beta^2}} e^{i\alpha(x-x')} e^{i\beta(z-z')} e^{-\sqrt{\alpha^2+\beta^2}(y_>-y_<)}$$

where $y_>$ or $y_<$ is the greater or lesser of y and y'. The current densities and their Fourier transforms are related by

$$j_x^a(\alpha,\beta) = \int_{-\infty}^{\infty}\int_{-\infty}^{\infty} dx\, dz\, e^{-i\alpha x} e^{-i\beta z} J_x^a(x,z)$$

$$J_x^a(x,z) = \frac{1}{4\pi^2}\int_{-\infty}^{\infty}\int_{-\infty}^{\infty} d\alpha\, d\beta\, e^{i\alpha x}\, e^{i\beta z}\, j_x^a(\alpha,\beta).$$

Further, the continuity equation

$$\nabla \cdot \mathbf{J}(\mathbf{r}) = 0$$

is used to relate the x and z components of the current densities

$$\alpha j_x^a(\alpha, \beta) + \beta j_z^a(\alpha, \beta) = 0.$$

The vector potential

$$\mathbf{A}(\mathbf{r}) = \frac{\mu_0}{4\pi} \int_V \frac{J(r')}{|\mathbf{r} - \mathbf{r}'|} d^3x'$$

is computed using the above Green's function expansion, which is used to find the z component of the magnetic field

$$B_z(r) = -\frac{\mu_0}{8\pi^2} \int_{-\infty}^{\infty} \int_{-\infty}^{\infty} d\alpha \, d\beta \, e^{i\alpha x} \, e^{i\beta z}$$

$$\times \left[e^{\sqrt{\alpha^2+\beta^2}(y-a)} j_x^a(\alpha, \beta) - e^{\sqrt{\alpha^2+\beta^2}(y+a)} j_x^{-a}(\alpha, \beta) \right]$$

Because the current densities in the $y = a$ and $y = -a$ planes are symmetric for the magnetic field to reverse, $j_x^a(\alpha, \beta) = j_x^{-a}(\alpha, \beta)$. Thus the expression is simplified

$$B_z(r) = -\frac{\mu_0}{4\pi^2} \int_{-\infty}^{\infty} \int_{-\infty}^{\infty} d\alpha \, d\beta \, e^{i\alpha x} \, e^{i\beta z} \, j_x^a(\alpha, \beta) e^{-a\sqrt{\alpha^2+\beta^2}} \sinh\left(y\sqrt{\alpha^2 + \beta^2}\right),$$

after which an inverse Fourier transform is computed to solve for the current density J_x^a at the current planes which yields the desired magnetic field B_z at the target plane.

A MATLAB script was written implementing the above equation, in which the user defines a desired magnetic field and a cutting pattern is generated. The first step is to determine the coil geometry. To fit within the system gradient coil at the MRSL which has an inner diameter of 26 cm, the two current planes were separated by 8 cm (a = +/- 4 cm), allowing a maximum gradient coil width of 12.4 cm. The target field was defined to produce an error of 5% over the central 7 x 7 cm of the target plane. Because

of the equal current in the top and bottom coil planes defined above, the reversal of the field and its gradient along y is enforced and is not considered in the targeting except in location of the target plane. Because the field at the y = 0 mm plane is zero, the y = 0.1 mm was selected to place the targeted region in the center of the phantom. The target field must therefore have a gradient in x and sufficient apodization to be well conditioned for Fourier transformation and to yield a realizable current distribution [74]. A Gaussian filter was applied to the ideal x gradient field for apodizaiton. Also the integral of the B_z field along z must be zero so the cutting pattern will include current return paths. The target functions and a surface plot of the gradient of the target field are shown in Fig. 18. The x current density producing the targeted magnetic field and the z current density determined by applying the continuity relation are shown in Fig. 19.

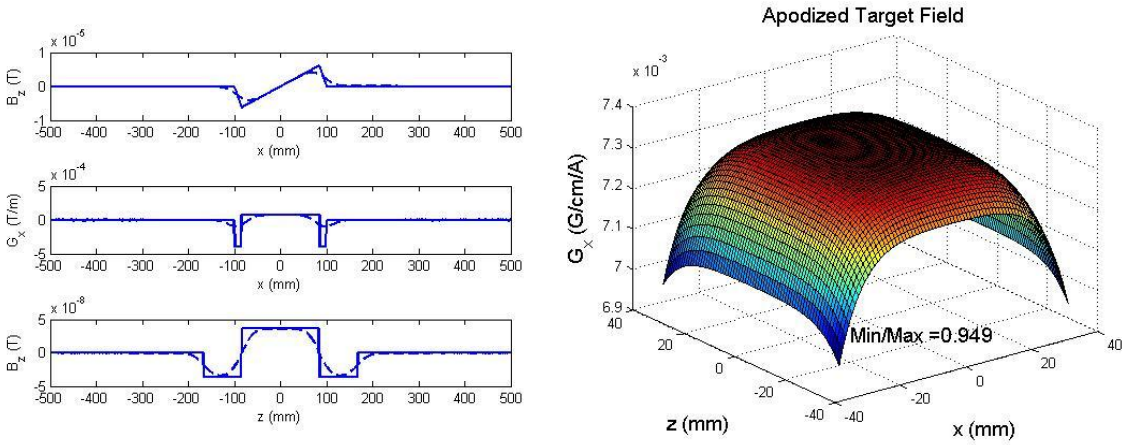

Fig. 18. Targeted magnetic field and x-gradient. Targeted field and gradient at the y = 0.1 mm plane (left) and surface plot of the targeted field (right). The dashed lines are the desired field after apodization by a Gaussian window. The fall-off over the central 7 x 7 cm is 5.1%.

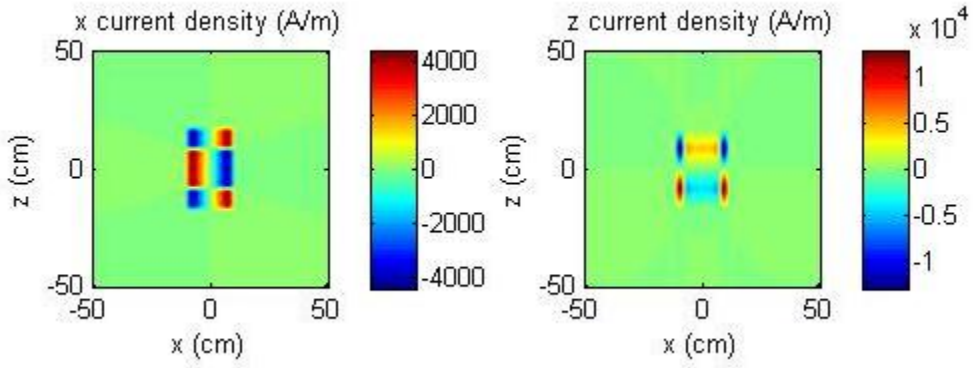

Fig. 19. Current density producing target field. X and Z components of the current density producing the targeted z directed magnetic field with x gradient shown in Fig 18.

3.4.2 Generation of the Cutting Pattern

To realize the continuous current distribution above, which yields the desired magnetic field, the distribution must be discretized into either a winding or cutting pattern. A winding pattern is used if the distribution is realized by a wire placed in grooves or around a former while a cutting pattern is used if the distribution is realized by removing conductive strips from a solid conductive sheet, such as with printed circuit board techniques [75]. To determine the discrete pattern, first a stream function ψ is found [76] by integrating the current density, with x and z components of the current density related to the stream function by the equation

$$\mathbf{J} = \nabla \times \psi \hat{\boldsymbol{a}}_{\boldsymbol{y}}.$$

The cutting pattern is determined by finding the locations of equally spaced contours of the stream function. This can be done using MATLAB's built-in "contour" function, the output of which is shown in Fig. 20. The number of contours is selected to achieve the desired sensitivity with more turns yielding a more accurate approximation of the

continuous current distribution. The contour lines are then exported in a format which can be converted and imported into a printed circuit board editing software, after which "jogs" are manually added to connect the concentric current paths as shown in [77]. Sixteen turns were found to give sufficient accuracy to produce a gradient of the desired linearity and sensitivity, with a 4 ms half sine pulse of 10.8A providing the target ±25 rad/cm over a 1cm slab.

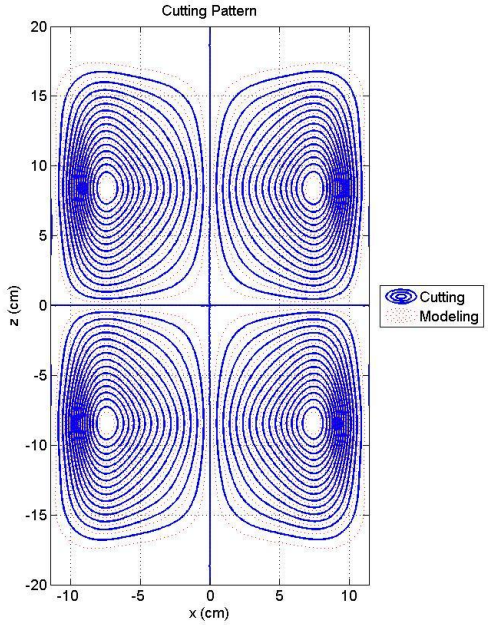

Fig. 20. Contour plot of the stream function of the current densities. Sixteen equally spaced contours are plotted in each quadrant. The blue traces are the cutting pattern, while the dotted red traces are the lines used for simulation of the field.

3.4.3 Construction

The coil was realized using 4 oz copper clad printed circuit boards, with the pattern printed on both sides for added sensitivity and more convenient connection of the feed lines to the coil. By milling the pattern on both sides of each circuit board, the current path finishes at the same place it starts, allowing easier connection of the power lines. The total coil geometry was divided into four sections, all the same by symmetry, which were milled using the LPKF machine. These were initially affixed between half inch and quarter inch thick acrylic sheets using nylon bolts. The biplanar coil was then assembled by holding the two acrylic sheets a fixed distance apart by nylon bolts and nuts, keeping the two current planes separated by 8 cm, as shown in Fig. 21. For initial testing, a twisted pair of wire was used to connect the coil segments, but this was replaced with coaxial cable for better containment of the magnetic flux of the cables and for added flexibility. The measured resistance and inductance of the coil are 2.7 Ω and 477 μH, respectively. No cooling was included in this coil as little heating was observed at the duty cycles used for testing (less than 2%).

Fig. 21. Prototype biplanar target field gradient coil before integration into an imaging probe.

3.4.4 Verification of Field

The gradient fields realized by simulating the contour lines between the cutting lines shown in Fig. 20 are shown in Fig. 22. The plots indicate significantly improved linearity compared to the uniplanar coil, and better than that indicated by simulating two Cho-type coils in a biplanar configuration. A set of phase images was acquired with the MR scanner to verify the linearity of the gradient field. An initial reference image was acquired with the fourth gradient disabled. This was followed by an image with the fourth gradient set to produce +/- 16 rad/cm over a 1 cm slab. The phase of these images was subtracted to remove effects of inhomogeneity of the static B0 field, leaving only the effect of the fourth gradient pulse, shown in Fig. 23. By extracting a row at the top and bottom of this image and unwrapping the phase, two linear plots are obtained, shown in Fig. 24. After minor adjustment of calibration constants, the slopes of these plots indicate that the coil is producing the expected gradient field

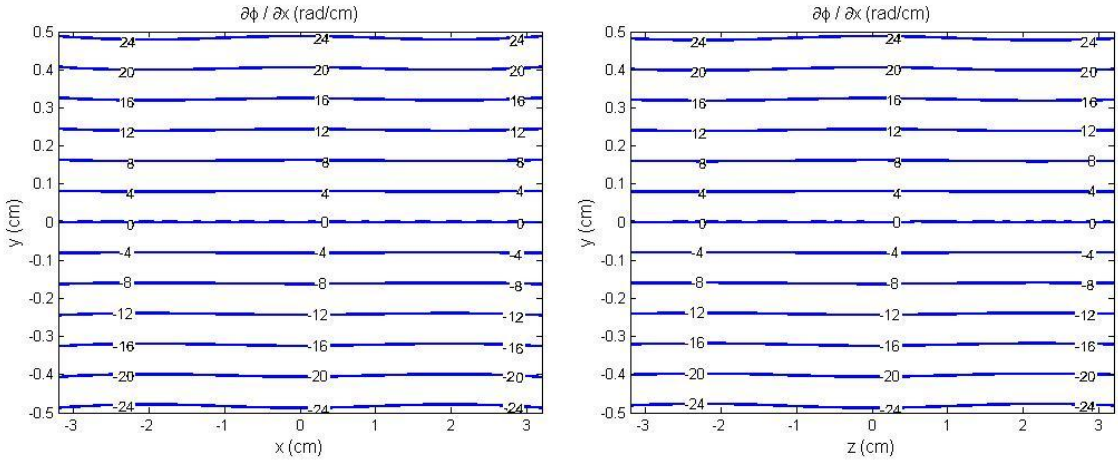

Fig. 22. Simulated fields of the stream function resulting from the target field calculations. The "simulation" lines indicated in Fig. 20 were used for these calculations.

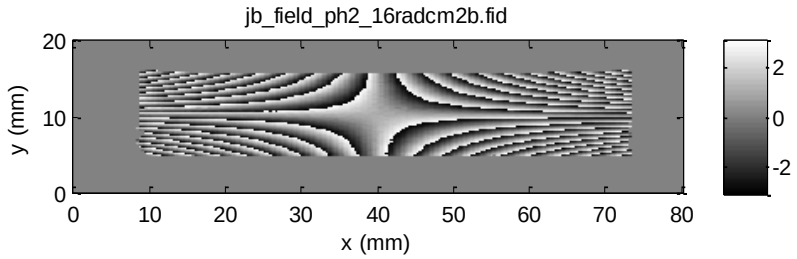

Fig. 23. Phase image from a transverse slice of a uniform phantom after a pulse from the target field gradient coil. The pulse was set to produce +/- 16 rad/cm over a 1 cm slab. This is the resulting image after subtracting a reference phase image. The pattern appears to match that of the target magnetic field in Fig. 8.

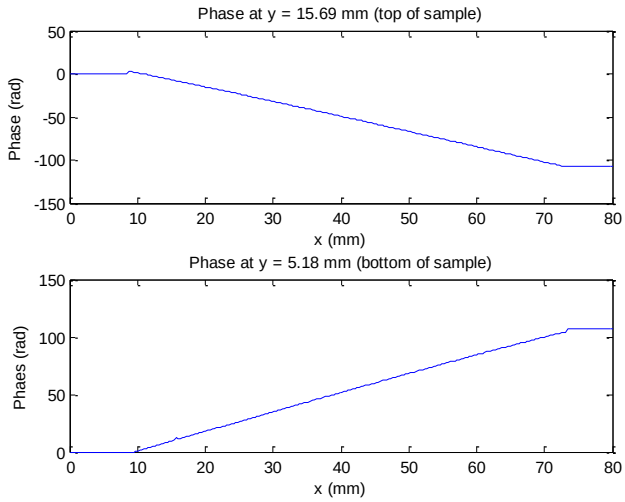

Fig. 24. Unwrapped phase from the top and bottom rows of the phase image. The top plot is from the y = 15.7 mm row in the above phase image, and the slope is -17.2 rad/cm. The bottom plot is from the y = 5.2 mm row in the above phase image, and the slope is 16.4 rad/cm. The phase variation over a 1cm slab is ± 16 rad/cm.

3.5 Through-slice Gradient

A complication in using the described coils for phase compensation is that any coil producing an x gradient with a y dependency also produces a y gradient with an x dependency. Because images are typically acquired parallel to the receive array surfaces which are parallel to gradient coil surface, this x dependent y gradient presents as a "through slice" gradient and creates a phase variation through the thickness of imaged slice. This phase variation is not uniform but varies along the x direction, increasing linearly toward the ends of the field of view. This can be understood by considering the desired field given above and computing the y derivative rather than x

$$B_z = kxy$$

$$\frac{\partial B_z}{\partial y} = kx = G_y(x).$$

Therefore, if the fourth gradient is set to produce an x phase gradient of ±25 rad/cm over a 1 cm slab, such that $k = 50\ \mathrm{rad/cm^2}$, it must also produce a y phase gradient of ±160 rad/cm over the 6.4 cm FOV along the x direction, as shown in Fig. 25. It is important to note that this undesired or "concomitant" gradient is not inherent to the gradient coil, but is a consequence of the phase distribution generating the desired gradient. Whether the distribution is imparted by a gradient pulse or a multidimensional RF pulse, the x dependent y phase gradient will occur. Fig. 26 illustrates how a phase distribution having a y varying x gradient must also have an x varying y gradient. One way to correct for RF coil phase while avoiding this problem would be if the phase of each array element is corrected with by a local phase gradient in the sample, repeating for each coil element. Parallel transmission is capable of this [78], but it is unlikely that a multidimensional RF

pulse or field due to a gradient coil could correct this, as it would require many sharp variations in the phase distribution.

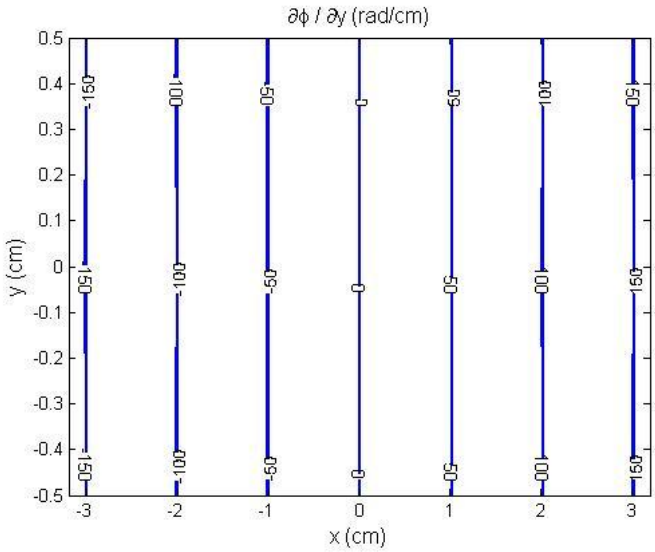

Fig. 25. X dependent y phase gradient also produced with the desired y dependent x gradient.

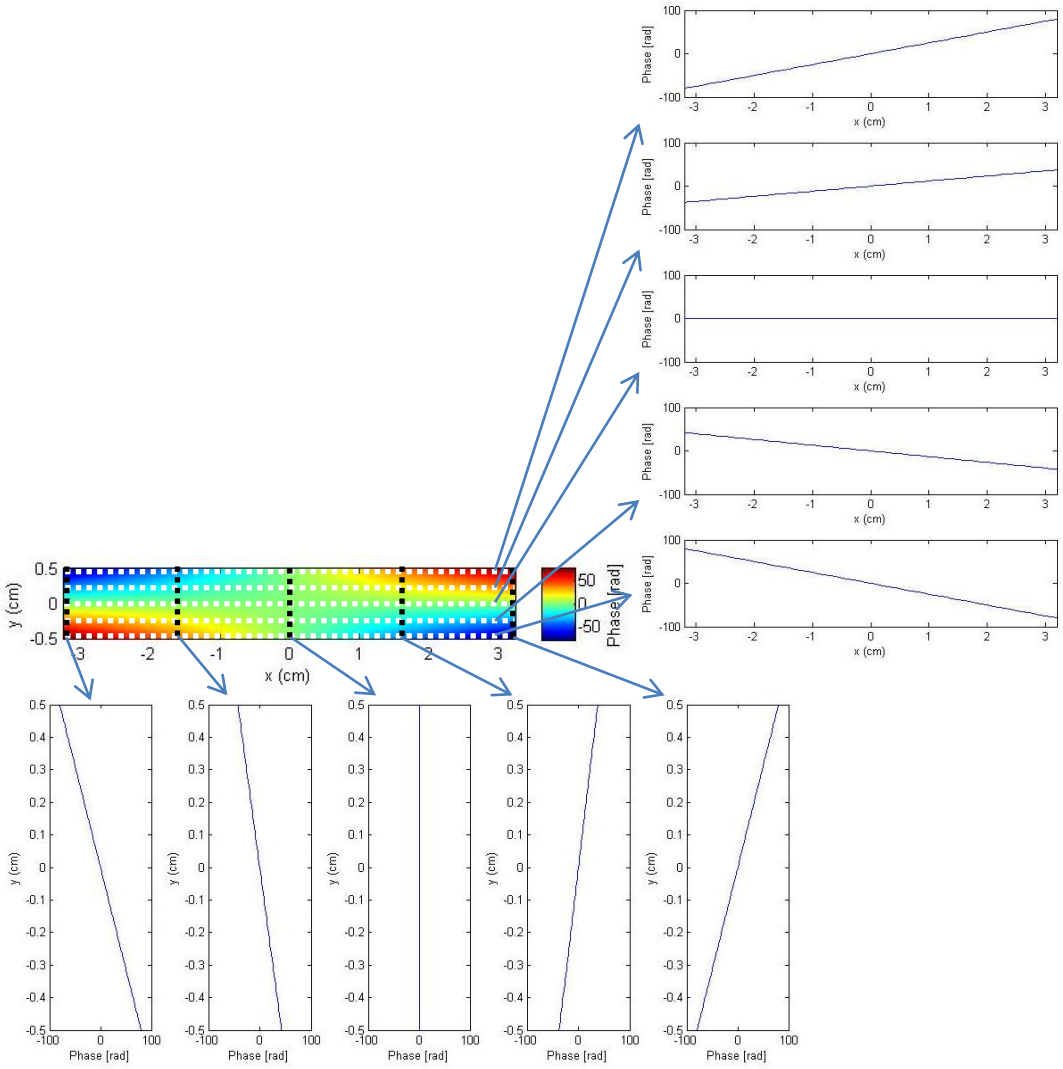

Fig. 26. Phase distribution in sample and in several lines along x and y. The white lines and associated phase plots show the desired y dependent x phase gradient, while the black lines and plots show the unavoidable x dependent y phase gradient.

When images acquired using the uniplanar fourth gradient coil offset by the main gradient for phase compensation were found to have a limited field of view, it was initially thought due to the non-linearity of the gradient field. However images had also been acquired using only the uniplanar gradient for phase encoding, which returned the full field of view with only some distortion near the edges, shown in Fig. 27. Considering that the problem may be due to an unwanted through-slice gradient, the amplitude of the slice select refocusing pulse was manually varied by modifying the spin echo pulse sequence. This caused the visible portion of the field of view to move, as the properly refocused area was moved as shown in Fig. 28 [79]. This confirmed that the fourth gradient was creating an unwanted through-slice gradient, resulting in signal cancellation. The source of signal cancellation due to a phase gradient through the thickness of a slice is illustrated in Fig. 29.

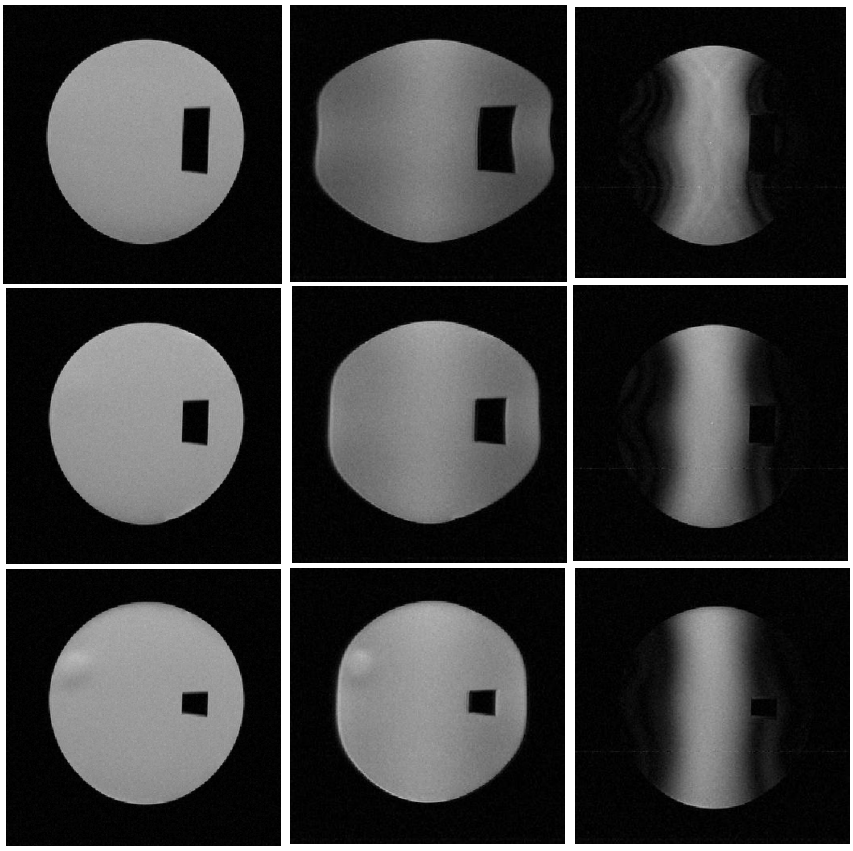

Fig. 27. Effect of through-slice gradient with uniplanar gradient coil. Images acquired at three slices with the main gradient only for phase encoding (left), with the Cho-type uniplanar gradient only for phase encoding showing some distortion due to gradient nonlinearity (middle) and with the uniplanar gradient set to 0.8 G/cm and the main gradient phase encoding table offset by the same amount (right). Loss of FOV only occurs when the fourth gradient is used with the system gradient to create the desired y dependent x gradient.

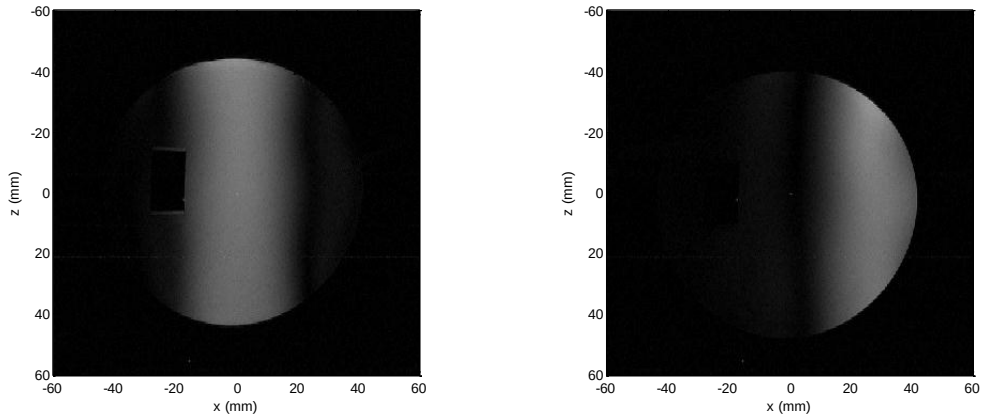

Fig. 28. Effect of modified refocusing pulse on image intensity. Restricted field of view image when employing the fourth gradient for phase compensation (left). Result of decreasing the slice select refocusing pulse by 50% (right). This shows that the through-slice gradient is adversely affecting refocusing [79]. (© 2010 IEEE)

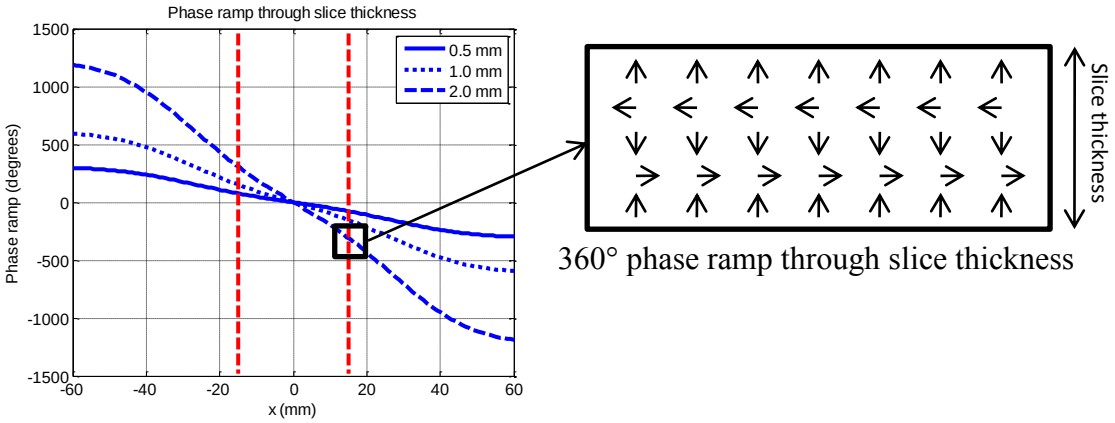

Fig. 29. Phase gradient through the thickness of the slice due to a pulse of the uniplanar gradient coil. As the phase gradient increases linearly in the x direction, at the points where the phase gradient is 360° there is complete cancellation, creating a signal null.

This loss of field of view due to the through-slice gradient can be estimated by integrating the signal through the thickness of a uniform slice

$$S(x) = \int_{\substack{slice \\ thickness}} e^{j\phi_{comp}(x,y)} dy$$

where $S(x)$ is the total received signal at a position x and $\phi_{comp}(x,y)$ is the phase at position (x,y). The phase produced by a pulse of the desired field $G(x,y)$ is expressed as:

$$\phi_{comp}(x,y) = \phi xy$$

where ϕ is in rad/cm^2. Carrying out the integration gives the expression of the signal along the x direction in the presence of the x dependent through-slice gradient,

$$S(x) = \int_{-\frac{st}{2}}^{\frac{st}{2}} e^{j\phi xy} dy$$

$$S(x) = \frac{1}{j\phi x}\left[e^{j\phi x\frac{st}{2}} - e^{-j\phi x\frac{st}{2}}\right] = \frac{2\sin\left(\phi x\frac{st}{2}\right)}{\phi x}$$

$$|S(x)| = \left|\frac{2\sin\left(\phi x\frac{st}{2}\right)}{\phi x}\right|.$$

An image obtained from a 1.5 mm thick slice with the fourth gradient set to produce an x phase gradient of +/- 20.1 rad/cm over a 1 cm thick slab exhibits the reduced field of view due to the through-slice gradient, shown in Fig. 30. Comparing a row of this image to the signal estimated by the formula, side by side in Fig. 31, shows agreement. In 2D imaging, field of view loss due to the fourth gradient can be mitigated by constraining the slice thickness as shown in Fig. 32. For a phase gradient of +/- 25 rad/cm over a 1cm slab, for instance, constraining the slice thickness to 0.24 mm will result in a 50% loss of signal at the edges of the 6.4 cm field of view along x. By normalization, the image intensity can be maintained, resulting in a loss of SNR at the edges, a trade-off when imaging using this method.

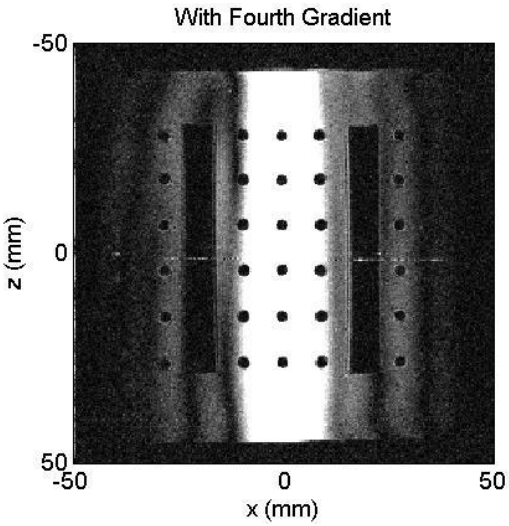

Fig. 30. Restricted field of view image using the biplanar fourth gradient coil. Image obtained with fourth gradient set to produce an x phase gradient of 20.1 rad/cm over a 1 cm slab using a 1.5 mm slice thickness.

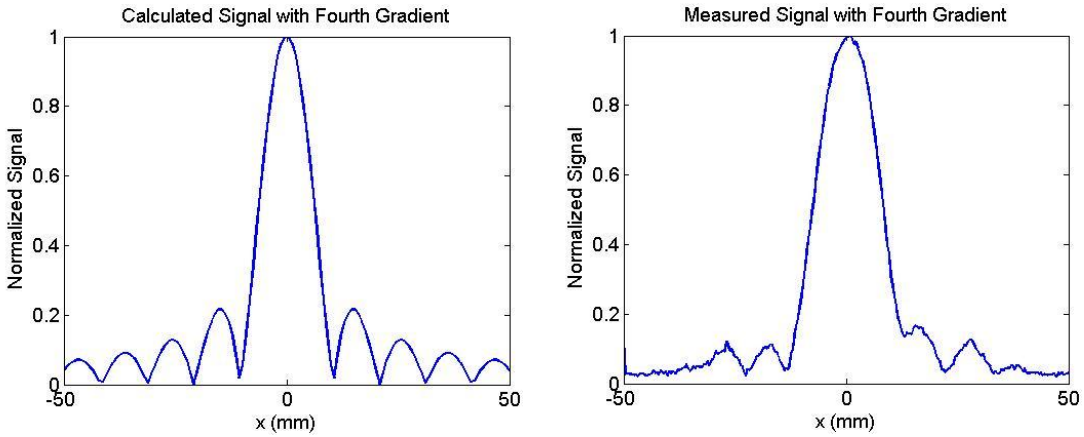

Fig. 31. Calculated and measured signal intensity along the x direction with fourth gradient. Current set to produce an x phase gradient of +/- 20.1 rad/cm over a 1 cm slab for a slice thickness of 1.5 mm.

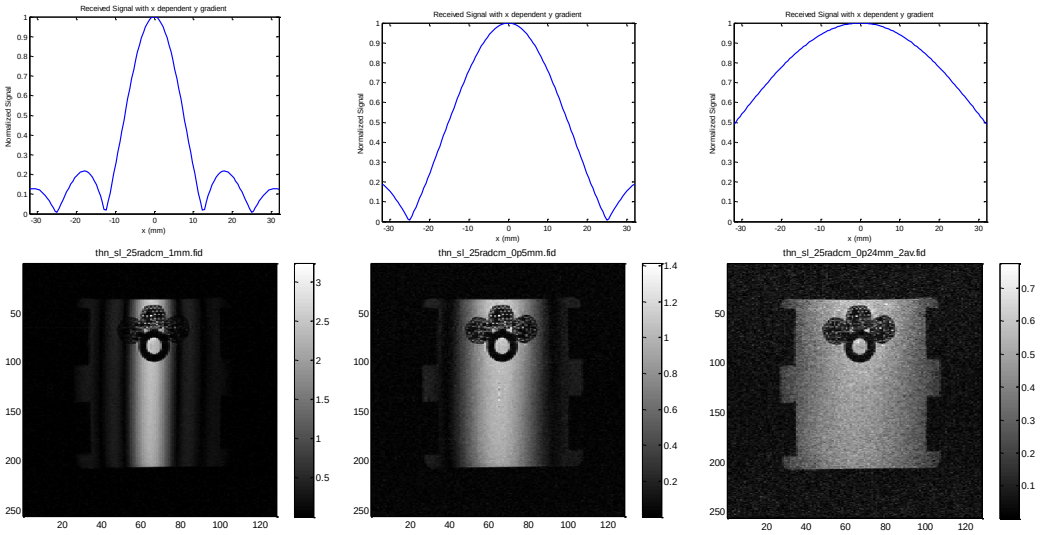

Fig. 32. Effect of slice thickness on through-slice gradient artifact. Calculated image intensity over a 6.4 cm x field of view (top) and images obtained of a 6.4 cm x 6.4 cm phantom with the fourth gradient set to produce +/- 25 rad/cm over a 1 cm slab with slice thickness of 1 mm (left), 0.5 mm (middle) and 0.24 mm (right). Constraining the slice thickness restores the field of view lost due to the through slice gradient [51]. (© 2012 IEEE)

This concomitant gradient also has an adverse effect on 3D imaging. While the desired y varying x phase gradient corrects the offset in x *k*-space caused by the RF coil phase, the x varying y phase gradient causes an offset in the acquired y *k*-space, increasing towards the edges of the field of view along x as illustrated in Fig. 33. This demands a higher resolution in the y direction so that the offset introduced in y *k*-space is not detrimental to imaging. For example, a fourth gradient pulse producing an x phase gradient of ±25 rad/cm over a 1 cm slab along y also produces a y phase gradient of ±160 rad/cm over the 6.4 cm FOV in the x direction. For a 0.5 mm resolution and a 1.6 cm field of view along y, *k*-space is sampled from -62.8 to 58.9 rad/cm in 3.93 rad/cm steps. Because the fourth gradient pulse would offset the center of y *k*-space beyond the

sampling range at the edges of the field of view in x, much of the y spatial frequencies including the DC component of the images will not be collected, leading to significant artifacts. To keep the offset of y *k*-space under 20%, an arbitrary metric, the following expression can be evaluated to determine the necessary resolution

$$\frac{k(6.4\ cm)}{\frac{2\pi}{FOV_y}N_y} < 0.2$$

where N_y/FOV_y is the resolution in pixels per cm and k is the phase variation produced by the fourth gradient coil in rad/cm^2. For typical phase compensation values of ±12 to ±25 rad/cm over a 1 cm slab, the value of k ranges from 24 to 50 rad/cm^2. For a typical y field of view of 16 mm, the number of phase encode steps necessary to limit the offset of y *k*-space to 20% ranges from 197 to 410. The amount of acceptable offset in the y *k*-space depends on the acceptable artifact power in a particular sample, which can be determined for different experiments.

The effect of using an insufficient number of y phase encode steps is shown in the 3D volume coil dataset in Figs. 34 and 35. Applying a fourth gradient pulse generating ±25 rad/cm over a 1 cm slab and imaging with a resolution of 390 μm x 390 μm x 312 μm, the signals from the edge of the field of view along x are lost beyond x = 2 cm, where the center (DC component) of *k*-space along the y direction is no longer collected due to the unwanted offset produced by the fourth gradient coil.

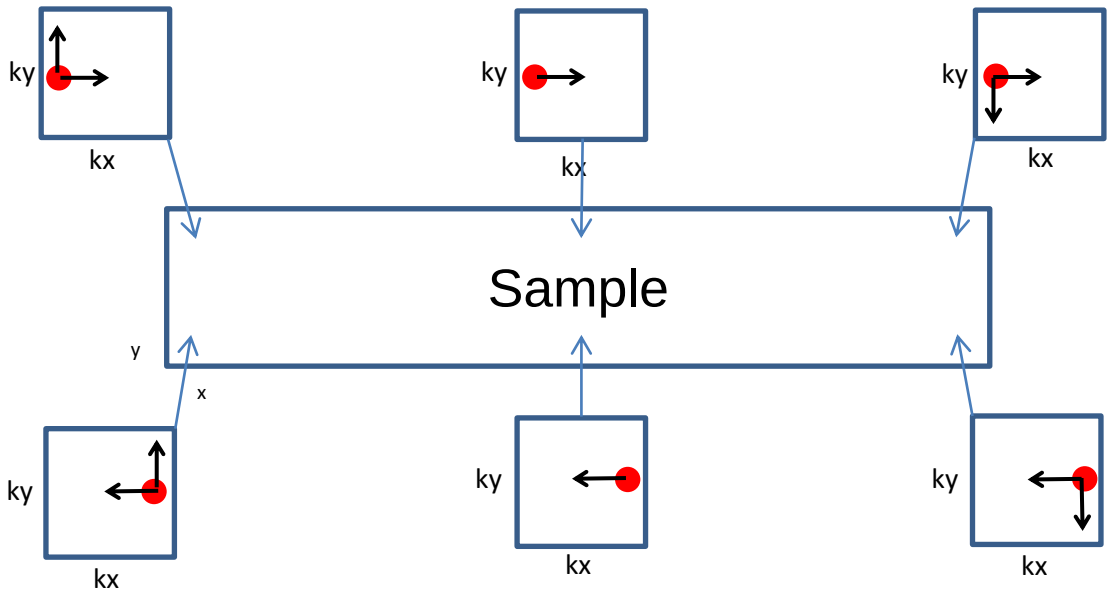

Fig. 33. Effect of fourth gradient on *k*-space in 3D imaging. *k*-space offset due to the bottom and top RF coil arrays (red dots) and correction due to an applied fourth gradient pulse in 3D imaging (black arrows). The offset in x *k*-space is corrected, but a new x dependent offset in y *k*-space is introduced.

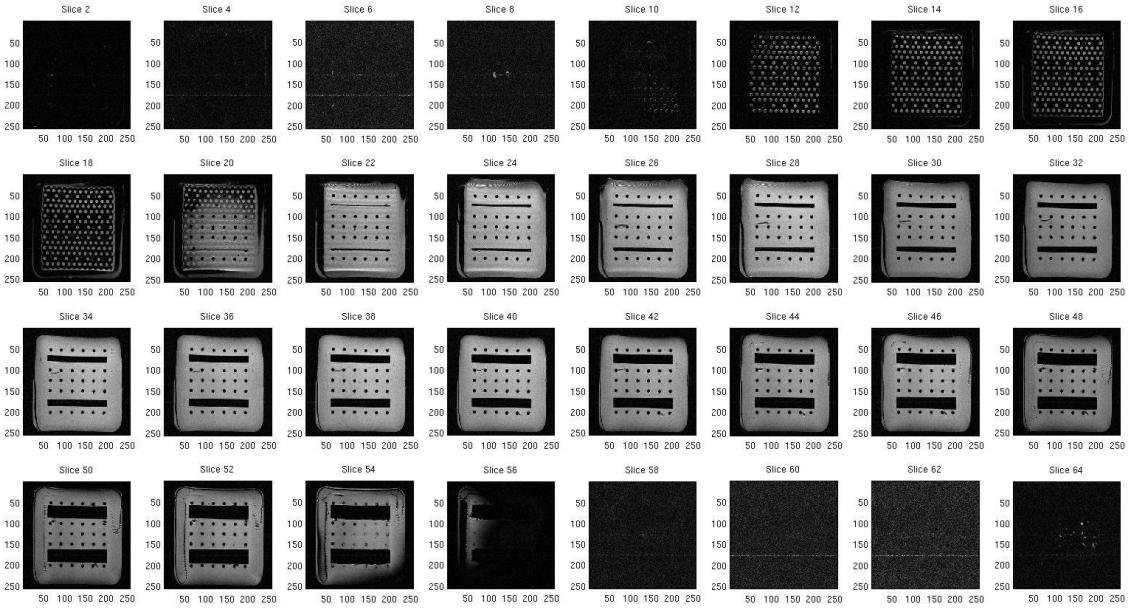

Fig. 34. 3D volume coil data without fourth gradient. The full field of view is visible.

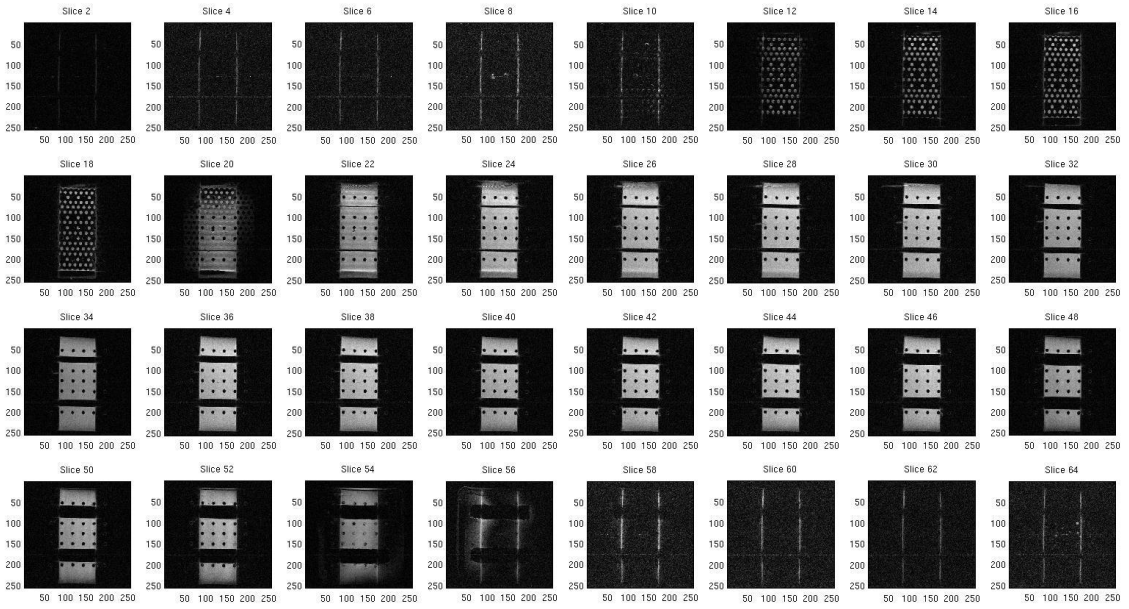

Fig. 35. 3D volume coil data with fourth gradient. When the fourth gradient is set to generate ±25 rad/cm over a 1 cm slab and y *k*-space is sampled from -100.5 to 97.4 rad/cm, the regions along x where the x dependent y gradient has shifted the center of *k*-space beyond the sampling range return little or no signal.

4. WIDE FIELD OF VIEW IMAGING SYSTEM

4.1 Imaging Probe

The target field biplanar gradient coil discussed above was integrated with a volume RF coil for excitation and a platform for loading various samples and receive arrays, forming a single probe for wide field of view imaging over a range of spatio-temporal regimes [80]. The probe, shown in Fig. 36, is placed with the imaging region of the fourth gradient coil centered within the imaging region of the main gradient coil. Two polycarbonate cradle pieces with rubber feet are affixed to the bottom of the probe along with two cam-type clamps on the top. The clamps were added due to the probe position shifting within the bore of the magnet during pulsing. Once the probe is placed in the magnet, several images are acquired to ensure that the coordinate systems are aligned. After adjusting the position of the probe, it is locked in place. In order to mitigate vibrations, the inner acrylic pieces which held the coil circuit boards in place were replaced by unclad FR-4 boards which were affixed to the gradient coil boards by epoxy, adding some rigidity. Increasing the duration of the gradient pulses also reduces vibrations.

Because precise placing of the probe within the main gradient coil is a time consuming process, the probe was designed such that the receive array and sample could be removed while leaving the remainder of the probe in the magnet. This facilitates comparison of different receive array coil geometries as well as faster loading of samples, which is important as some biological samples may have a limited viability.

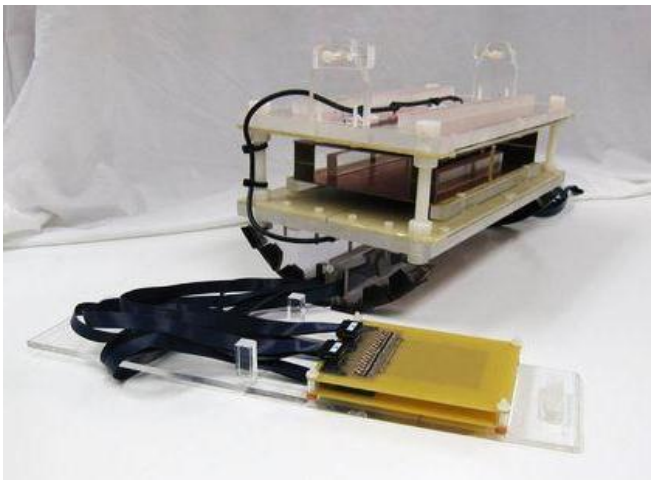

Fig. 36. Photograph of wide field of view imaging probe. The probe consists of the biplanar gradient coil and acrylic former with integrated volume RF excitation coil, shown with the dual sided receive array and loading platform removed [79].

4.1.1 Volume Excitation Coil

The volume excitation coil, illustrated in Fig. 37, is based on a parallel plate resonant structure previously used by our group for SEA imaging, similar to the ribbonator described by Marshall et al. [81]. The boundary conditions at the top and bottom conductive plates force the $B_{1,y}$ field (normal to the plates) to 0 within the structure and maintain uniformity in the $B_{1,x}$ field. An L-network at the feed point was implemented to tune and match the coil to 50 ohms, with a PIN diode added across the tuning capacitor to allow active detuning of the coil to minimize coupling to receive arrays during signal reception. The width of the aperture for inserting the sample and arrays affects the B_1 uniformity of the coil, with a wider aperture resulting in a decrease of the B_1 field in the center of the coil along the x direction. To maintain field uniformity over a 6.4 x 6.4 cm imaging region, the coil was made somewhat larger, measuring 30.5

x 17 cm, with an aperture width of 11.5 cm. The location of the peak B_1 field was moved away from the aperture using 4.7 pF capacitors at the gaps adjacent to it. The measured B_1 field along the center of the coil and offset by 4 cm is shown in Fig. 38. By centering the sample 15 cm from the opening, a variation of 0.3 dB is achieved over a 6 cm imaging region. Narrow, 16 cm long slits in the copper were added to mitigate eddy currents induced by the fourth gradient coil after observing distortion in the images. The problem and improvement due to the slits are shown in Fig. 39.

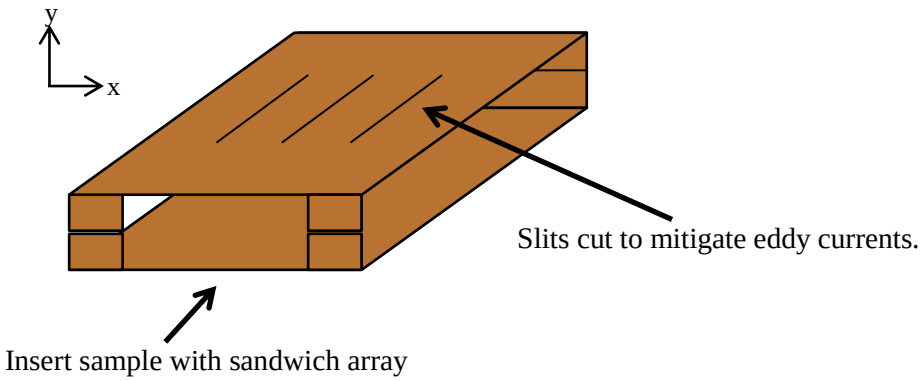

Fig. 37. Drawing of RF excitation or "volume" coil. A loading platform supporting the sandwich receive array and sample are inserted into the aperture in the volume coil.

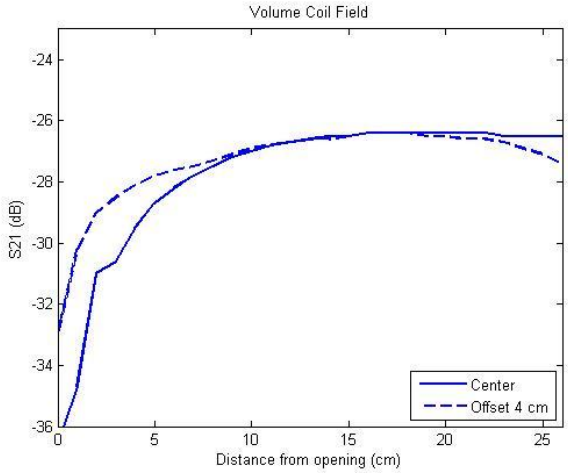

Fig. 38. Network analyzer S21 measurement of the RF magnetic field within the volume coil. Measurements were made using a shielded detection loop before slits were added. The uniform region is centered around 15 cm from the aperture.

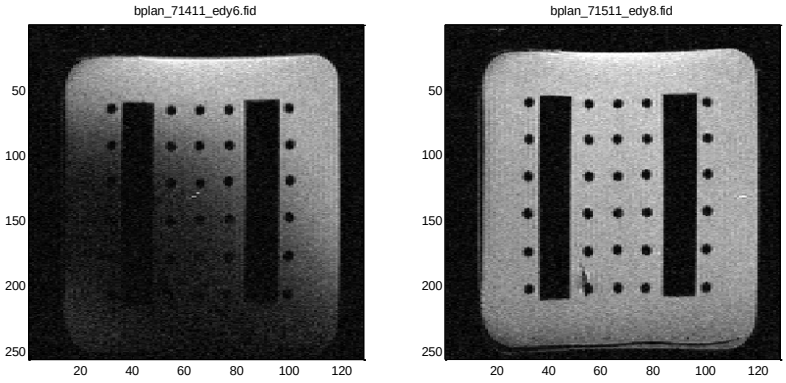

Fig. 39. MR images showing effect of eddy currents induced in the volume coil by the fourth gradient coil. Images were acquired with the standard Varian pulse sequence preceded by 4 ms, 8.06 A pulse of the fourth gradient coil. A loss of signal occurs due to eddy currents (left). Same image after adding narrow slits in the excitation coil (right), as illustrated in Fig. 37.

4.1.2 Dual-sided Receive Arrays

Two prototype dual-sided arrays have been constructed for use with this system. One employs the standard planar pair element geometry successfully used by our group for SEA imaging [41] and MR microscopy [8]. This geometry offers superior isolation between coils, which is especially important in SEA and the most accelerated imaging cases. However, the planar pair element suffers from relatively poor penetration depth. Another prototype tested employs a dual-plane pair geometry [82, 83], very similar to the planar pair except that the current return paths are located on the opposite side of the printed circuit board. This facilitates a greater penetration depth but at the expense of a broader field pattern and increased coupling between coil elements, requiring use of additional decoupling transformers. The planar pair coil was used in all results shown below as SEA and highly accelerated imaging, demanding of confined B1 patterns, are the applications requiring the fourth gradient coil.

4.1.3 Cables and Coupling

Upon initial insertion of a dual sided receive array into the parallel plate volume coil, it was found that the volume coil was detuned significantly and could no longer be impedance matched to 50 ohms. Furthermore, the input impedance of the volume coil was highly affected by the placement of the Blue Ribbon cables connected to the receive array. The dual sided receive arrays are made up of unbalanced coils with all coils sharing a common ground and each array containing a large ground plane. By connecting the blue ribbon cables to both arrays, the ground planes of the arrays are connected at some distance from the coil by the common mode currents of the Blue

Ribbon cables, adversely affecting the fields in the volume coil. In order to avoid this, a pair of current suppression traps similar to those described by Seeber at al. [84] were implemented, improving the stability of the tuning of the volume coil. Also, a set of clips was placed beneath the gradient coil to allow keeping the cables stationary.

4.1.4 Controlling System

A LabVIEW virtual instrument was written to control a PCI-6221 card (National Instruments, Austin, TX) with two analog outputs [79]. The user inputs the desired phase gradient, slab thickness, pulse duration, pulse shape, and any desired initial delay, as shown in Fig. 40. A Varian spin echo pulse sequence was modified to generate a TTL output trigger at the beginning of the normal phase encode gradient pulse. This triggers the PCI-6221 card to generate a gradient pulse providing the desired phase compensation. The gradient waveform is output from both analog output channels as a differential signal, which is connected to the input of a Techron 8606 gradient amplifier. Both the Dell PC containing the output card and the fourth gradient amplifier are shown in Fig. 41, next to the standard three-axis gradient amplifier cabinet. The output of the gradient amplifier is passed through two filtered feed-through connectors mounted to the custom flange plate. An additional LabVIEW script was written to allow stepping through a table of fourth gradient values, allowing collection of 4D datasets for analysis of the effect of the fourth gradient coil.

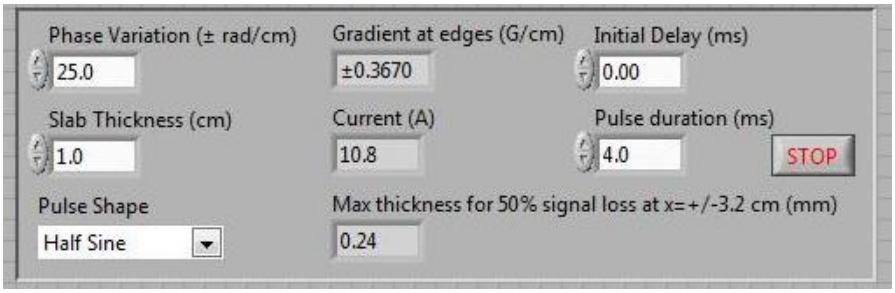

Fig. 40. Input control panel of the LabVIEW virtual instrument that controls the fourth gradient channel.

Fig. 41. Fourth gradient controller PC and amplifier. Shown to the right of the standard three-axis gradient amplifier system (since upgraded).

4.2 Acquired *k*-space

The ability of the fourth gradient coil to compensate for the phase gradient of a dual sided array was tested by acquiring images from of a set of slices parallel to and between two planar receive arrays separated by 1.3 cm. In these experiments, the stepped phase encoding gradient used in fully encoded imaging serves as a phase compensation gradient of varying amplitude for assessment of the effect of phase compensation on the received signals. The fourth gradient amplitude was also stepped such that a 4D matrix (read out, phase encoding, fourth gradient, slice) was acquired for analysis of the effect of the fourth gradient on the RF coil phase gradient. By plotting the normalized received signal strength from each array for different phase encode values, the ability of the fourth gradient coil to provide slice dependent phase compensation is evaluated. By using thin slices and comparing data from coils near the center of each array, any deleterious effect of the through-slice gradient was avoided.

The plots in Fig. 42 are extracted from a fully encoded *k*-space matrix along the phase encoding direction, with each trace using the same frequency encoding point. The plots show that a pulse from the fourth gradient collects the locations in *k*-space at which the peak signals from the bottom and top array planes occur. This allows more efficient signal reception from the two arrays, enabling SEA imaging from both arrays simultaneously if slices near each array are excited together. Furthermore, data for resolution enhanced imaging based on 2 or 4 *k*-lines near the peak of *k*-space can be collected from both arrays simultaneously, doubling the acquisition efficiency. As this acquisition employs an 80 mm field of view, each "*k*-line" represents a step of 0.785

rad/cm in phase encode gradient strength, with *k*-line 129 representing the center of *k*-space, or 0 rad/cm. Fig. 43 shows a set of fully encoded images through the thickness of the phantom, giving an indication of how much signal is available at each slice.

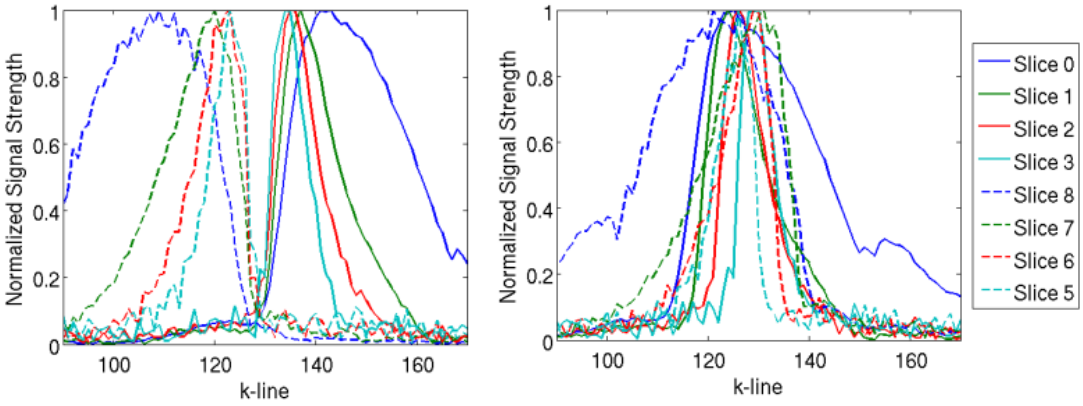

Fig. 42. Measured normalized received signal vs phase compensation gradient strength. The phase compensation is indicated by *k*-line number, collected without the fourth gradient (left) and with the fourth gradient set to produce +/- 12 rad/cm over a 1 cm slab (right). The solid lines represent signals received from a coil near the center of the bottom array, while the dashed lines are from coils near the center of the top array [51]. (© 2012 IEEE)

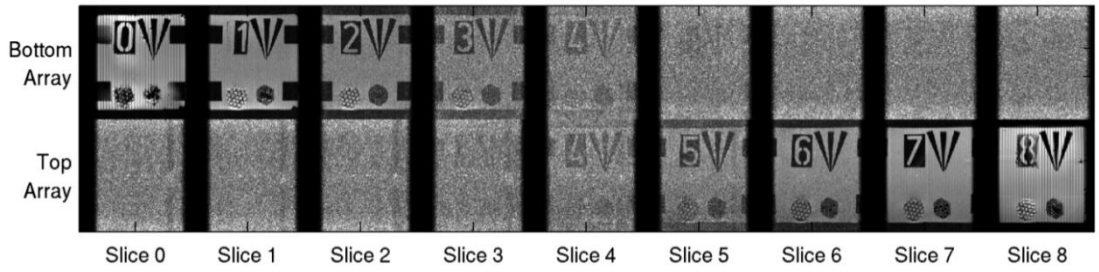

Fig. 43. Fully encoded reference images received by the sandwich array. Eight slices, labeled 0 through 8, were received using the bottom and top arrays. Using two arrays, signal is received from both sides of the sample, however the B1 pattern of both arrays has largely decayed at the center slice, resulting in little detected signal [51]. (© 2012 IEEE)

4.3 SEA Imaging Results

4.3.1 Multislice

The advantage of using the fourth gradient coil for phase compensation is primarily seen when receiving simultaneously from an array above and below a sample in a sandwich configuration. During such parallel reception, there is no compensation pulse from the main gradient which can simultaneously yield SEA images from the bottom and top arrays. In multislice sequences, several slices are acquired in a time series, each requiring a different phase compensation value based on its position relative to the bottom or top array. In principle a gradient table could be programmed such that the normal system gradient provides the proper phase compensation for each slice, however in some instances it may be desirable to simplify this process by using a single pulse from the fourth gradient coil to provide a suitable compromise phase compensation value to all slices (except the middle slice which necessarily receives no compensation due to the reversal of the fourth gradient field). A multislice dataset is also useful in studying the effect of the fourth gradient on SEA images at different slices to demonstrate the benefit it can provide when these slices are acquired in parallel.

A fully encoded multislice dataset was acquired with five fourth gradient amplitudes (0, ±4, ±8, ±12, ±16 rad/cm over a 1 cm slab), forming a 4D matrix allowing analysis of the effect of the RF coil phase gradient on images. A set of nine 0.5 mm thick coronal slices was acquired using a 2.5 s TR, 30 ms TE, 256 x 256 matrix, 80 x 80 mm field of view, and 50 kHz spectral width. The slices were separated by 1.275 mm, spanning the 1.3 cm thick phantom. Half-sine shaped 7 ms phase compensation pulses

were applied to the fourth gradient coil. The long duration was to reduce vibrations of the fourth gradient coil insert. Fig. 44 shows SEA images at different slices reconstructed retrospectively using a range of phase compensation pulses, indicated by *k*-line, without a pulse from the fourth gradient coil. These images show that with a phase compensation pulse from the main gradient, SEA images can be acquired using one array or the other, with slices from the bottom array requiring compensation gradients of *k*-line greater than 129 and slices from the top array requiring compensation gradients of *k*-line less than 129. The acquired images show that there is no single compensation pulse yielding images from both arrays, with only high spatial frequency information received from the side opposite of that properly compensated.

However, by applying a pulse from the fourth gradient coil, as shown in Fig. 45, SEA images are acquired from both arrays using the same compensation value. The acquired *k*-lines in this set are offset by 1 line to correct for an offset of the position of the sample within the fourth gradient field. This allows collecting multislice SEA images without altering the phase compensation pulse for each slice and enables dual-slice SEA imaging in which two slices are excited and received simultaneously.

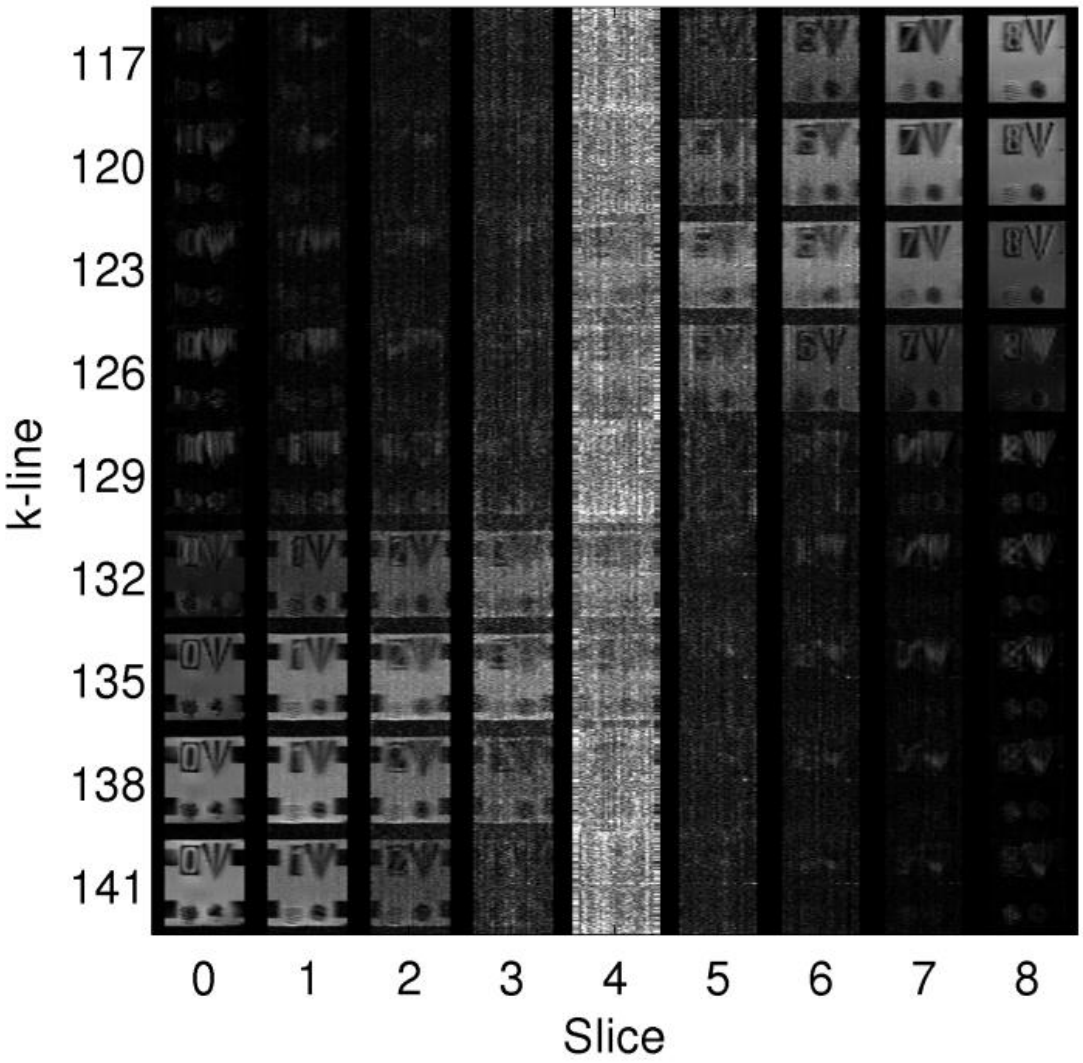

Fig. 44. Retrospective SEA images acquired without the fourth gradient. Images were reconstructed from the bottom array (slices 0-3), a combination of both arrays (slice 4) and the top array (slices 5-8) over a range of phase compensation gradient values, indicated by *k*-line number, without the fourth gradient for phase compensation. Images are obtained from the bottom array using *k*-lines greater than 129 and from the top array using *k*-lines less than 129, where 129 represents a compensation gradient strength of 0 rad/cm. No single compensation gradient value yields SEA images from both arrays [51]. (© 2012 IEEE)

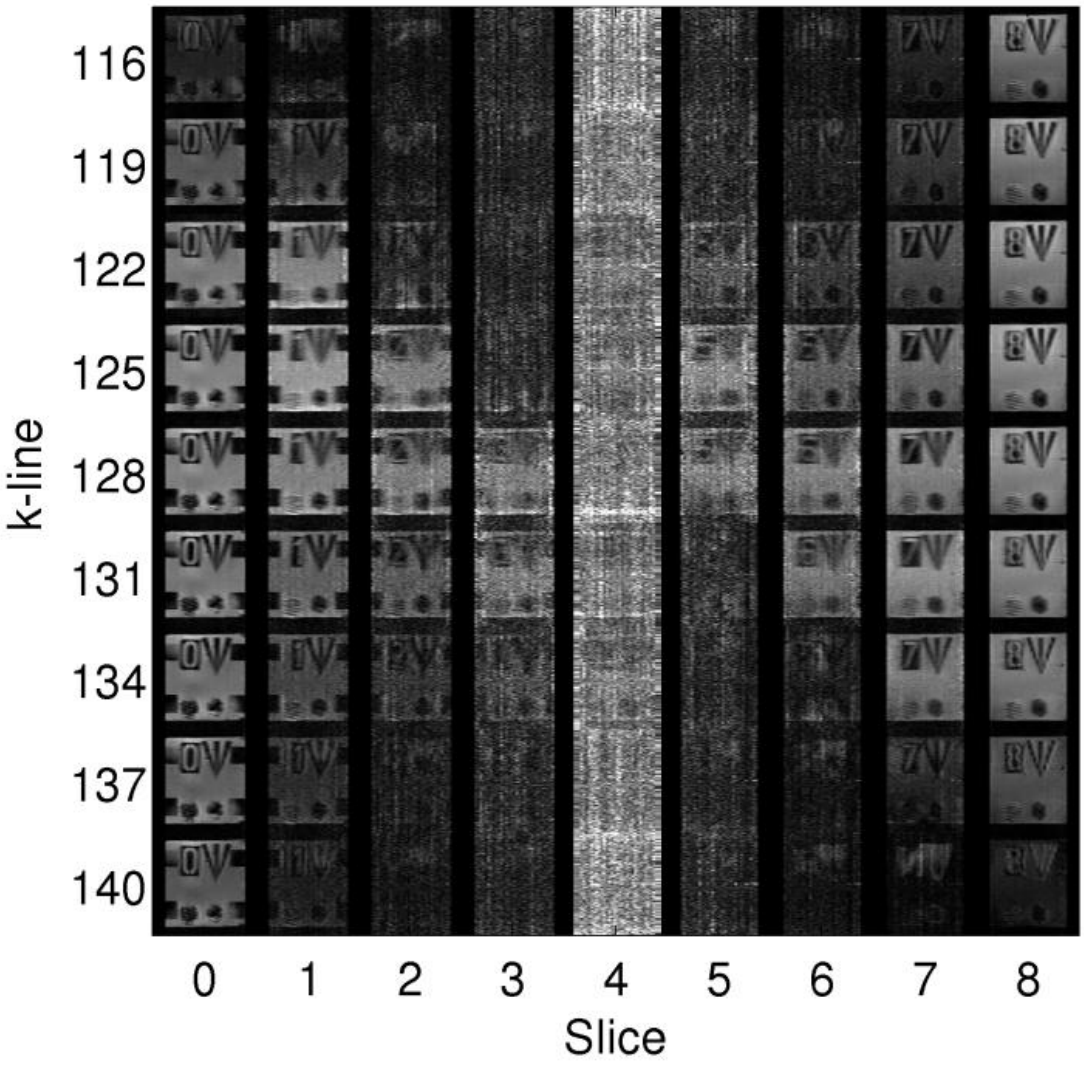

Fig. 45. Retrospective SEA images acquired with the fourth gradient. Images were reconstructed from the bottom array (slices 0-3), a combination of both arrays (slice 4) and the top array (slices 5-8) over a range of phase compensation gradient values, indicated by *k*-line number, with the fourth gradient set to produce +/- 12 rad/cm over a 1 cm slab. Images are obtained from both arrays using *k*-line 128, as slices from each array receive opposite compensation from the fourth gradient coil [51]. (© 2012 IEEE)

4.3.2 Dual Slice Imaging

To realize the increased acquisition efficiency arising from using the fourth gradient coil for phase compensation, signals must be received from both arrays simultaneously. This has been accomplished by modifying a sinc pulse to excite two narrow bandwidths corresponding to two thin slices, each offset from the center of the sample by equal and opposite amounts. This is accomplished by summing two sinc pulses modulated by positive and negative linear phase ramps, corresponding to positive and negative frequency shifts. Because of the confined B_1 sensitivity patterns of the bottom and top planar pair receive array elements, the bottom and top slices are not detected by opposite arrays, meaning that there is no interference when imaging from the two sides in parallel. Fig. 46 shows the time and frequency domain of a 4 ms RF pulse modulation producing the dual slice excitation, while Fig. 47 shows two volume coil images resulting from using this excitation.

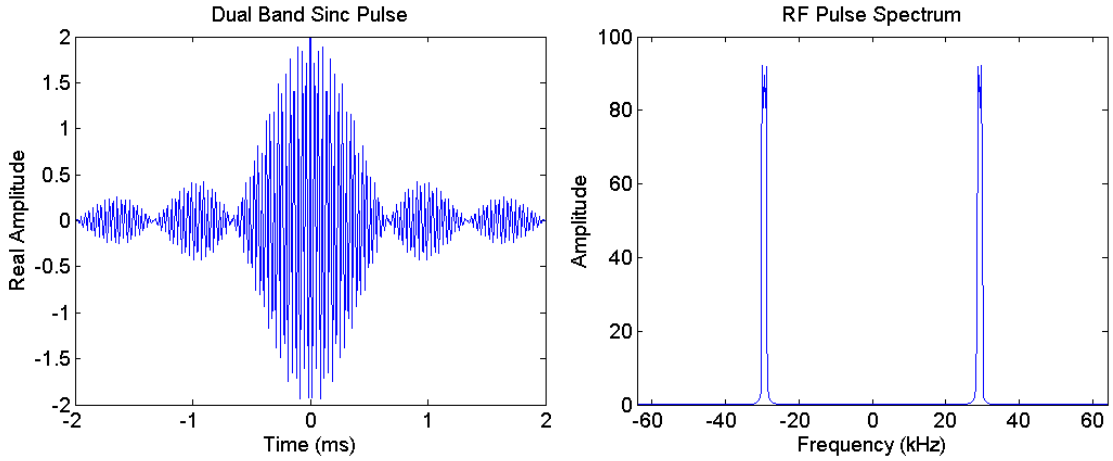

Fig. 46. Dual band sinc pulse and spectrum. The pulse simultaneously excites two thin slices, each offset from the center of the slice select gradient field by approximately 29 kHz. In a 14.1 G/cm gradient field, this corresponds to two slices separated by approximately 9.75 mm.

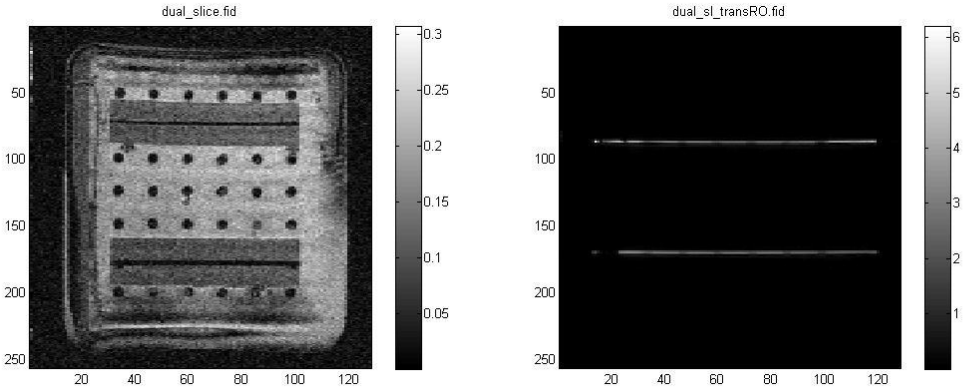

Fig. 47. Slices excited by the dual-band sinc pulse. Two slices in the xz plane simultaneously excited and received using a volume coil with frequency encoding along the z direction (left) and y direction (right). With frequency encoding along the z direction, the coronal image is the sum of the two excited slices. Moving the frequency encoding to the y direction yields a transverse image indicating two distinct excited slices.

Using a similar excitation in conjunction with a dual sided receive array, images were obtained with seven fourth gradient values for phase compensation (0, ±4, ±8, ±12, ±16, ±20, ±24 rad/cm over a 1 cm slab). All imaging parameters are the same as the multislice set above, except a TR of 500 ms was employed and the 180 pulse was replaced with a non-selective hard pulse. As shown above, without the fourth gradient channel, a phase compensation value can be selected to yield a SEA image from either the bottom or top array, but not both. Because the slices are equidistant from their respective receive arrays, each requires equal and opposite compensation, so the only possible compromise is to set the compensation gradient to 0. As shown in Fig. 48, this yields images from each array containing only high spatial frequency components. By enabling the fourth gradient channel, a single gradient pulse provides equal and opposite phase compensation to both slices, enabling simultaneous SEA imaging using both

arrays. This will allow monitoring rapid events which occur at the outer surfaces of the sample.

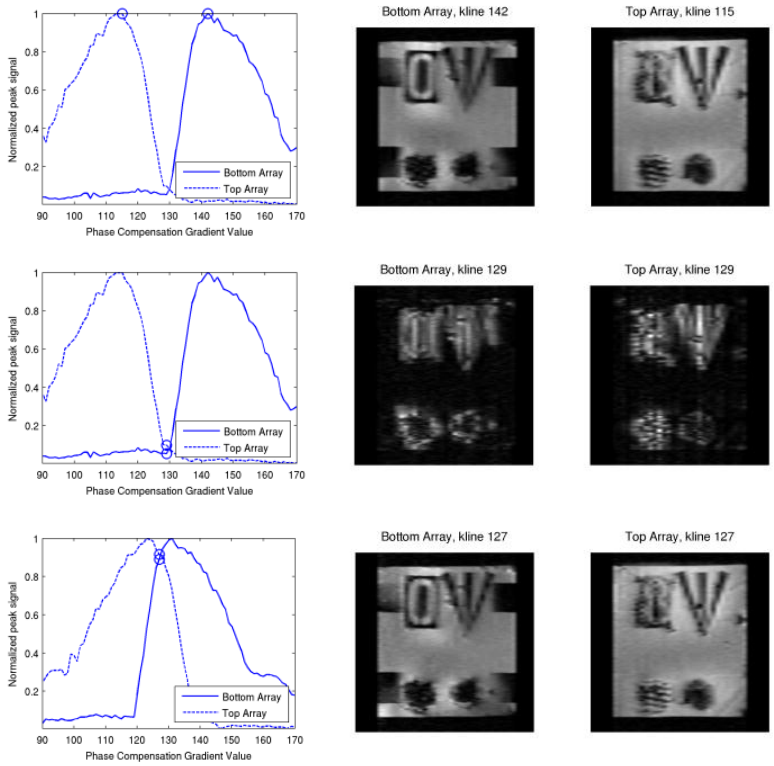

Fig. 48. Normalized peak signal vs *k*-line and SEA images received in parallel with and without the fourth gradient. The *k*-lines used for each reconstruction are indicated by the markers. The top row shows images obtained in two echoes without the fourth gradient coil, using *k*-line 142 for RF coil phase compensation for the bottom array image and *k*-line 115 for the top array image. The middle row images were obtained in one echo without the fourth gradient using no phase compensation pulse, midway between the optimal phase compensation for either array. The bottom shows that images are obtained from both arrays in one echo using the fourth gradient to provide a slice dependent phase compensation of ±8 rad/cm over a 1 cm slab [51]. (© 2012 IEEE)

4.3.3. Effect of Through-slice Gradient

As shown in Section 3.5, the through-slice gradient causes signal cancellation toward the edges of the imaging field of view along the x direction. In order to assess the effect of this cancellation in SEA imaging, the normalized average signal level over a uniform region of the phantom is extracted from projections from each channel for increasing fourth gradient values. For each fourth gradient value, the phase compensation gradient or *k*-space line yielding maximum signal was selected. This metric is termed "available signal". Because the array coil elements are positioned along the x-direction, channel number correlates with position along x. The bottom half of the sandwich array coil is connected to receiver channels 1-32, while the top half is connected to channels 33-64. Channel 1 is at the edge of the field of view of the bottom array (at approximately x = -3.2 cm), while channel 16 is near the center (at x = 0 cm). Fig. 49. shows that the available signal decreases with distance from the center of the field of view as the fourth gradient value is increased. For the fourth gradient value used in Section 4.3.1, ±12 rad/cm over a 1 cm slab, approximately half of the signal is lost at the edge of the field of view. In Section 4.3.2 a value of ±8 rad/cm was employed, resulting in signal loss of approximately 25%. However, due to the channel to channel normalization employed in the SEA images presented, this loss was not noticeable. With the normalization method employed, additional artifacts may occur if there are thin features (in the y direction) near the edges, as these will be less affected by the through slice gradient, resulting in unwanted brightening upon normalization. This may be improved by other normalization strategies.

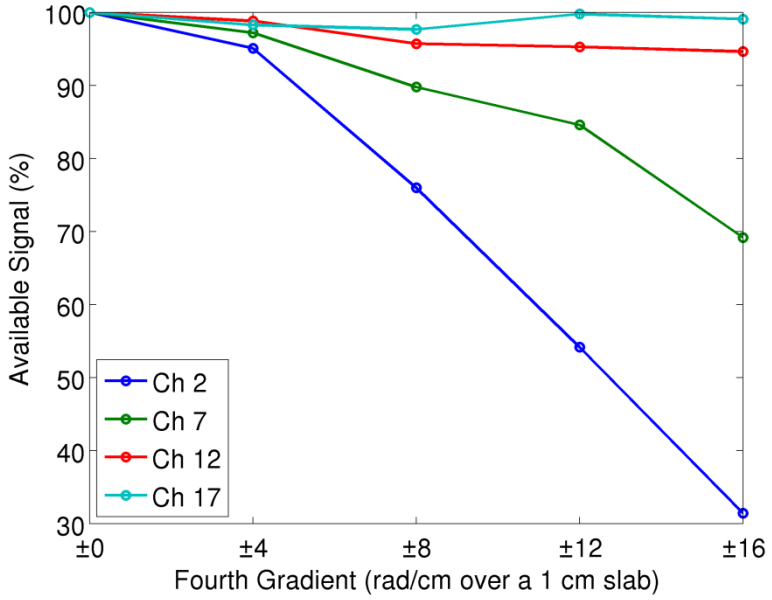

Fig. 49. Loss of SEA signal due to the through-slice gradient at the bottom array. As the fourth gradient value is increased, the peak received signal resulting from an optimal phase compensation pulse decreases for channels nearest the edges of the field of view. Channel 2 is near the edge of the field of view where signal loss is greatest, while Channel 17 is near the center of the field of view where no signal loss occurs. This loss is not visible in the SEA image reconstructions shown above due to normalization across channels.

4.4 Highly Accelerated 2D Imaging Results

Some of the resolution sacrificed to obtain images in a single echo can be recovered by what has been termed “resolution enhanced” imaging [54]. While the data for such images is acquired in two or more echoes, the images could be refreshed as new data becomes available, with each echo providing new spatio-temporal information. In past implementations one echo is acquired near the peak of *k*-space, providing the bulk of the signal, and one to three additional echoes offset from the peak of *k*-space are then acquired, supplying additional higher spatial frequency components of the image. The reconstruction is performed by placing the acquired phase encode lines in a zero matrix of dimensions equal to the *k*-space of the fully encoded image. After a Fourier transform, a significantly aliased image is obtained from each coil. These images are windowed by the known coil element positions and combined by sum of squares. The lines of *k*-space providing additional resolution can be selected based on which spatial frequencies are desired. For instance, if acquiring highly accelerated MR elastography data, it may be desirable to acquire specific spatial frequencies to capture a propagating shear wave [85]. When imaging with a sandwich array, the phase encoding gradient values correspond to different spatial frequencies when received by each half of the array. Using the fourth gradient channel for phase compensation allows collection of resolution enhanced images with greater efficiency, such that at the same time an echo providing peak signal is acquired by the bottom array, an echo providing the desired additional spatial information is acquired by the top array.

A metric to quantify the quality of such highly accelerated images is artifact power (AP), given by

$$AP = \frac{\sum_{m=1}^{M_{col}} \sum_{n=1}^{N_{row}} \left(I(m,n) - I_{ref}(m,n) \right)^2}{\sum_{m=1}^{M_{col}} \sum_{n=1}^{N_{row}} I_{ref}^2(m,n)}$$

where $I(m,n)$ and $I_{ref}(m,n)$ are the intensities of the accelerated and fully encoded reference images at pixel (m,n). This was originally reported as a method to quantify image quality in partial Fourier reconstructions [86] and has been used previously by our group to assess resolution enhanced imaging performance [54]. In using this metric to compare highly accelerated images with the 64 channel array to fully encoded images, it was necessary to first normalize the image power, as including fewer *k*-lines in the reconstruction results in lower average image intensity.

To demonstrate the effect of the fourth gradient on resolution enhancement, several images were reconstructed retrospectively from the dual-slice dataset using 2 *k*-lines, one of which is the *k*-line corresponding to peak signal in the signal vs *k*-line plots, and the other of which provides additional resolution. Artifact power was calculated as a function of the additional "resolution enhancing" *k*-line, using the fully encoded image as the reference. Using the bottom array for receive, line 142 provides peak signal, so artifact power was calculated for lines in addition to 142. The plot in Fig. 50 shows that also including line 162 gives minimum artifact power. The resulting signal vs. *k*-line plot and reconstructed images are shown in Fig. 51. While using these lines yields resolution enhanced images from the bottom array, only high spatial frequency components of the image are received by the top array, as the coil's RF phase gradient is opposite,

sensitizing it to different spatial frequencies. For the top array, line 115 gives peak signal and minimum artifact power is achieved by also including line 96 in the reconstruction, as shown in Figs. 52 and 53.

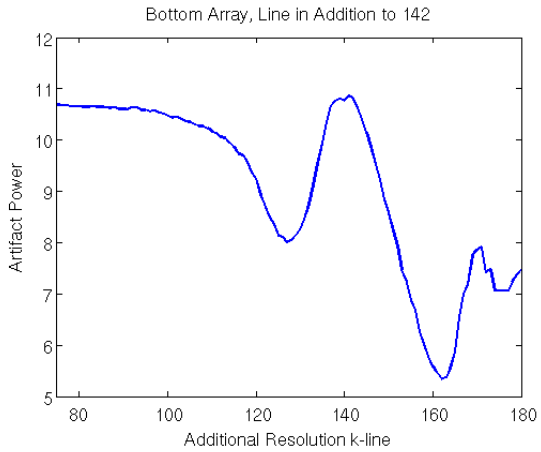

Fig. 50. Artifact power of the image received by the bottom array. Plotted as a function of the second *k*-line included for additional resolution. Including line 162 along with the peak signal line of 142 yields a minimum artifact power of 5.34.

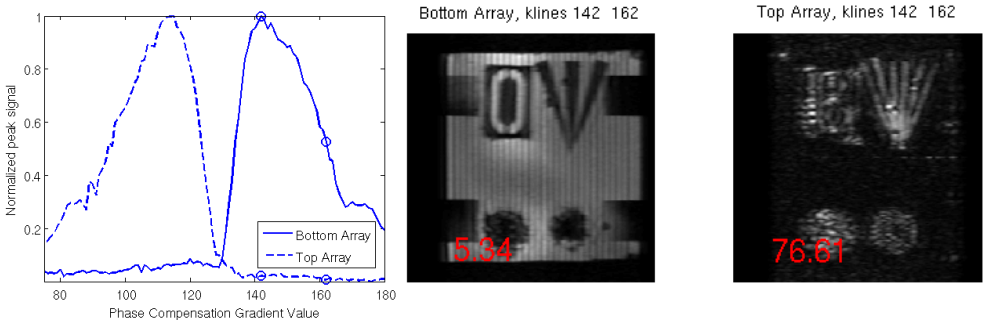

Fig. 51. Signal vs *k*-line plot and partial-Fourier reconstruction for minimum artifact power from the bottom array. *k*-lines 142 and 162 were used. These *k*-lines yield only high spatial frequencies from the top array.

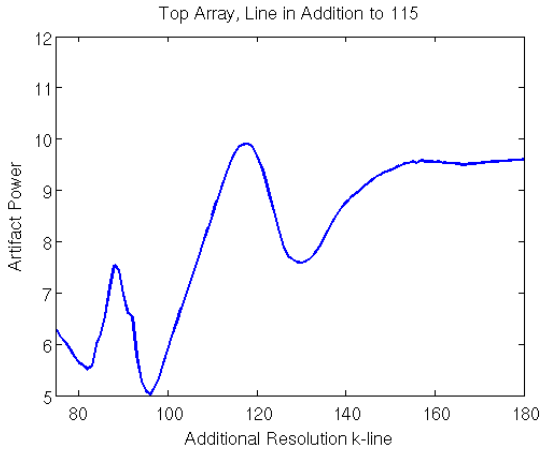

Fig. 52. Artifact power of the image received by the top array. Plotted as a function of the second *k*-line included for additional resolution. Including line 96 along with the peak signal line of 115 yields a minimum artifact power of 5.02.

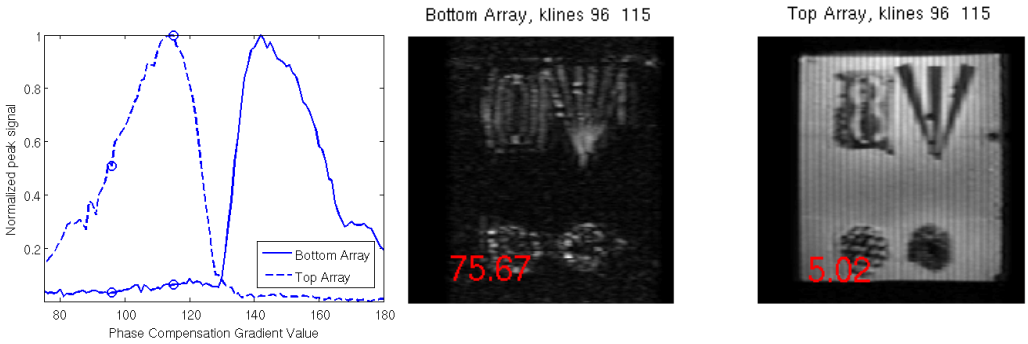

Fig. 53. Signal vs *k*-line plot and partial-Fourier reconstruction for minimum artifact power from the top array. *k*-lines 96 and 115 were used. These *k*-lines yield only high spatial frequencies from the bottom array.

In the dual slice excitation, when receiving from the top and bottom arrays simultaneously, the combined artifact power can be used as a metric for optimal image quality. This is computed by taking the square root of the sum of the squares of the artifact powers from each array. The combined artifact power can be plotted as a function of the distance between the two acquired *k*-lines, with lines equally spaced from the center of the acquired *k*-space, yielding the same spatial frequency components from each array. Without using the fourth gradient coil, the optimum occurs using lines 109 and 149, yielding signal from each array as shown in Fig. 54. However, because of the distance between the *k*-space peaks, the line giving signal from the opposite array results in sub-optimal resolution enhancement, as shown in Fig. 55. While the combined artifact power from the optimal images from each array shown above is 7.33, the artifact power from the simultaneously received images is 12.02.

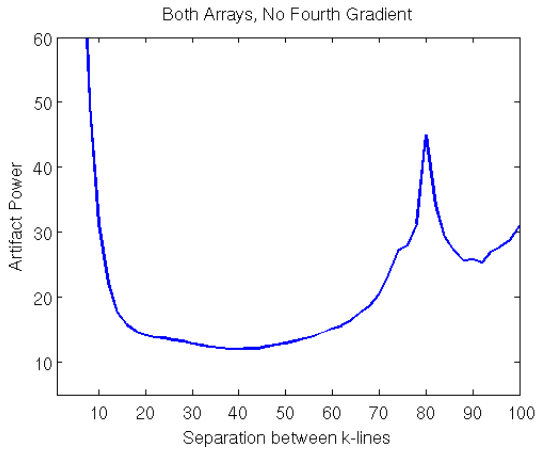

Fig. 54. Combined artifact power from both arrays without the fourth gradient coil. *k*-lines employed are equally spaced from center of the acquired *k*-space (*k*-line 129). A separation of 40 *k*-lines yields the lowest combined artifact power of 12.02.

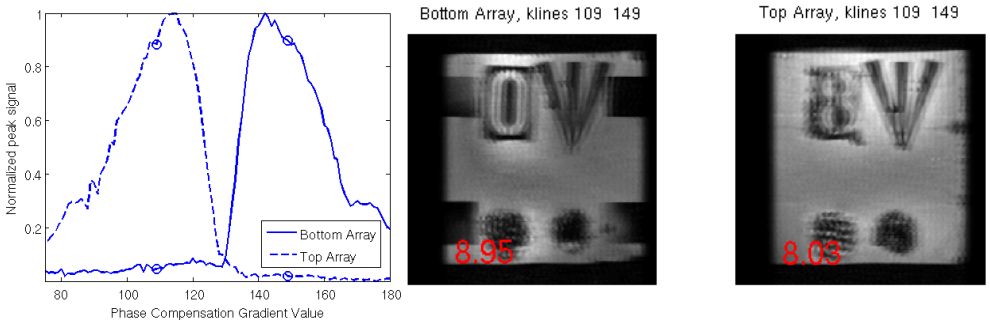

Fig. 55. Signal vs *k*-line plot and partial-Fourier reconstruction for minimum combined artifact power from the both arrays without the fourth gradient coil. *k*-lines 109 and 149 were used. These *k*-lines yield images from both arrays, but with greater distortion than the images produced with *k*-line selection optimized for either one of the arrays.

However, when applying the fourth gradient the *k*-space peaks are moved together, such that when acquiring the peak signal line from one array, resolution-enhancing information is simultaneously received from the opposite array. A minimum combined artifact power of 9.80 is achieved using the fourth gradient coil and *k*-lines 117 and 137, shown in Fig. 56. This power is still greater than that achieved by the optimal images acquired from either array individually as new artifacts are introduced by the fourth gradient. Qualitatively however, the images obtained using the fourth gradient, shown in Fig. 57, exhibit significantly improved resolution compared to those in Fig. 55. This is especially notable in the amount of blurring and in comparison with the images reconstructed from lines selected for optimal images from either array.

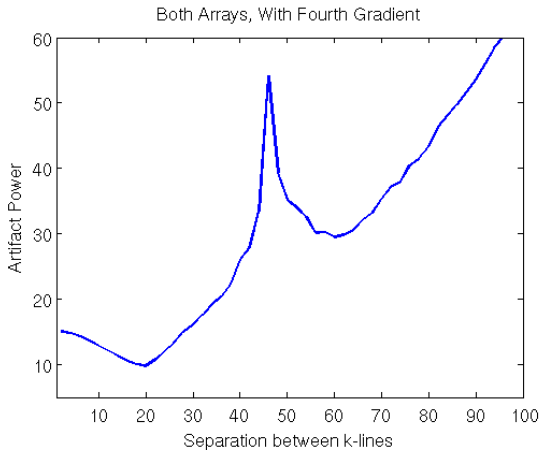

Fig. 56. Combined artifact power from both arrays with the fourth gradient coil. The coil was configured to produce +/- 12 rad/cm over a 1 cm slab. Two *k*-lines equally spaced from center of the acquired *k*-space (*k*-line 127 – due to an offset in the fourth gradient field) were used. A separation of 20 *k*-lines yields the lowest combined artifact power of 9.80.

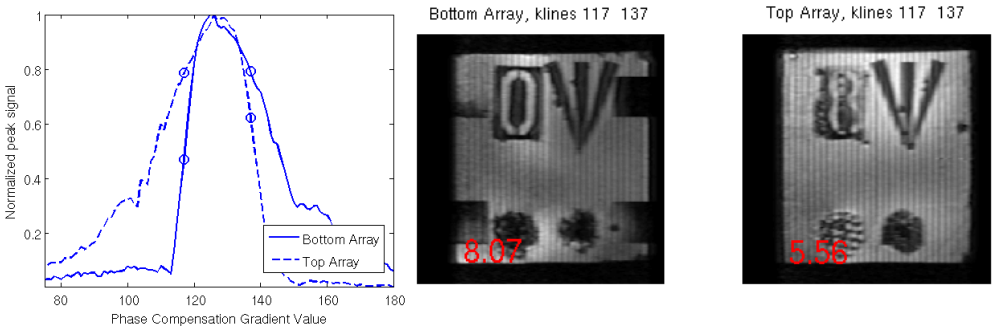

Fig. 57. Signal vs *k*-line plot and partial-Fourier reconstruction for minimum combined artifact power from the both arrays with the fourth gradient. *k*-lines 117 and 137 were used. These *k*-lines yield images with improved resolution from both arrays.

As the fourth gradient strength is increased, the artifacts induced by the unwanted through-slice gradient begin to exceed the artifact power improvement due to correcting the RF coil phase gradient. Fig. 58 shows that beyond a fourth gradient pulse producing ±16 rad/cm over a 1 cm slab, the artifact power is worse than without the fourth gradient. It is also important to note that lowest artifact power does not always correspond to the most visually appealing image, but serves as a general metric. There may be cases in which application of a rather strong fourth gradient pulse is desirable, sensitizing the image to a particular target resolution, despite increased artifact power. Also, a fourth gradient producing ±12 rad/cm over a 1 cm slab was selected, while the result in Fig. 58 indicate that lowest artifact power occurs for a setting of ±8 rad/cm over a 1 cm slab. The stronger gradient yielded better images from both arrays.

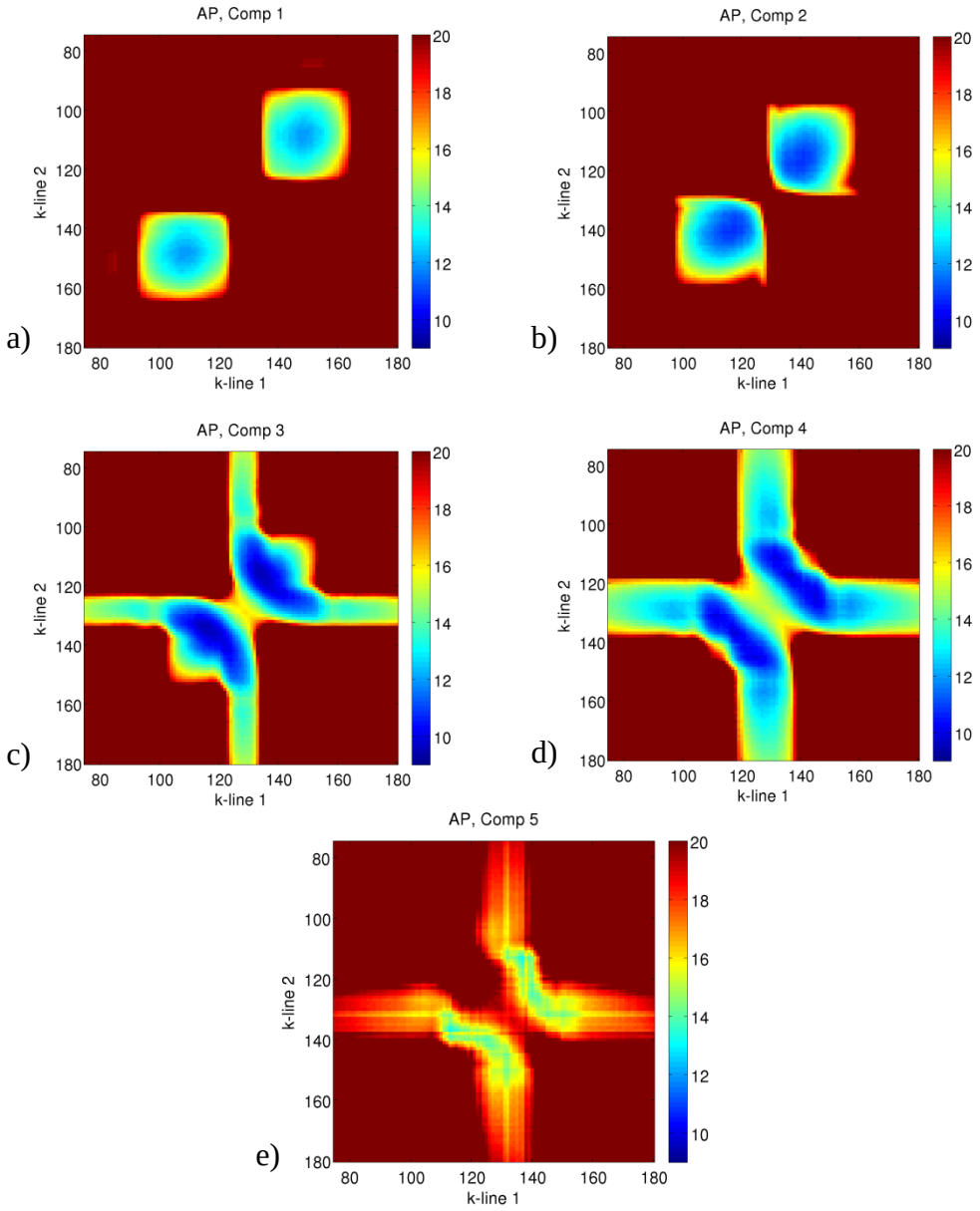

Fig. 58. Dual-slice combined artifact power of 2 *k*-line image from both arrays. Blue indicates low artifact power and red indicate high artifact power for each possible pair of *k*-lines used in a resolution enhanced reconstruction. The forth gradient strength is varied across a) ±0 rad/cm, b) ±4 rad/cm, c) ±8 rad/cm, d) ±12 rad/cm, e) ±16 rad/cm, each over a 1 cm thick slab. At ±16 rad/cm, the image quality begins to degrade due to artifacts caused by the through-slice gradient.

4.5 3D Imaging Results

The described imaging system allows both high resolution and highly accelerated imaging with no changes to the hardware configuration. Using a 3D acquisition sequence with two phase encode axes, the dual sided array has been used to acquire a high resolution MR microscopy dataset over the whole volume of a sample. The images were reconstructed using a technique similar to PILS [40] in which the image from each coil element is windowed and offset based on the position of the coil within the full field of view of the image and then combined by sum of squares. Images were obtained using 1024 frequency encode points in z by 128 phase encode steps in x and 128 phase encode steps in y, yielding a resolution of 78 µm x 63 µm x 125 µm, as shown in Fig. 59. The SNR benefit of the small array elements enables imaging at this high resolution essentially at the array surfaces, with the images decaying to noise deeper into the sample as the RF coil field patterns fall off. However, the high resolution dataset can be parsed to lower resolutions, providing images deeper within the sample as shown in Fig. 60.

Most notable is the amount of time saved by using this technique. With a 1 s repetition time, acquisition of this volumetric image using the 64 channel array required 4.6 hours. However, to obtain an image of the same resolution using a single volume coil for receive would require extending the field of view in the x direction by a factor of 10, requiring 10 times as many phase encode steps and a factor of 10 more time. In addition, without the SNR benefit at the array surfaces afforded by using small coils, averaging becomes necessary, further increasing acquisition time.

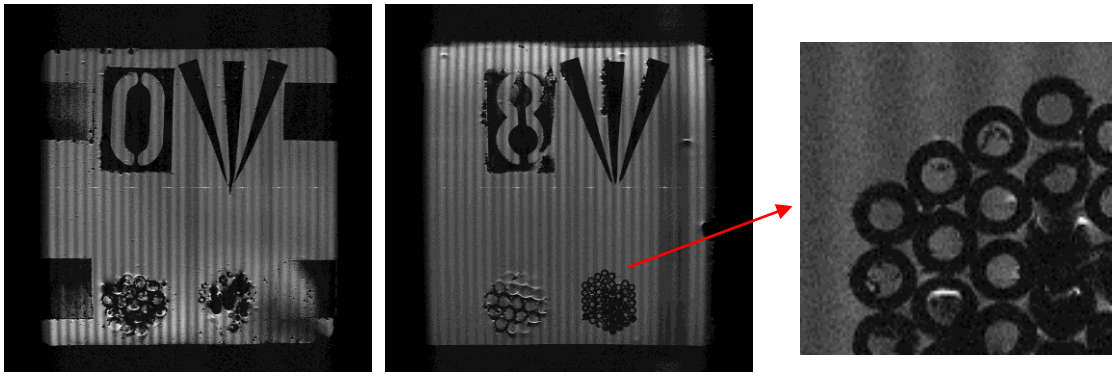

Fig. 59. Microscopy images obtained at the surfaces of the sandwich array. Image from the bottom array (left) and top array (middle) from a 3D dataset acquired at a resolution of 78 x 63 x 125 μm over a 6.4 x 6.4 cm field of view. The zoomed-in region in the rightmost image shows a bundle of 1.65 mm OD capillary tubes.

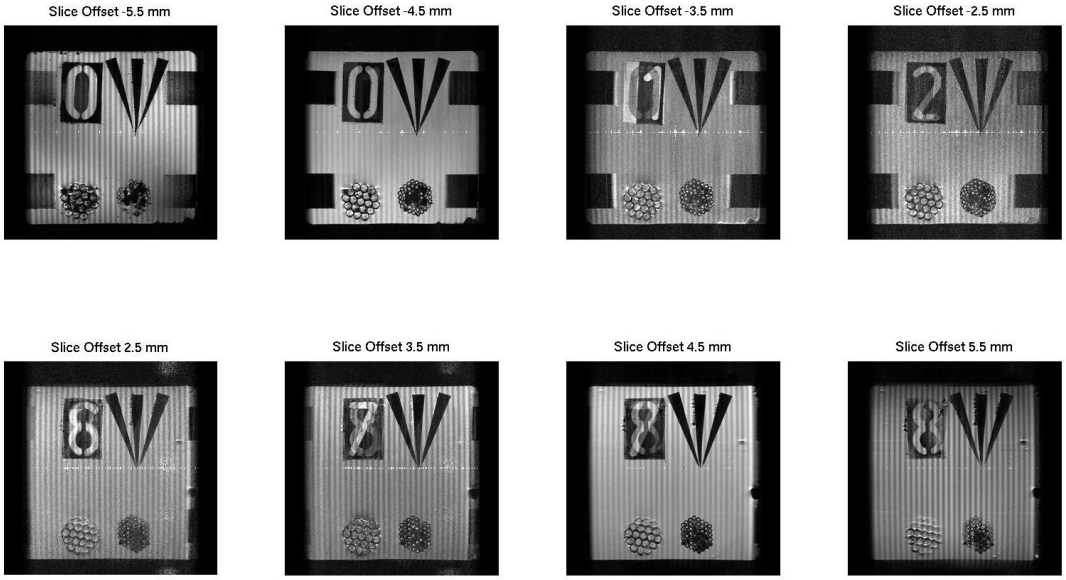

Fig. 60. Reduced resolution (313 x 250 x 1000 μm) images extracted from the same high resolution dataset above. Highest resolution is available at the array surfaces where the sensitivity of the coils is strongest. SNR at slices further from the array is recovered by extracting lower resolution images from the full resolution dataset. Images up to a distance of 3 mm from either array are shown.

If the field of view along the x direction (narrow dimension of coil elements) is high enough such that *k*-space is significantly oversampled, images can be recovered through the entire thickness of the sample, as shown in Fig. 61. Additionally, lower resolution, highly accelerated 3D imaging is possible using the fourth gradient coil. Because 3D imaging replaces slice selection with phase encoding, it is not possible to program the phase compensation gradient to vary for each slice. Using the fourth gradient coil allows compensating for the phase of a sandwich receive array over the entire volume of a sample simultaneously. A 3D dataset was acquired using a 500 ms TR, 30 ms TE, 256 readout points along z, 256 phase encode steps along x, and 64 phase encode steps along y, field of views of 80 mm along z, 80 mm along x, and 16 mm along y, and a 50 kHz spectral width. Non-selective square RF pulses of 500 μs duration were employed. Because of the larger data size, separate data sets were acquired for different fourth gradient values, using a 7 ms half-sine pulse producing 0, ±8, ±12, ±16, and ±20 rad/cm over a 1 cm slab.

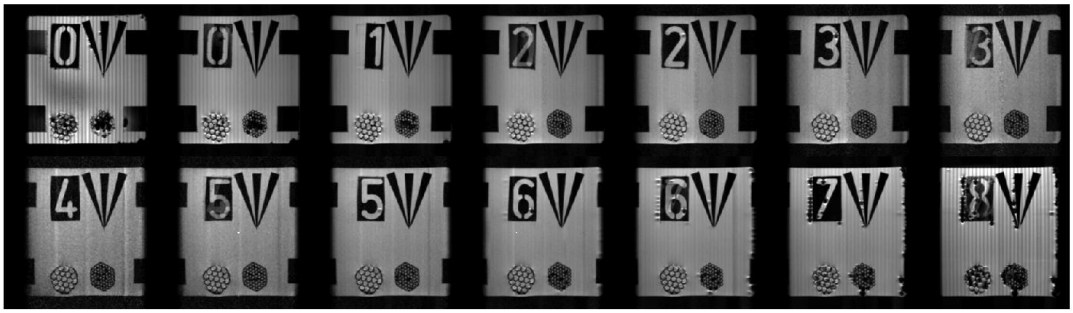

Fig. 61. Set of 3D images over entire volume. Slices from a 3D dataset were acquired with a sandwich array at a resolution of 312.5 x 250 x 312.5 μm over a 6.4 x 6.4 cm region. Using a lower resolution and field of view significantly beyond the sensitive region of each coil element in x, effectively averaging the noise by oversampling *k*-space, yields images through the entire slab which was not possible using a single sided

By extracting a single *k*-line along the x direction, 2D-SEA images are obtained from each coil. By stacking these images, a 3D-SEA volume image is obtained [52, 53], with the width of each coil element providing the resolution along x. However, the coil phase gradient shifts which single x *k*-line is necessary to obtain the SEA image sets from the bottom and top arrays. By applying a pulse of the fourth gradient, the same x *k*-line gives images from both arrays, enabling 3D-SEA imaging as shown in Fig. 62.

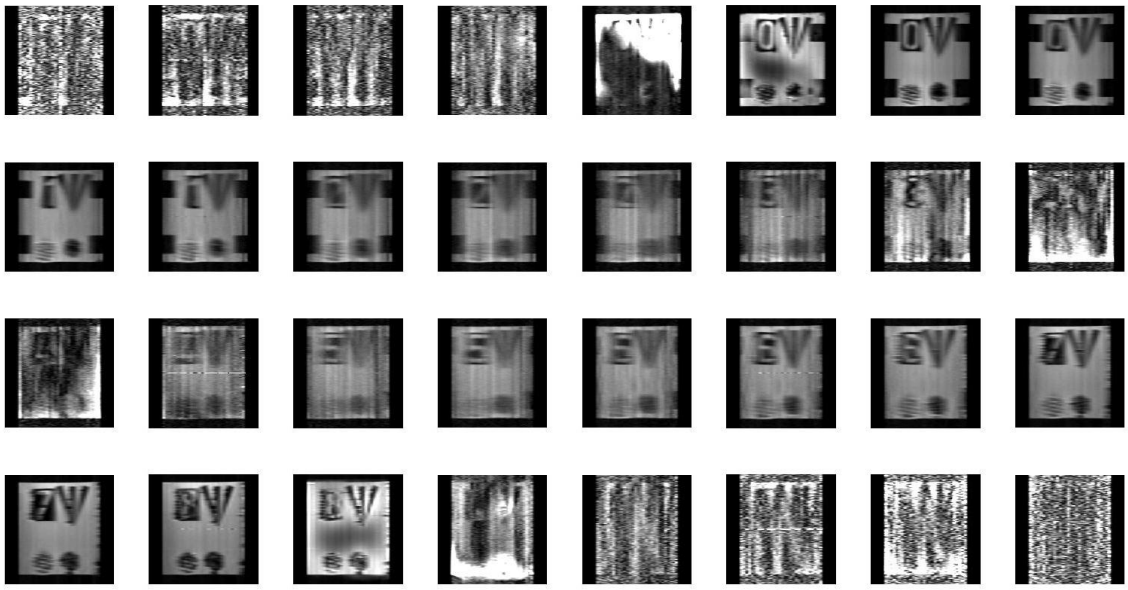

Fig. 62. "3D-SEA" images with the fourth gradient. A single x *k*-space line is acquired, along with 64 y phase encode steps and 256 readout points. Using the fourth gradient to provide ± 12 rad/cm over a 1 cm slab, images are simultaneously obtained from the bottom array (first two rows) and the top array (last two rows). Without the fourth gradient, 3D-SEA images can be acquired from only one array at a time.

Partial Fourier reconstructions in highly accelerated 3D imaging can also be performed, in which two or more lines of *k*-space along the x direction are acquired to provide additional resolution. As with the dual-slice excitation, employing the fourth gradient coil allows more efficient acquisition of the desired spatial frequency components of the image, such that at each echo useful information is received from both arrays. Fig. 63 shows an example set of images acquired of using two *k*-lines separated by 20 lines with the fourth gradient set to generate a phase variation of ±12 rad/cm over a 1 cm slab, which was shown to provide the lowest combined artifact power at the bottom and top slices in the dual slice experiment above. Using *k*-lines 118 and 138, resolution enhanced images are obtained near the periphery of the sample. However slices closer to the middle of the sample, where the RF coil phase gradient is less, do not receive the proper phase compensation and return poor images. By also including *k*-lines 125 and 131 in the reconstructions as shown in Fig. 64, images near the center of the sample are restored as these slices also receive the proper compensation. However resolution varies with slice as the RF coils remain sensitive to different spatial frequencies at different distances.

Fig. 63. Resolution enhanced 3D reconstruction using two *k*-lines. The *k*-lines are separated by the same distance yielding minimal artifact power in the dual slice experiment above (lines 118 and 138) with the fourth gradient producing a variation of ± 12 rad/cm over a 1 cm slab. While these lines yield resolution enhanced images from the outer slices, the middle slices yield little signal, as they require lower phase compensation values.

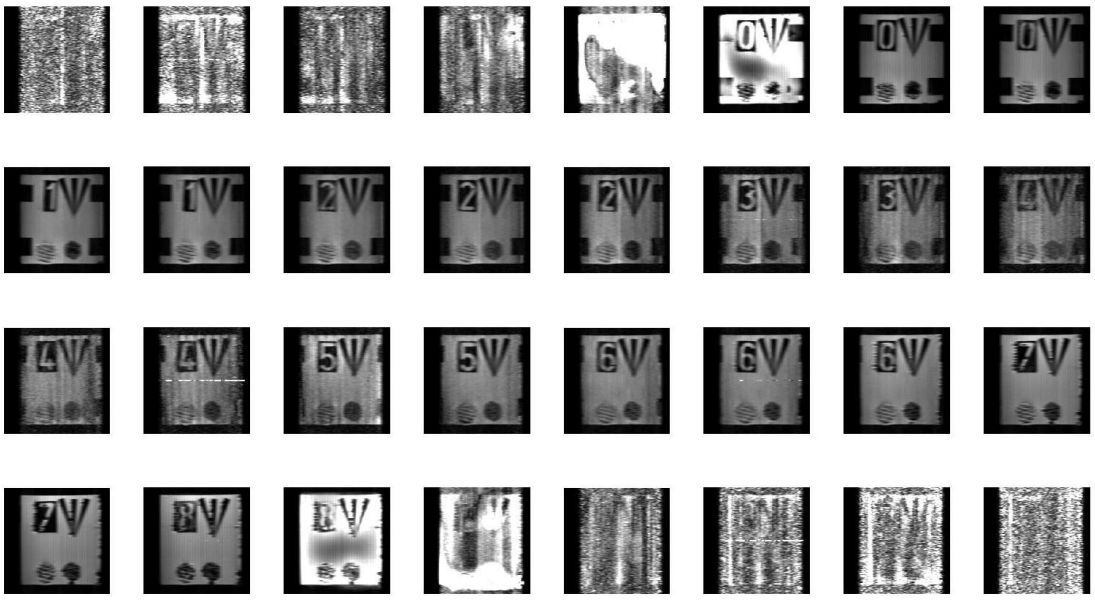

Fig. 64. Resolution enhanced reconstruction using four *k*-lines. *k*-line 118, 125, 131, and 138 were used with the fourth gradient producing a variation of ± 12 rad/cm over a 1cm slab. Using four lines allows resolution enhancement at the outer slices while also providing suitable phase compensation to recover images from the middle slices.

The need for maintaining a fairly high resolution in y to avoid problems due to the offset in y *k*-space when imaging with the fourth gradient are shown in Fig. 65. Similar to the volume coil 3D image shown earlier, decreasing from 64 to 32 y *k*-lines leads to signal loss at the edges, as the center of *k*-space is no longer sampled in these regions. The additional striping artifacts are likely due to a combination of the slice-varying x phase gradient and truncation artifacts in the inverse Fourier transform, or other system instabilities.

Fig. 65. Artifacts in 3D imaging with the fourth gradient due insufficient coverage of y *k*-space. Resolution enhanced reconstruction using the same fourth x *k*-lines above, with the fourth gradient producing a variation of ±12 rad/cm over a 1 cm slab but retaining only 32 of the 64 *k*-line collected. Loss of field of view along x is apparent.

5. APPLICATIONS

5.1 Spatio-temporal Capabilities

The wide field of view imaging probe finds its greatest utility in applications demanding both extremely fast and high resolution MR imaging. The probe allows conveniently switching between these modes of operation by adjusting the imaging parameters and fourth gradient setting with no changes to the hardware configuration. At the extremely fast end is SEA, in which an MR image is received in a single echo. The probe extends the SEA technique in the third dimension by employing two arrays receiving simultaneously with opposite coil phase compensation provided by the fourth gradient coil. This is most important in the dual-slice imaging described above, allowing rapid imaging at both the top and bottom surfaces of a sample. Several applications may benefit from real time MR imaging of the periphery of a sample.

One potential application is imaging of fluid flow. Magnetic resonance has been used to study flow for a number of years, especially in vivo blood flow. A review article on flow in NMR lists several of the advantages of NMR for imaging flow, including its non-invasiveness, ability to measure many parameters, and that it is not adversely affected by optical opaqueness which is especially an issue in multi-phase flows [1]. It has also been used in measurement of flow in engineering and for velocity measurement of turbulent flows and diffusion [2]. Investigators have developed fast imaging sequences to capture flow phenomenon with the desire to capture turbulent flow [87]. SEA imaging provides the ability to visualize non-repeatable events like turbulent flow

in a way unlike other parallel imaging strategies which eliminate only a fraction of the phase encoding [26, 27]. Because SEA imaging eliminates phase encoding completely, each RF excitation and resulting echo capture a frame of such dynamic events, with the frame rate determined by the TR of the pulse sequence. Another potential application of this probe which is discussed in detail below is MR elastography [88], a phase contrast imaging method that captures vibrations in elastic media.

At the other side of the spatio-temporal range of this system is wide field of view MR microscopy, which is extended further in the third dimension using the described wide field of view probe. Because of the extent of *k*-space sampled in high resolution imaging, the RF coil phase generally does not adversely affect the acquired images, so coil phase compensation is unnecessary and the fourth gradient is disabled. Several of the intended applications of wide field of view microscopy with a single sided 64 channel array have been excised brain slices, study of bone and cartilage architecture, skin, and neuritic plaques [8]. Applications of particular interest are those demanding both high speed and high resolution over a large field of view. A potential application discussed in detail below is microscopic magnetic resonance elastography (μMRE) [89].

5.2 MR Elastography

5.2.1 Background

MR elastography (MRE) is a method of imaging mechanical vibrations propagating through an elastic material such as tissue [88, 90]. By applying mechanical vibrations to a sample in the presence of an oscillating motion sensitizing gradient of the same frequency, micrometer displacements induce a change in the phase of the acquired

MR images. The resulting "wave images" allow extraction of the wavelength of the mechanical vibration at different positions, allowing estimation of a map of the elastic modulus. In the clinical setting, this has been used to measure the stiffness of the liver to assess liver fibrosis [91]. Other applications include MRE of the brain [92], muscle [93], and breast [94].

Typically four to eight "phases" of the wave image are captured in order to extract the elastic modulus [95]. Acquisition of each phase requires acquisition of a complete image with the phase between the motion sensitizing gradient and the vibration source shifted. As this can be a time consuming process, groups have attempted to improve acquisition time using gradient echo [96] and EPI [97] sequences. Spatially selective MRE has also been investigated as a means of reducing the acquisition time [98]. By using a spatially selective RF excitation, the elasticity of a specific region or anatomy can be determined. Because fewer *k*-space steps are necessary to image a limited field of view, faster imaging is possible. Similarly, parallel MRI has been shown to accelerate data acquisition in MRE [99]. A different approach to save time in MRE is to alter the sampling strategy. Because the spatial frequency content within the sample with the encoded elasticity information is limited in some situations, acquisition of the complete *k*-space may not be necessary to obtain accurate elasticity measurements [85].

Another technique called "mechanical transient" based MR elastography seeks to determine elasticity by observing a mechanical disturbance as it propagates through a sample [100]. Stiffer regions will accelerate the propagating wave front while slower regions will slow it down. Generating a map of the tissue elasticity from this data

demands acquisition of many frames of the propagating wave to determine the regions in the sample where its propagation velocity changes. Reported results used sixty-four temporal offsets, requiring a much more time consuming scan than the typical "dynamic" elastography described above.

Another challenge in MR elastography is the longer echo times required to accommodate the motion sensitizing gradient pulse, which is usually one or more periods at the same frequency as the applied mechanical vibration. For vibrations on the order of 100 Hz, this results in an echo time of sufficient duration to accommodate at least a 10 ms motion encoding gradient pulse, which causes problems for samples with a short T2 relaxation time. Various strategies have been employed to reduce this time, including "fractional encoding" which employs a motion sensitizing gradient at a multiple of the frequency of the applied vibration [101] or methods employing gradients sensitive to a broad range of vibration frequencies [102]. For MRE of the heart, a sequence called DENSE has been employed to improve the sensitivity compared to the fractional encoding sequence [103].

While MRE captures transverse shear waves which have wavelengths on the order of tissue dimensions, some clinical implementations of liver MR elastography employ a longitudinal driver and rely on mode conversion to generate transverse shear waves in the liver [104]. Mode conversion has also been utilized to create high frequency transverse shear waves deeper within a sample or patient [105]. Because longitudinal waves attenuate more slowly in tissue, mode conversion allows detection of stiff regions by detecting the presence of high frequency shear waves beyond the

distance at which high frequency transverse shear waves from the source have attenuated. When imaging stiff samples such at cartilage, the wavelength within the tissue is longer, requiring the use of high frequency shear waves. Applied vibrations of up to 9 kHz have been used in MR elastography of cartilage samples [106].

Another area of interest is microscopic MRE or μMRE [89]. Because of the small regions of interest and because at least a half wavelength of the vibration wave field must be captured to reliably extract tissue elasticity [107], investigators have employed frequency vibrations of approximately 550 Hz. The typical spatial resolutions used in μMRE were 34 μm x 34 μm to 140 μm x 140 μm with a 500 μm slice thickness. Elasticity measurements were conducted of phantoms, frog oocytes, and tissue-engineered constructs. One of the limitations in the μMRE method to date is that the high frequency mechanical vibration attenuates rapidly, limiting the measurement depth [108]. The limitation in the resolution of stiffness measurements due to the low mechanical driving frequencies and consequent low spatial frequencies of the shear waves is also discussed in a paper on tissue engineered constructs. The authors suggested in some cases using frequencies greater than 2 kHz [109]. Microscopic MRE has also been applied in traumatic brain injury models using rat brains [110].

SEA imaging using a single array has previously been employed by our group both for dynamic elastography as described and mechanical transient based elastography [28, 29]. SEA imaging provides the advantage of yielding a frame or “phase” of an elastography “wave image” set upon each echo. In addition to improving upon the time requirements for obtaining a set of wave images, SEA elastography may be especially

valuable in testing of non-repeatable or dynamic events. One example is a study of muscle stiffness under variable applied strain [111]. SEA MRE may allow extending this study to destruction and tearing of tissue samples. A reported investigation that could benefit from SEA is MRE of the sol/gel transition of agarose [112], which our group has explored previously [29]. Similarly, MRE during thermal ablation [113] may benefit from rapid, single shot imaging. Another possible application is in wide dynamic range elastography, in which a range of mechanical excitation frequencies are captured to assess tissue mechanical properties [114].

5.2.2 Initial Results

In order to explore potential MR elastography studies which may benefit from a wide spatio-temporal imaging range, some initial experiments were conducted using the imaging probe. A longitudinal mechanical driver system similar to that described by Yin et al. [91] was employed in these tests. This mechanical excitation method has previously been employed by our group for SEA imaging, with some results shown at the 2007 ISMRM conference in Berlin [115] and in the Proceedings of the IEEE EMBS [116]. The setup consists of a triggered function generator connected to an audio amplifier and speaker. Upon receipt of a trigger from the imaging system, the function generator produces 40 cycles of an audio frequency sine wave at 400 Hz which is guided into the RF shield room by a plastic tube adapted to the speaker. The tube terminates at an aperture in an agarose gel phantom, as shown in Fig. 66.

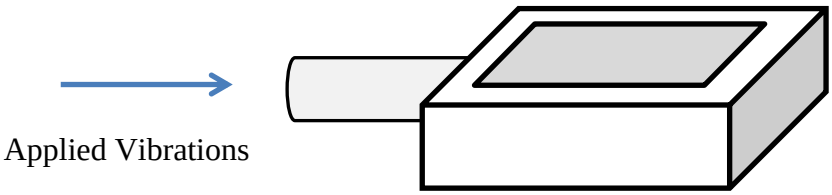

Fig. 66. Test phantom for MR elastography. A tube is connected to the side channel, conducting the vibrations into an agarose gel phantom.

Three imaging protocols were investigated using a phantom consisting of approximately 1% agarose gel with an occlusion near the vibration aperture consisting of half agarose concentration. Applied mechanical waves are expected to decelerate and exhibit a shorter spatial wavelength within the occlusion. A 1 g/L copper sulfate solution was used in preparation of the agarose gels, reducing the T1 relaxation time. In the first protocol, a spin echo pulse sequence was modified for dual-slice SEA imaging using the sandwich receive array and fourth gradient coil for phase compensation. A modified sinc pulse was designed to excite two 0.75 mm thick slices separated by 7.5 mm. In addition, a 400 Hz bipolar motion sensitizing gradient pulse was inserted on the x gradient axis for MR elastography. The delay between the each mechanical vibration pulse and the motion sensitizing gradient pulse was increased upon repeated excitations and acquisitions, with each acquisition yielding one frame of the vibration propagating into and across the sample. This allows capture of an emerging mechanical wave at the lower and upper boundaries of a sample in a time equal to TR times the number of acquired frames. Two hundred forty time steps were acquired with a step size of 0.125 ms. Such

acceleration of the acquisition of many frames of a propagating wave could be beneficial in mechanical-transient based elastography.

A TR of 1 s and a TE of 30 ms were employed. The field of view of the displayed images is 80 x 80 mm with the receive array covering the central 64 x 64 mm. Two hundred fifty-six frequency encode points were acquired with no phase encoding. The fourth gradient was set to produce ±0.8 rad/cm over a 1 cm slab by a 5 ms half-sine pulse for RF coil phase compensation. Elastography phase contrast "wave images" resulting from this acquisition are shown in Fig. 67. These were obtained by division of the complex image frames by a single reference image taken with the vibration source disabled to cancel all background phase. The bottom array images depict the wavelength shortening in the occlusion region, highlighted in Fig. 68. The gel in the occlusion region and that surrounding it receded somewhat in the top slice, likely due to drying. The wave fields in the top and bottom slices are different due to their positions on opposite sides of the excitation aperture and due to different boundary conditions. The gel in the bottom slice is bound by the acrylic sample holder, while at the top slice there is an air gap between the gel and the top acrylic plate.

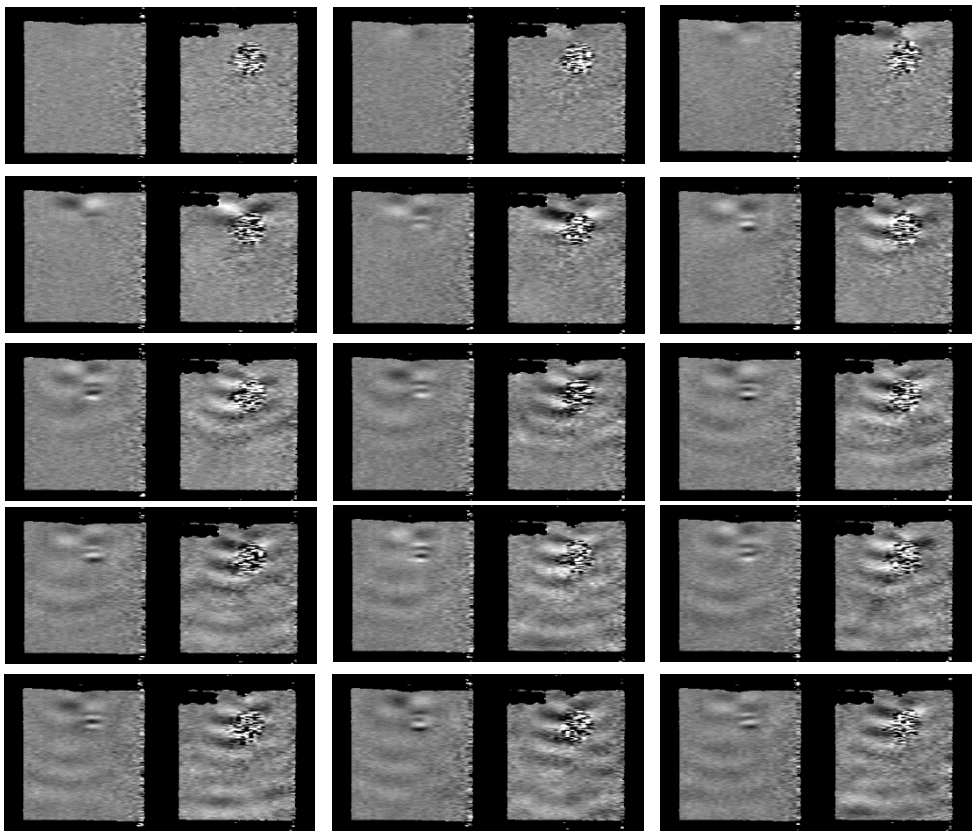

Fig. 67. SEA MR elastography "wave images" of an emerging 400 Hz mechanical disturbance. The vibrations are applied in the top center of the phantom as shown. Every sixteenth frame, representing a time step of 2 ms, of a 240 frame set is shown. The left hand image within each frame was acquired by the bottom array while the right hand image was simultaneously acquired by the top array. The set of 240 frames was acquired by repeating the mechanical vibration for each excitation and acquisition with the delay between the vibration and motion sensitizing gradient increased by 0.125 ms.

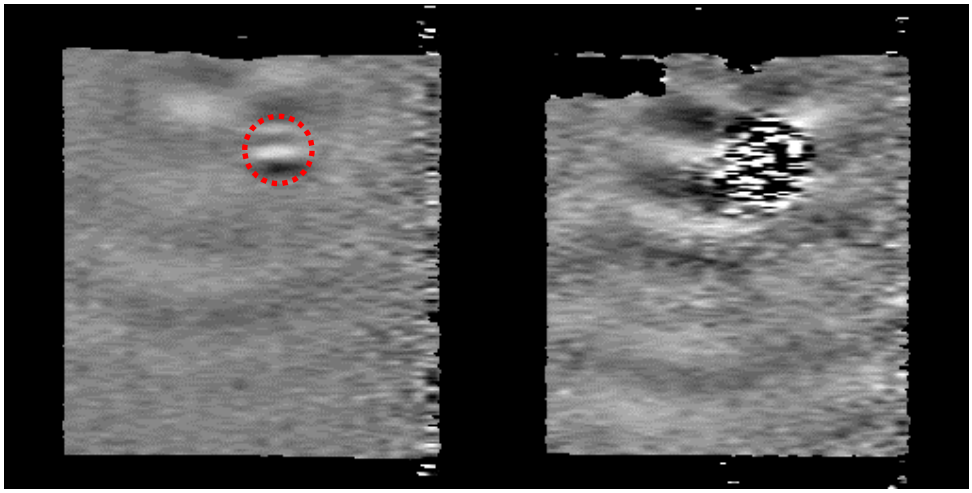

Fig. 68. Soft gel occlusion. The spatial wavelength is shorter in the highlighted soft gel occlusion, which has approximately half the agarose concentration as the background gel.

In the second protocol, the acquisition is further accelerated by recalling four gradient echoes following a single RF excitation and mechanical vibration pulse, incorporating a bipolar motion sensitizing gradient pulse prior to each readout gradient pulse as shown in Fig. 69. The same two slices were excited. A single fourth gradient pulse of -/+ 0.8 rad/cm over a 1 cm slab provided RF coil phase compensation for the sandwich array. Each recalled echo yields a SEA image with additional phase contrast added as a single mechanical vibration propagates across the sample. This may be useful in time sensitive or dynamic experiments which will not allow repetition of an applied mechanical transient. The scan was repeated with the vibration source disable to acquire four recalled reference phase images to cancel background phase. While the digitizer cards in the 64 channel receiver are capable of a higher temporal frame rate, in these preliminary results an echo was recalled every 6 ms due to limitations in the acquisition

software. This frame rate could be improved using other acquisition strategies. Because of the long echo time, significant artifacts appear in the wave images, shown in Figs. 70 and 71. In Fig. 70, the phase contrast accumulates image to image, such that the fourth elastography "wave image" is the sum of the vibration fields encoded by all four motion sensitizing gradient pulses. A simple subtraction was applied to yield the images in Fig. 71, intended to isolate the vibration field at each time. While the dynamics of the propagating wave are not clearly depicted in these images, it is evident that the vibrations were captured.

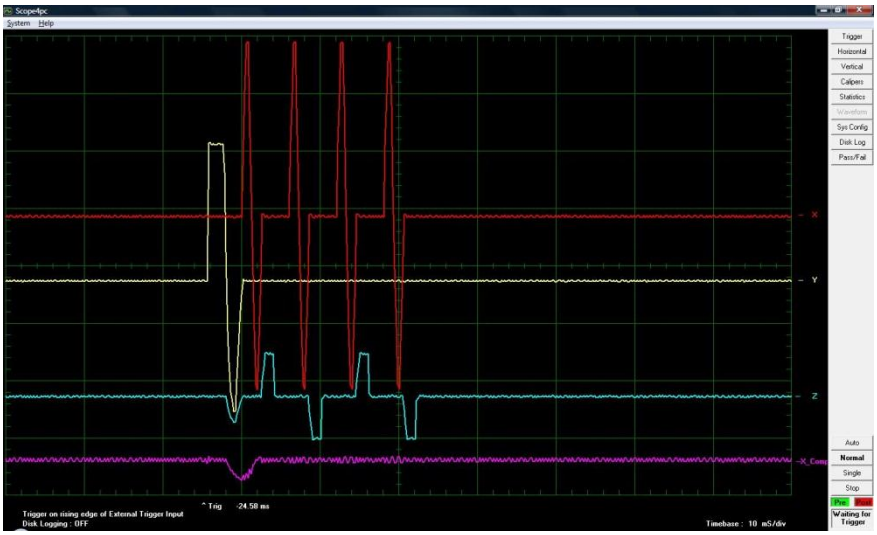

Fig. 69. Scope waveform of the multi-echo elastography pulse sequence. Four readout pulses are generated by the z gradient, each preceded by a bipolar motion sensitizing gradient pulse on the x axis. RF coil phase compensation is provided by the fourth gradient channel.

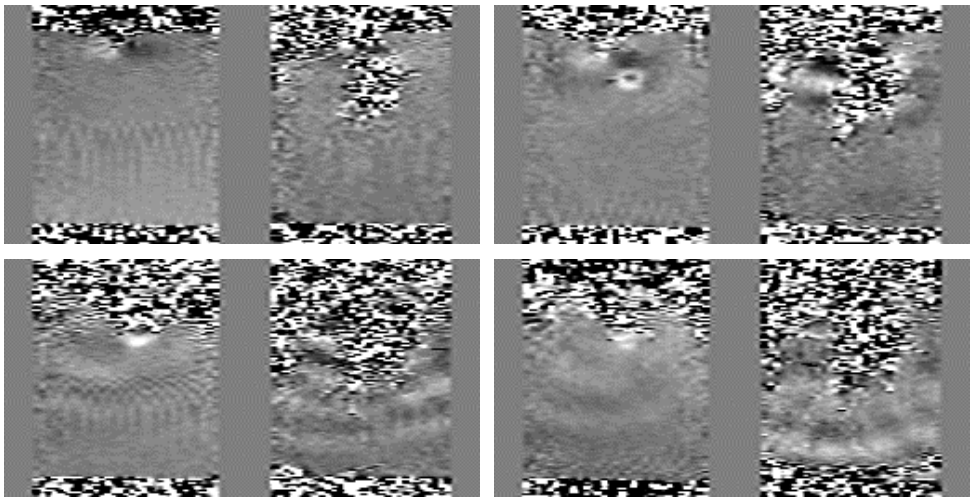

Fig. 70. Four SEA images resulting from four recalled echoes following a single RF excitation and mechanical vibration. Each image is the result of the cumulative motion sensitization of the previous images.

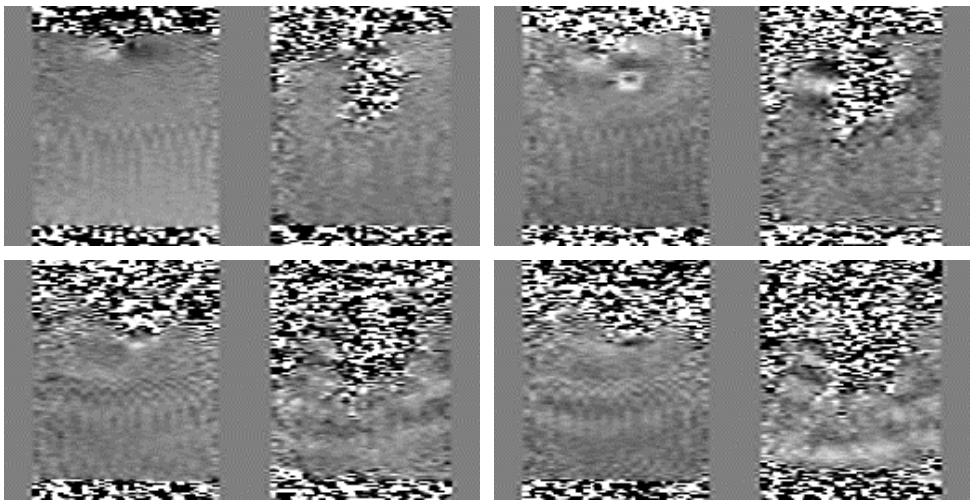

Fig. 71. Four SEA images resulting from four recalled echoes following a single RF excitation and mechanical vibration with correction. The previous wave images are subtracted to visualize the motion at each time point.

The third protocol was to obtain an accelerated high resolution data set in order to explore potential applications in μMRE. Images were obtained simultaneously from the bottom and top slices at a resolution of 156.3 x 125 μm using a sinc pulse which excited two 1 mm thick slices separated by 8.5 mm as shown in Fig. 72. These were obtained in 1.6 minutes with a 1.5 s TR, while a fully encoded dataset of the same resolution would have required 32 minutes (16 minutes for each slice), likely with additional time for averaging due to use of a large receive coil. It was necessary to use a thicker slice closer to the bottom array to obtain sufficient SNR at such small voxel sizes. An elastography dataset of 240 frames as described above was also obtained at this resolution in 6.4 hours, one frame of which is shown in Fig. 73. To acquire the same dataset with the volume coil would have required 128 hours (64 hours for each slice), plus additional time for averaging.

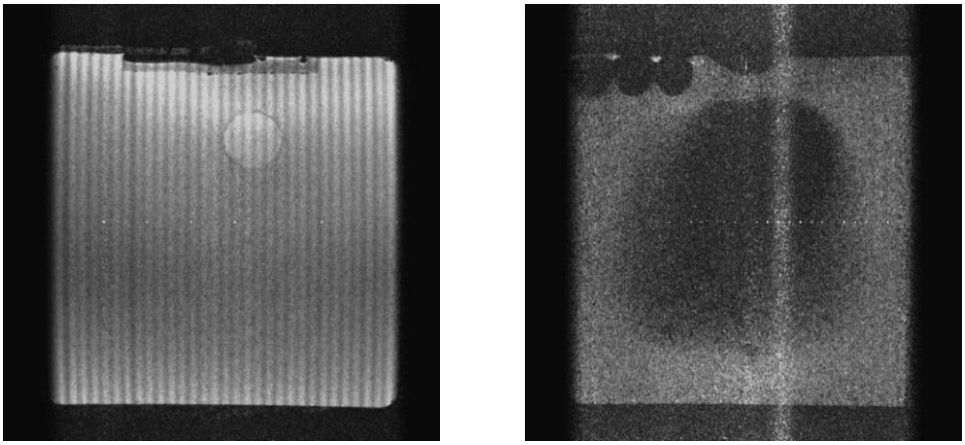

Fig. 72. Accelerated high resolution magnitude images of elastography phantom. The left hand image was acquired using the bottom array while the right hand image was acquired simultaneously by the top array. The image from the bottom array clearly shows the round soft gel occlusion, while a large signal void is present in the top slice.

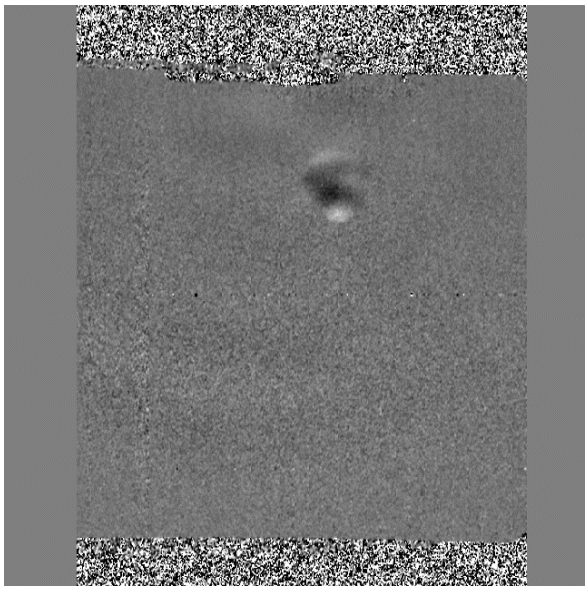

Fig. 73. Accelerated high resolution elastography wave image. Frame 177 from the bottom array extracted from a set of 240 frames. The complex wave motion within the soft occlusion is better visualized at higher resolution.

While these are only preliminary results, they indicate the potential utility of the wide field of view probe in MR elastography, both for very fast low resolution studies which may benefit mechanical transient based MRE and high resolution studies which may be useful in microscopic MRE. Having access to both imaging regimes in a single study may be of importance in time sensitive applications, such as destructive testing or imaging of biological samples with a limited viability.

6. CONCLUSIONS

A platform has been developed which allows highly parallel magnetic resonance imaging of a 6.4 cm x 6.4 cm x 1 cm sample over a range of spatio-temporal imaging regimes. By implementing a custom fourth gradient channel, the RF phase gradient negatively affecting ultra-fast and highly accelerated imaging using dual-sided or "sandwich" receive arrays is corrected. Using the fourth gradient channel enables simultaneous SEA imaging at the lower and upper boundaries of a sample in which slices are received by arrays below and above the sample in parallel. The fourth gradient channel also enables acquisition of highly accelerated or "resolution-enhanced" images acquired in two or four echoes from both sides of the sandwich array with increased efficiency, such that each echo yields useful data from all sixty-four receive channels. Similarly, SEA and highly accelerated imaging using 3D pulse sequences is enabled. The sandwich receive array is also capable of wide field of view magnetic resonance microscopy and high resolution imaging through the volume of the sample, with highest resolution available at the array surfaces where coil sensitivity is greatest.

SEA imaging at the upper and lower boundaries of the sample may be useful for capturing dynamic events such as flow, mixing, or non-repeatable and destructive processes. Of particular note is this system's ability to switch between high speed and high resolution imaging modes. An application that may benefit from this capability is magnetic resonance elastography (MRE). Samples with variable elasticity in the direction normal to the array planes could benefit from SEA imaging at two boundaries.

Elastography of destructive events may also be served by SEA which allows capture of wave images in single echoes during a dynamic process. The probe's high resolution and microscopy capabilities may be useful in microscopic MRE, in which higher imaging resolution is necessary to visualize vibrations having high spatial frequencies, allowing extraction of high resolution elasticity maps. MRE in which the applied mechanical vibration frequency is swept could also benefit from savings in scan time. The probe is also suited for high resolution three dimensional imaging of biological samples, allowing straightforward changing of arrays and samples for different experiments.

While the through-slice gradient places some constraints on this technique, use of thin slices in SEA imaging largely overcomes the problem. In the results shown, a fourth gradient pulse producing ±12 rad/cm over a 1 cm slab using half-mm thick slices results in a theoretical signal loss of approximately 50% at the edges of the field of view, however after channel-to-channel normalizations were applied to SEA images this was found to have little impact on image quality. The dual slice SEA images shown were reconstructed with only ±8 rad/cm, reducing signal loss at the edges. The resolution enhanced imaging benefited significantly from the fourth gradient until artifacts induced by the through-slice gradient became dominant. One way to further decrease such artifacts in SEA imaging may be to try alternative normalization strategies, as thin features become overly-bright using the present method, contributing to increased artifact power. Finally, 3D SEA is enabled provided the y resolution is high enough to avoid problems due to the offset in y *k*-space produced by the through-slice gradient.

Future work may include improving the rigidity of the fourth gradient coil to allow faster rise times and shorter duration phase compensation gradient pulses. As the current prototype coil consists of printed circuit boards mounted to an acrylic former, it is subject to vibrations when employing more aggressive gradient pulses, important for the fastest SEA imaging sequences. Such vibrations may adversely affect delicate samples and could shift the position of the sample, introducing image artifacts. By casting the coil in an epoxy resin, its rigidity would be significantly improved. Adding water cooling and thermal sensors may also become necessary for ultra-fast imaging at sustained high duty cycles. Furthermore, only linearity and field of view were considered in the electromagnetic design of the gradient coil. Stored energy and dissipated power optimizations may be important for fast rise times and greater efficiency. While simulations indicate that a biplanar gradient coil provides improved linearity over a uniplanar coil, further investigation of an optimized uniplanar gradient coil is warranted. Such a coil would allow a more open imaging platform. Additionally, the benefits of a shielded gradient coil could be considered.

Improved RF coil arrays based on other geometries remain the subject of investigation. Array elements with spatially confined field patterns, low coupling to adjacent coils, and deep penetration are ideal for high resolution imaging through the volume of a sample and ultra-fast SEA imaging in which localization is provided by the array alone along one dimension. However, there are many trade-offs in designing such coils. Alternative decoupling networks and preamplifier configurations could provide additional freedom in choosing element geometries. Improvement of the varactor biasing

method and routing of the receive cables into the magnet would also allow easier and more reliable installation of the imaging platform.

Finally, additional testing of applications which benefit from this imaging platform is important. There is further work to be done in MR elastography, especially in improving the images obtained from multiple recalled echoes and continuing with microscopic MR elastography. Tissue samples provided by collaborators would allow additional assessment of the utility of the platform especially in MR microscopy, while setting up more detailed experiments demanding single shot imaging, such as destructive testing of tissues, would demonstrate the utility of the fastest imaging modes.

REFERENCES

[1] E. Fukushima, "Nuclear magnetic resonance as a tool to study flow," *Annu. Rev. Fluid. Mech.*, vol. 31, pp. 95-123, 1999.

[2] C. Elkins and M. Alley, "Magnetic resonance velocimetry: Applications of magnetic resonance imaging in the measurement of fluid motion," *Exp. Fluids*, vol. 43, pp. 823-858, 2007.

[3] P. Chen and Z. Sun, "A review of non-destructive methods for quality evaluation and sorting of agricultural products," *J. Agric. Engng. Res.*, vol. 49, pp. 85-98, 1991.

[4] A. J. Sederman, M. L. Johns, A. S. Bramley, P. Alexander, and L. F. Gladden, "Magnetic resonance imaging of liquid flow and pore structure within packed beds," *Chem. Eng. Sci.*, vol. 52, pp. 2239-2250, 1997.

[5] G. Johnson, H. Benveniste, R. Black, L. Hedlund, R. Maronpot, and B. Smith, "Histology by magnetic resonance microscopy," *Magn. Reson. Q.*, vol. 9, p. 1, 1993.

[6] P. T. Callaghan, *Principles of Nuclear Magnetic Resonance Microscopy*. Oxford, UK: Clarendon Press, 1991.

[7] S. M. Wright, M. P. McDougall, and D. G. Brown, "Single echo acquistion of MR images using RF coil arrays," in *Proc. 2nd Joint IEEE Engineering in Medicine and Biology Society and Biomedical Engineering Society Conf.*, Houston, TX, 2002, pp. 1181-1182 vol.2.

[8] M. P. McDougall and S. M. Wright, "Initial results in wide-field 3D MR microscopy using parallel imaging," in *Proc. 4th IEEE Int. Symp. Biomedical Imaging: From Nano to Macro*, Washington, DC, 2007, pp. 1072-1075.

[9] M. P. McDougall and S. M. Wright, "Overcoming phase effects of voxel-sized coils in planar and cylindrical arrays," in *Proc. 26th Annu. Int. Conf. IEEE Engineering in Medicine and Biology Society*, San Francisco, CA, 2004, pp. 1060-1063.

[10] S. M. Wright and M. P. McDougall, "Coil effect on k-space line selection in highly accelerated parallel imaging," in *Proc. 4th IEEE Int. Symp. Biomedical Imaging: From Nano to Macro*, Washington, DC, 2007, pp. 1016-1019.

[11] A. Haase, J. Frahm, D. Matthaei, W. Hanicke, and K. D. Merboldt, "FLASH imaging. Rapid NMR imaging using low flip-angle pulses," *J. Magn. Reson.,* vol. 67, pp. 258-266, 1986.

[12] P. Mansfield, "Multi-planar image formation using NMR spin echoes," *J. Phys. C: Solid State Phys.,* vol. 10, p. L55, 1977.

[13] C. B. Ahn, J. H. Kim, and Z. H. Cho, "High-speed spiral-scan echo planar NMR imaging-I," *IEEE Trans. Med. Imag.,* vol. 5, pp. 2-7, 1986.

[14] E. M. Haacke, *Magnetic Resonance Imaging: Physical Principles and Sequence Design*. New York, NY: John Wiley & Sons, 1999.

[15] R. Turner, "Gradient coil systems," in *Encyclopedia of Magnetic Resonance*, R. K. Harris and R. E. Wasylishen, Eds., Chichester: John Wiley & Sons, Ltd., 2007, DOI: 10.1002/9780470034590.emrstm0192.

[16] B. Zhang, Y.-F. Yen, B. A. Chronik, G. C. McKinnon, D. J. Schaefer, and B. K. Rutt, "Peripheral nerve stimulation properties of head and body gradient coils of various sizes," *Magn. Reson. Med.,* vol. 50, pp. 50-58, 2003.

[17] R. M. Heidemann, Ö. Özsarlak, P. M. Parizel, J. Michiels, B. Kiefer, V. Jellus, M. Müller, F. Breuer, M. Blaimer, M. A. Griswold, and P. M. Jakob, "A brief review of parallel magnetic resonance imaging," *Eur. Radiol.,* vol. 13, pp. 2323-2337, 2003.

[18] D. J. Larkman and R. G. Nunes, "Parallel magnetic resonance imaging," *Phys. Med. Biol.,* vol. 52, p. R15, 2007.

[19] P. B. Roemer, W. A. Edelstein, C. E. Hayes, S. P. Souza, and O. M. Mueller, "The NMR phased array," *Magn. Reson. Med.,* vol. 16, pp. 192-225, 1990.

[20] J. W. Carlson, "An algorithm for NMR imaging reconstruction based on multiple RF receiver coils," *J. Magn. Reson.,* vol. 74, pp. 376-380, 1987.

[21] J. R. Kelton, R. L. Magin, and S. M. Wright, "An algorithm for rapid image acquisition using multiple receiver coils," in *Proc. Int. Society for Magnetic Resonance in Medicine,* Amsterdam, The Netherlands, 1989, p. 1172.

[22] M. Hutchinson and U. Raff, "Fast MRI data acquisition using multiple detectors," *Magn. Reson. Med.,* vol. 6, pp. 87-91, 1988.

[23] D. K. Sodickson and W. J. Manning, "Simultaneous acquisition of spatial harmonics (SMASH): Fast imaging with radiofrequency coil arrays," *Magn. Reson. Med.,* vol. 38, pp. 591-603, 1997.

[24] K. P. Pruessmann, M. Weiger, M. B. Scheidegger, and P. Boesiger, "SENSE: Sensitivity encoding for fast MRI," *Magn. Reson. Med.,* vol. 42, pp. 952-962, 1999.

[25] S. M. Wright, M. P. McDougall, and N. Yallapragada, "Rapid flow imaging using single echo acquisition MRI," in *Proc. Int. Society for Magnetic Resonance in Medicine*, Miami, FL, 2005, p. 289.

[26] S. M. Wright, M. P. McDougall, and J. C. Bosshard, "Progress in visualizing turbulent flow using single-echo acquisition imaging," in *Proc. 28th Annu. Int. Conf. IEEE Engineering in Medicine and Biology Society*, New York, NY, 2006, pp. 4877-4880.

[27] J. C. Bosshard, "Applications of MRI in fluidics: Single echo acquisition MRI toward microfluidics," B.S. thesis, Dept. Elect. Eng., Texas A&M Univ., College Station, TX, 2006.

[28] J. C. Bosshard, N. Yallapragada, M. P. McDougall, and S. M. Wright, "High speed MR elastography using SEA imaging," in *Proc. Int. Society for Magnetic Resonance in Medicine,* Toronto, ON, Canada, 2008, p. 831.

[29] N. Yallapragada, "A 64-channel personal computer based image reconstruction system and applications in single echo acquisition magnetic resonance elastography and ultra-fast magnetic resonance imaging," Ph.D. dissertation, Dept. Elect. Eng., Texas A&M Univ., College Station, TX, 2008.

[30] P. C. Lauterbur, "Image formation by induced local interactions: Examples employing nuclear magnetic resonance," *Nature,* vol. 242, pp. 190-191, 1973.

[31] D. B. Twieg, "The k-trajectory formulation of the NMR imaging process with applications in analysis and synthesis of imaging methods," *Med. Phys.,* vol. 10, p. 610, 1983.

[32] V. J. Wedeen, Y.-S. Chao, and J. L. Ackerman, "Dynamic range compression in MRI by means of a nonlinear gradient pulse," *Magn. Reson. Med.,* vol. 6, pp. 287-295, 1988.

[33] D. L. Parker and J. R. Hadley, "Multiple-region gradient arrays for extended field of view, increased performance, and reduced nerve stimulation in magnetic resonance imaging," *Magn. Reson. Med.,* vol. 56, pp. 1251-1260, 2006.

[34] J. Hennig, A. Welz, G. Schultz, J. Korvink, Z. Liu, O. Speck, and M. Zaitsev, "Parallel imaging in non-bijective, curvilinear magnetic field gradients: A concept study," *Magn. Reson. Mater. Phys., Biol. Med.,* vol. 21, pp. 5-14, 2008.

[35] D. Gallichan, C. A. Cocosco, A. Dewdney, G. Schultz, A. Welz, J. Hennig, and M. Zaitsev, "Simultaneously driven linear and nonlinear spatial encoding fields in MRI," *Magn. Reson. Med.*, vol. 65, pp. 702-714, 2011.

[36] J. P. Stockmann, P. A. Ciris, G. Galiana, L. Tam, and R. T. Constable, "O-space imaging: Highly efficient parallel imaging using second-order nonlinear fields as encoding gradients with no phase encoding," *Magn. Reson. Med.*, vol. 64, pp. 447-456, 2010.

[37] R. E. Feldman, T. J. Scholl, J. K. Alford, W. B. Handler, C. T. Harris, and B. A. Chronik, "Results for diffusion-weighted imaging with a fourth-channel gradient insert," *Magn. Reson. Med.*, vol. 66, pp. 1798-1808, 2011.

[38] C. E. Hayes, "An efficient, highly homogeneous radiofrequency coil for whole-body NMR imaging at 1.5 T," *J. Magn. Reson. A*, vol. 63, p. 622, 1985.

[39] S. M. Wright and L. L. Wald, "Theory and application of array coils in MR spectroscopy," *NMR Biomed.*, vol. 10, pp. 394-410, 1997.

[40] M. A. Griswold, P. M. Jakob, M. Nittka, J. W. Goldfarb, and A. Haase, "Partially parallel imaging with localized sensitivities (PILS)," *Magn. Reson. Med.*, vol. 44, pp. 602-609, 2000.

[41] M. P. McDougall and S. M. Wright, "64-channel array coil for single echo acquisition magnetic resonance imaging," *Magn. Reson. Med.*, vol. 54, pp. 386-392, 2005.

[42] M. Weiger, K. Pruessmann, and P. Boesiger, "2D sense for faster 3D MRI," *Magn. Reson. Mater. Phys., Biol. Med.*, vol. 14, pp. 10-19, 2002.

[43] M. Weiger, K. P. Pruessmann, A. Kassner, G. Roditi, T. Lawton, A. Reid, and P. Boesiger, "Contrast-enhanced 3D MRA using SENSE," *J. Magn. Reson. Imaging*, vol. 12, pp. 671-677, 2000.

[44] M. Weiger, K. P. Pruessmann, and P. Boesiger, "Cardiac real-time imaging using SENSE," *Magn. Reson. Med.*, vol. 43, pp. 177-184, 2000.

[45] X. Golay, K. P. Pruessmann, M. Weiger, G. R. Crelier, P. J. M. Folkers, S. S. Kollias, and P. Boesiger, "PRESTO-SENSE: An ultrafast whole-brain fMRI technique," *Magn. Reson. Med.*, vol. 43, pp. 779-786, 2000.

[46] D. G. Brown, M. P. McDougall, and S. M. Wright, "Receiver design for parallel imaging with large arrays," in *Proc. Int. Society for Magnetic Resonance in Medicine*, Honolulu, HI, 2002, p. 863.

[47] S. M. Wright and M. P. McDougall, "MR imaging at sub-millisecond frame rates," in *Proc. Int. Society for Magnetic Resonance in Medicine*, Honolulu, HI, 2009, p. 259.

[48] J. A. Bankson and S. M. Wright, "Simulation-based investigation of partially parallel imaging with a linear array at high accelerations," *Magn. Reson. Med.*, vol. 47, pp. 777-786, 2002.

[49] A. Jesmanowicz, W. Froncisz, and J. S. Hyde, "A complication in prescan strategy when using surface coils," *Magn. Reson. Med.*, vol. 5, pp. 318-322, 1987.

[50] M. P. McDougall and S. M. Wright, "Coil phase compensation for single echo acquisition (SEA) imaging," in *Proc. Int. Society for Magnetic Resonance in Medicine*, Toronto, ON, Canada, 2004, p. 330.

[51] J. C. Bosshard, M. P. McDougall, and S. M. Wright, "An insertable fourth gradient coil for phase compensation in SEA imaging," *IEEE Trans. Biomed. Eng.*, 2012, Submitted.

[52] M. P. McDougall and S. M. Wright, "Investigation of coil phase compensation in 3D imaging at very high acceleration factors," *J. Magn. Reson. Imaging*, vol. 25, pp. 1305-1311, 2007.

[53] M. P. McDougall and S. M. Wright, "Implementation of single-shot 3D imaging using the SEA technique," in *Proc. Int. Society for Magnetic Resonance in Medicine*, Miami, FL, 2005, p. 2416.

[54] S. M. Wright and M. P. McDougall, "Resolution enhancement in single echo acquisition (SEA) MR imaging," in *Proc. Int. Society for Magnetic Resonance in Medicine*, Toronto, ON, Canada, 2003, p. 2338.

[55] J. C. Sharp and S. B. King, "MRI using radiofrequency magnetic field phase gradients," *Magn. Reson. Med.*, vol. 63, pp. 151-161, 2010.

[56] P. Glover and P. Mansfield, "Limits to magnetic resonance microscopy," *Rep. Prog. Phys.*, vol. 65, p. 1489, 2002.

[57] T. L. Peck, R. L. Magin, and P. C. Lauterbur, "Design and analysis of microcoils for NMR microscopy," *J. Magn. Reson. B*, vol. 108, pp. 114-124, 1995.

[58] T. Neuberger and A. Webb, "Radiofrequency coils for magnetic resonance microscopy," *NMR Biomed.*, vol. 22, pp. 975-981, 2009.

[59] J. B. Aguayo, S. J. Blackband, J. Schoeniger, M. A. Mattingly, and M. Hintermann, "Nuclear magnetic resonance imaging of a single cell," *Nature,* vol. 322, pp. 190-191, 1986.

[60] L. Ciobanu, D. A. Seeber, and C. H. Pennington, "3D MR microscopy with resolution 3.7 μm by 3.3 μm by 3.3 μm," *J. Magn. Reson.,* vol. 158, pp. 178-182, 2002.

[61] L. Ciobanu, A. G. Webb, and C. H. Pennington, "Magnetic resonance imaging of biological cells," *Prog. Nucl. Magn. Reson. Spectrosc.,* vol. 42, pp. 69-93, 2003.

[62] X. Zhang and A. Webb, "Design of a capacitively decoupled transmit/receive NMR phased array for high field microscopy at 14.1 T," *J. Magn. Reson.,* vol. 170, pp. 149-155, 2004.

[63] B. P. Sutton, L. Ciobanu, X. Zhang, and A. Webb, "Parallel imaging for NMR microscopy at 14.1 tesla," *Magn. Reson. Med.,* vol. 54, pp. 9-13, 2005.

[64] E. Laistler, R. Loewe, and E. Moser, "Magnetic resonance microimaging of human skin vasculature in vivo at 3 tesla," *Magn. Reson. Med.,* vol. 65, pp. 1718-1723, 2011.

[65] K. R. Demarest, *Engineering Electromagnetics*. Upper Saddle River, NJ: Prentice Hall, 1998.

[66] Z. H. Cho and J. H. Yi, "A novel type of surface gradient coil," *J. Magn. Reson.,* vol. 94, pp. 471-485, 1991.

[67] Z. H. Cho and J. H. Yi, "Planar surface gradient coil," *Concepts Magn. Reson.,* vol. 7, pp. 95-114, 1995.

[68] J. C. Bosshard, M. P. McDougall, and S. M. Wright, "Overcoming coil phase effects in highly accelerated imaging with a dedicated fourth gradient channel," in *Proc. Int. Society for Magnetic Resonance in Medicine*, Honolulu, HI, 2009, p. 3071.

[69] J. S. Boyer, S. M. Wright, and J. R. Porter, "An automated measurement system for characterization of RF and gradient coil parameters," *J. Magn. Reson. Imaging,* vol. 8, pp. 740-747, 1998.

[70] R. Turner, "Gradient coil design: A review of methods," *Magn. Reson. Imaging,* vol. 11, pp. 903-920, 1993.

[71] R. Turner, "A target field approach to optimal coil design," *J. Phys. D: Appl. Phys.,* vol. 19, p. L147, 1986.

[72] R. Turner and R. M. Bowley, "Passive screening of switched magnetic field gradients," *J. Phys. E: Sci. Instrum.*, vol. 19, p. 876, 1986.

[73] M. Martens, L. Petropoulos, R. Brown, J. Andrews, M. Morich, and J. Patrick, "Insertable biplanar gradient coil for MR imaging," *Rev. Sci. Instrum.*, vol. 62, pp. 2639–45, 1991.

[74] J. Jin, *Electromagnetic Analysis and Design in Magnetic Resonance Imaging*. Boca Raton, FL: CRC Press, 1999.

[75] W. A. Edelstein and F. Schenck, "Current streamline method for coil construction," U.S. Patent 4,840,700, Jun. 20, 1989.

[76] M. A. Brideson, L. K. Forbes, and S. Crozier, "Determining complicated winding patterns for shim coils using stream functions and the target-field method," *Concepts Magn. Reson.*, vol. 14, pp. 9-18, 2002.

[77] B. Aksel, L. Marinelli, B. D. Collick, C. V. Morze, P. A. Bottomley, and C. J. Hardy, "Local planar gradients with order-of-magnitude strength and speed advantage," *Magn. Reson. Med.*, vol. 58, pp. 134-143, 2007.

[78] K. Feng, N. Hollingsworth, M. McDougall, and S. Wright, "A 64-channel transmitter for investigating parallel transmit MRI," *IEEE Trans. Biomed. Eng.*, vol. 59, pp. 2152-2160, 2012.

[79] J. C. Bosshard, E. P. Eigenbrodt, M. P. McDougall, and S. M. Wright, "A fourth gradient to overcome slice dependent phase effects of voxel-sized coils in planar arrays," in *Proc. 32nd Annu. Int. Conf. IEEE Engineering in Medicine and Biology Society*, Buenos Aires, Argentina, 2010, pp. 6649-6652.

[80] J. C. Bosshard, M. P. McDougall, and S. M. Wright, "SEA imaging using a dual planar array and fourth gradient coil for phase compensation," in *Proc. Int. Society for Magnetic Resonance in Medicine*, Melbourne, Australia, 2012, p. 2605.

[81] E. A. Marshall, J. J. Listinsky, T. L. Ceckler, J. Szumowski, R. G. Bryant, and J. P. Hornak, "Magnetic resonance imaging using a ribbonator: Hand and wrist," *Magn. Reson. Med.*, vol. 9, pp. 369-378, 1989.

[82] C.-W. Chang, S. M. Wright, and M. P. McDougall, "Element design for increased sensitivity in 64-channel wide-field-of-view microscopy," in *Proc. Int. Society for Magnetic Resonance in Medicine*, Honolulu, HI, 2009, p. 102.

[83] C.-W. Chang, K. L. Moody, and M. P. McDougall, "An improved element design for 64-channel planar imaging," *Concepts Magn. Reson.*, vol. 39B, pp. 159-165, 2011.

[84] D. A. Seeber, J. Jevtic, and A. Menon, "Floating shield current suppression trap," *Concepts Magn. Reson.*, vol. 21B, pp. 26-31, 2004.

[85] M. C. Murphy, K. J. Glaser, A. Manduca, J. P. Felmlee, J. Huston, III, and R. L. Ehman, "Analysis of time reduction methods for magnetic resonance elastography of the brain," *Magn. Reson. Imaging*, vol. 28, pp. 1514-1524, 2010.

[86] G. McGibney, M. R. Smith, S. T. Nichols, and A. Crawley, "Quantitative evaluation of several partial fourier reconstruction algorithms used in MRI," *Magn. Reson. Med.*, vol. 30, pp. 51-59, 1993.

[87] A. J. Sederman, M. D. Mantle, C. Buckley, and L. F. Gladden, "MRI technique for measurement of velocity vectors, acceleration, and autocorrelation functions in turbulent flow," *J. Magn. Reson.*, vol. 166, pp. 182-189, 2004.

[88] R. Muthupillai, D. Lomas, P. Rossman, J. Greenleaf, A. Manduca, and R. Ehman, "Magnetic resonance elastography by direct visualization of propagating acoustic strain waves," *Science*, vol. 269, pp. 1854-1857, 1995.

[89] S. F. Othman, H. Xu, T. J. Royston, and R. L. Magin, "Microscopic magnetic resonance elastography (μMRE)," *Magn. Reson. Med.*, vol. 54, pp. 605-615, 2005.

[90] Y. K. Mariappan, K. J. Glaser, and R. L. Ehman, "Magnetic resonance elastography: A review," *Clin. Anat.*, vol. 23, pp. 497-511, 2010.

[91] M. Yin, J. A. Talwalkar, K. J. Glaser, A. Manduca, R. C. Grimm, P. J. Rossman, J. L. Fidler, and R. L. Ehman, "Assessment of hepatic fibrosis with magnetic resonance elastography," *Clin. Gastroenterol. Hepatol.*, vol. 5, pp. 1207-1213, 2007.

[92] S. A. Kruse, G. H. Rose, K. J. Glaser, A. Manduca, J. P. Felmlee, J. R. Clifford Jr., and R. L. Ehman, "Magnetic resonance elastography of the brain," *Neuroimage*, vol. 39, pp. 231-237, 2008.

[93] J. R. Basford, T. R. Jenkyn, K.-N. An, R. L. Ehman, G. Heers, and K. R. Kaufman, "Evaluation of healthy and diseased muscle with magnetic resonance elastography," *Arch. Phys. Med. Rehabil.*, vol. 83, pp. 1530-1536, 2002.

[94] A. L. McKnight, J. L. Kugel, P. J. Rossman, A. Manduca, L. C. Hartmann, and R. L. Ehman, "MR elastography of breast cancer: Preliminary results," *Am. J. Roentgenol.*, vol. 178, pp. 1411-1417, 2002.

[95] A. Manduca, T. E. Oliphant, M. A. Dresner, J. L. Mahowald, S. A. Kruse, E. Amromin, J. P. Felmlee, J. F. Greenleaf, and R. L. Ehman, "Magnetic resonance elastography: Non-invasive mapping of tissue elasticity," *Med. Image Anal.*, vol. 5, pp. 237-254, 2001.

[96] S. Maderwald, K. Uffmann, C. J. Galbán, A. de Greiff, and M. E. Ladd, "Accelerating MR elastography: A multiecho phase-contrast gradient-echo sequence," *J. Magn. Reson. Imaging*, vol. 23, pp. 774-780, 2006.

[97] S. A. Kruse, R. C. Grimm, D. S. Lake, A. Manduca, and R. L. Ehman, "Fast EPI based 3D MR elastography of the brain," in *Proc. Int. Society for Magnetic Resonance in Medicine*, Seattle, WA, 2006, p. 3385.

[98] K. J. Glaser, J. P. Felmlee, and R. L. Ehman, "Rapid MR elastography using selective excitations," *Magn. Reson. Med.*, vol. 55, pp. 1381-1389, 2006.

[99] D. W. Stanley, S. K. Venkatesh, M. Yin, K. Hwang, and R. L. Ehman, "Acceleration of MR elastography with parallel MR imaging," in *Proc. Int. Society for Magnetic Resonance in Medicine*, Toronto, ON, Canada, 2008, p. 2612.

[100] P. J. McCracken, A. Manduca, J. Felmlee, and R. L. Ehman, "Mechanical transient-based magnetic resonance elastography," *Magn. Reson. Med.*, vol. 53, pp. 628-639, 2005.

[101] J. Rump, D. Klatt, J. Braun, C. Warmuth, and I. Sack, "Fractional encoding of harmonic motions in MR elastography," *Magn. Reson. Med.*, vol. 57, pp. 388-395, 2007.

[102] P. Asbach, D. Klatt, U. Hamhaber, J. Braun, R. Somasundaram, B. Hamm, and I. Sack, "Assessment of liver viscoelasticity using multifrequency MR elastography," *Magn. Reson. Med.*, vol. 60, pp. 373-379, 2008.

[103] B. Robert, R. Sinkus, J.-L. Gennisson, and M. Fink, "Application of DENSE-MR-elastography to the human heart," *Magn. Reson. Med.*, vol. 62, pp. 1155-1163, 2009.

[104] M. Yin, O. Rouvière, K. J. Glaser, and R. L. Ehman, "Diffraction-biased shear wave fields generated with longitudinal magnetic resonance elastography drivers," *Magn. Reson. Imaging*, vol. 26, pp. 770-780, 2008.

[105] Y. K. Mariappan, K. J. Glaser, A. Manduca, A. J. Romano, S. K. Venkatesh, M. Yin, and R. L. Ehman, "High-frequency mode conversion technique for stiff lesion detection with magnetic resonance elastography (MRE)," *Magn. Reson. Med.*, vol. 62, pp. 1457-1465, 2009.

[106] O. Lopez, K. K. Amrami, A. Manduca, P. J. Rossman, and R. L. Ehman, "Developments in dynamic MR elastography for in vitro biomechanical assessment of hyaline cartilage under high-frequency cyclical shear," *J. Magn. Reson. Imaging*, vol. 25, pp. 310-320, 2007.

[107] N. S. Shah, S. A. Kruse, D. J. Lager, G. Farell-Baril, J. C. Lieske, B. F. King, and R. L. Ehman, "Evaluation of renal parenchymal disease in a rat model with magnetic resonance elastography," *Magn. Reson. Med.*, vol. 52, pp. 56-64, 2004.

[108] T. K. Yasar, T. J. Royston, and R. L. Magin, "Taking MR elastography (MRE) to the microscopic scale," in *Proc. 8th IEEE Int. Symp. Biomedical Imaging: From Nano to Macro*, Chicago, IL, 2011, pp. 1618-1623.

[109] S. F. Othman, E. T. Curtis, S. A. Plautz, A. K. Pannier, S. D. Butler, and H. Xu, "MR elastography monitoring of tissue-engineered constructs," *NMR Biomed.*, vol. 25, pp. 452-463, 2012.

[110] T. Boulet, M. L. Kelso, and S. F. Othman, "Microscopic magnetic resonance elastography of traumatic brain injury model," *J. Neurosci. Methods*, vol. 201, pp. 296-306, 2011.

[111] M. A. Dresner, G. H. Rose, P. J. Rossman, R. Muthupillai, A. Manduca, and R. L. Ehman, "Magnetic resonance elastography of skeletal muscle," *J. Magn. Reson. Imaging*, vol. 13, pp. 269-276, 2001.

[112] I. Sack, E. Gedat, J. Bernarding, G. Buntkowsky, and J. Braun, "Magnetic resonance elastography and diffusion-weighted imaging of the sol/gel phase transition in agarose," *J. Magn. Reson.*, vol. 166, pp. 252-261, 2004.

[113] T. Wu, J. P. Felmlee, J. F. Greenleaf, S. J. Riederer, and R. L. Ehman, "Assessment of thermal tissue ablation with MR elastography," *Magn. Reson. Med.*, vol. 45, pp. 80-87, 2001.

[114] K. Riek, D. Klatt, H. Nuzha, S. Mueller, U. Neumann, I. Sack, and J. Braun, "Wide-range dynamic magnetic resonance elastography," *J. Biomech.*, vol. 44, pp. 1380-1386, 2011.

[115] S. M. Wright, "Multidisciplinary approaches to MR engineering," in *Proc. Int. Society for Magnetic Resonance in Medicine*, Berlin, Germany, 2007, p. 660.

[116] S. M. Wright, M. P. McDougall, K. Feng, N. A. Hollingsworth, J. C. Bosshard, and C.-W. Chang, "Highly parallel transmit/receive systems for dynamic MRI," in *Proc. 31st Annu. Int. Conf. IEEE Engineering in Medicine and Biology Society*, Minneapolis, MN, 2009, pp. 4053-4056.

APPENDIX A

A.1. Calculation of the Cutting Pattern

This section annotates the code used to design the biplanar target field gradient coil, showing the step-by-step procedure to build the target field coil discussed in Section 3.4.

```
 %%
clear all;close all;clc
% Target Field Calculator
u0=4*pi*10^-7;
```

First, the amplitude of the gradient at the target plane, GxA, is specified in G/cm and converted to T/m. Here, the desired strength is 0.00734 G/cm at the target plane.

```
% Specify Target Field
GxA=.00734; %G/cm
GxA=GxA/10000*100; %T/m
```

Next the user specifies the total area in space over which the target field will be defined and calculated, wx and wz, in meters. This also determines the dimensions over which the current density is calculated. This area should be large enough to allow the target field and associated current to reach zero and to avoid Fourier transform artifacts. Here a region of 50 cm x 50 cm was selected. The x and z coordinate points are computed and the location of the target plane (amount of offset from the y = 0 plane), y, is also input in meters. The variable a specifies the distance between the y = 0 plane and the two current planes in meters. Here the target plane is 0.1 mm from the y = 0 plane and the two current planes are at y = ±4 cm. A set of grid vectors are computed using the meshgrid command.

```
% Calculation area
wx=50e-2;
wz=50e-2;
x=linspace(-wx,wx,1024);
y=.01e-2;
a=4e-2;
z=linspace(-wz,wz,1024);
[xi,zi]=meshgrid(x,z);
```

Next, the desired physical extent of the coil is specified in meters. Here, x = ±10 cm and z = ±16.8 cm were selected. Beyond this region the target field is zero, although it is slightly larger after apodization, shown below. The built-in MATLAB constant eps (epsilon – a very small number) is included to avoid dividing by zero later.

```
% Coil size
wxa=10e-2;
wxa=wxa-eps;
wza=16.8e-2-eps;
```

The inputs xsiz and zsiz specify the extent of the linear region of the target field before apodization, here defined as x = ±8.4 cm z = ±8.4 cm. These inputs set the boundaries beyond which the linearly-varying target field begins returning to zero along x or reversing along z. For this coil, in the x direction the field begins returning to zero at x = ±8.4 cm and reaches zero at x = ±10 cm. However, along z the field first reverses at z = ±8.4 cm before returning to zero at z = ±16.8 cm. This reversal is needed so that the "area under the curve" of the field along z is zero, forcing a reversal of the current density along z so the cutting pattern will form closed loops.

```
% Target Field Area
xsiz=8.4e-2;
zsiz=8.4e-2;
```

The number of turns is used to compute the number of equally spaced contours used to generate the discrete cutting pattern.

```
% Turns
turns=16;
```

The following section calculates the target field distribution, including the field reversal region described above.

```
xsiz=xsiz-eps;
zsiz=zsiz-eps;
xb=x(x>xsiz);
xb=xb(1);
xc=x(x>wxa);
xc=xc(1);
delta_z=abs(z(2)-z(1));

za=z(z>wza);
za=za(1);
zb=z(z>zsiz);
zb=zb(1);

Bz=ones(length(z),1)*[zeros(1,length(x(x<-xc)))
((GxA*-xb)-xb/(xc-xb)*GxA*(xb+x(x>=-xc & x<=-xsiz)))
GxA*x(x>-xsiz & x<xsiz) ((GxA*xb)-xb/(xc-
xb)*GxA*(x(x>=xsiz & x<=xc)-xb))
zeros(1,length(x(x>xc)))];
Bz(zi>zsiz & zi<wza)=-zb/(za-zb)*Bz(zi>zsiz & zi<wza);
Bz(zi<-zsiz & zi>-wza)=-zb/(za-zb)*Bz(zi<-zsiz & zi>-
wza);
Bz(zi<-wza)=0;
Bz(zi>wza)=0;
```

Next the Fourier transform of the targeted field is computed to determine the targeted current distribution.

```
% Compute Fourier Transform of Target Field
Bk=fftshift(fft2(fftshift(Bz)));

% Define Frequency space points
Nx=length(x);
```

```
nx=-Nx/2:(Nx/2-1);
Nz=length(z);
nz=-Nz/2:(Nz/2-1);
kx1=nx*pi/wx;
kz1=nz*pi/wz;
[kx,kz]=meshgrid(kx1,kz1);
```

The frequency space of the targeted field is apodized by a Gaussian function, removing the high spatial frequency components, resulting in a smoother and physically realizable current density. Here, constants of z0 = 0.10 and x0 = 0.10 were selected. The targeted and apodized fields and the gradient along x are plotted, shown in Fig A.1.

```
% Apodize target field
z0=.010;
x0=.010;
Bk=Bk.*exp(-2*(x0^2*kx.^2+z0^2*kz.^2));
TargetB=real(ifftshift(ifft2(ifftshift(Bk))));
[Gx,Gz]=gradient(TargetB,abs(x(2)-x(1)),abs(z(2)-
z(1)));
n=size(TargetB,2)/64;
m=size(TargetB,1)/64;
x1=downsample(x,n);
z1=downsample(z,m);
TargetB1=downsample(downsample(TargetB',n)',m);
Gx1=downsample(downsample(Gx',n)',m);
figure;surf(x1*1000,z1*1000,TargetB1);title('Apodized
Target Field');xlabel('x (mm)');ylabel('z (mm)');
figure;subplot(311);plot(x*1000,Bz(size(Bz,1)/2,:),'Li
newidth',2)
hold on;plot(x*1000,TargetB(size(Bz,1)/2,:),'--
','Linewidth',2);xlabel('x (mm)');ylabel('B_z (T)');
subplot(312);plot((x(1:(length(x)-1))+abs(x(2)-
x(1))/2)*1000,diff(TargetB(size(Bz,1)/2,:))/abs(x(2)-
x(1)),'--','Linewidth',2);ylabel('G_x
(T/m)');xlabel('x (mm)');
hold on;plot((x(1:(length(x)-1))+abs(x(2)-
x(1))/2)*1000,diff(Bz(size(Bz,1)/2,:))/abs(x(2)-
x(1)),'Linewidth',2);ylabel('G_x (T/m)');xlabel('x
(mm)');
subplot(313);plot(z*1000,Bz(:,size(Bz,2)/2+1),'Linewid
th',2);
```

```
hold on;plot(z*1000,TargetB(:,size(Bz,2)/2+1),'--
','Linewidth',2);xlabel('z (mm)');ylabel('B_z (T)');

figure;surf(x1*1000,z1*1000,Gx1);title('Apodized
Target Gradient');xlabel('x (mm)');ylabel('z (mm)')

plotsize=3.5e-2;
surf(z(z>-plotsize & z<plotsize)*1000,x(x>-plotsize &
x<plotsize)*1000,Gx(x>-plotsize & x<plotsize,z>-
plotsize & z<plotsize)*10000/100);ylabel('z
(mm)','FontSize',14);xlabel('x
(mm)','FontSize',14);zlabel('G_x
(G/cm/A)','FontSize',14);title('Apodized Target
Field','FontSize',14);
text(-20,-20,min(min(Gx(x>-plotsize & x<plotsize,z>-
plotsize & z<plotsize)*10000/100)),['Min/Max ='
num2str(min(min(Gx(x>-plotsize & x<plotsize,z>-
plotsize & z<plotsize)))/max(max(Gx(x>-plotsize &
x<plotsize,z>-plotsize &
z<plotsize))),'%6.3f')],'FontSize',14);
%%
```

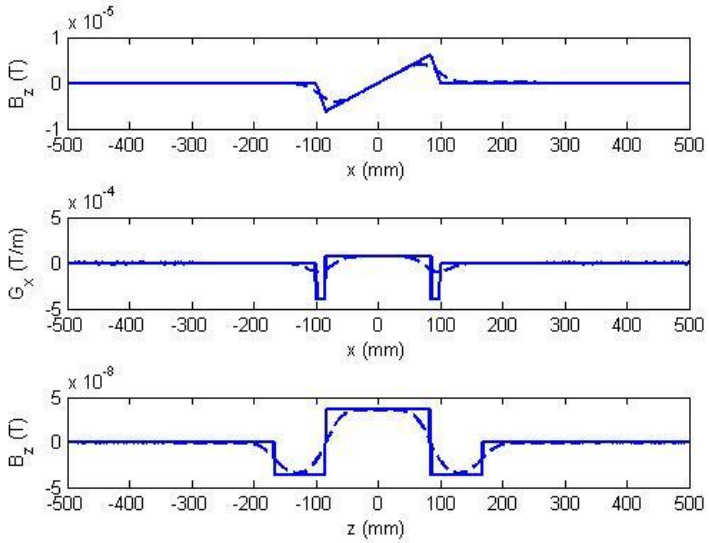

Fig. A.1. Target z-directed magnetic field and its gradient along x (top and middle, respectively) and z-directed magnetic field along z (bottom) produced by the fourth gradient coil. The solid lines are the desired field before apodization and the dashed lines show after apodization. Along x, the field begins returning to zero in a linear fashion beyond x = 8.4 cm, reaching zero at x = 10 cm. Along z, the field reverses beyond z = 8.4 cm and returns to zero at z = 16.8 cm.

The Fourier transform of the target field is then used to solve for the Fourier transform of the current density at the target plane y.

```
% Compute FT of current density generating target
field

jx=Bk./(-u0.*exp(-
a.*sqrt(kx.^2+kz.^2)).*sinh(y.*sqrt(kx.^2+kz.^2))-
eps);
```

The inverse Fourier transform is then computed, giving the x-directed current density yielding the target z directed magnetic field:

```
%Take inverse FT of jx to find current density Jx
Jx=ifftshift(ifft2(ifftshift(jx)));
```

The current density is integrated, yielding a stream function, psi, which is used to solve for a cutting pattern:

```
% Compute stream function

deltaz=abs(z(2)-z(1));
deltax=abs(x(2)-x(1));

psi=-cumtrapz(Jx)*deltaz;
psi=psi-
ones(length(z),1)*(psi(length(z),:)+psi((1),:))/2;

figure;imagesc(x*100,z*100,psi);axis image;axis
xy;colorbar

[Gxa,Gza]=gradient(psi,abs(x(2)-x(1)),abs(z(2)-z(1)));

%Plotting
figure;
subplot(121);imagesc(x*100,z*100,Jx);xlabel('x
(cm)');ylabel('z (cm)');title('x current density
(A/m)');axis image;axis xy;colorbar
subplot(122);imagesc(x*100,z*100,Gxa);xlabel('x
(cm)');ylabel('z (cm)');title('z current density
(A/m)');axis image;axis xy;colorbar
```

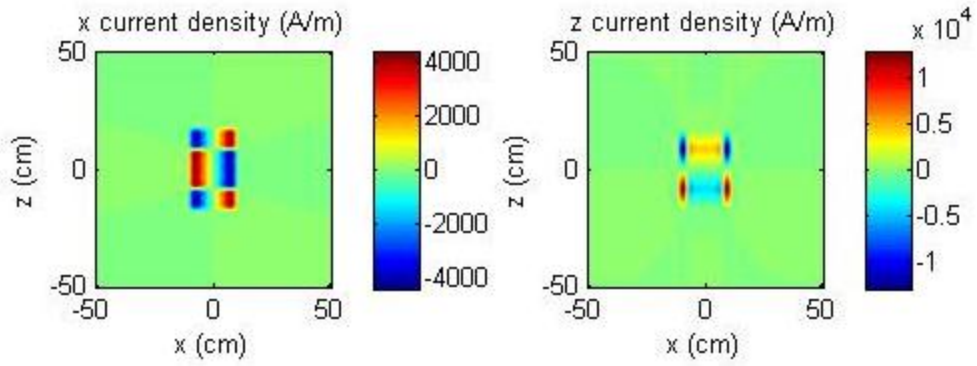

Fig. A.2. Current densities producing the target field. The x component (left) and z component (right) of the current densities at the y = ±4 cm planes which generate the desired (target) z-directed magnetic field at the y = 0.1 mm plane.

MATLAB's built in "contour" function is used to solve for equally-spaced contours in the stream function, which are used to generate a cutting pattern for the gradient coil. The contours are output as a set of points connecting arc segments forming the contour plot.

```
Num_contours=turns*2-1;
contours=linspace(-
max(max(psi)),max(max(psi)),Num_contours+2);
contours1=contours(2:(length(contours)-1));
figure;cutting=contour(x,z,psi,contours1,'LineWidth',2
,'linecolor','b');axis image;grid on;
axis([-.114 .114 -.20 .20]);
contours2=contours(2:length(contours))-
abs(contours(2)-contours(1))/2;
hold
on;C=contour(x,z,psi,contours2,'LineStyle',':','LineWi
dth',1,'linecolor','r');
xlabel('x (cm)','FontSize',14);ylabel('z
(cm)','FontSize',14);title('Cutting
Pattern','FontSize',14);
set(gca,'FontSize',14);
Ic=2*max(max(psi))/(2*turns);
legend('Cutting','Modeling','location','EastOutside');
```

The calculated winding (simulation) pattern and cutting pattern are saved as the matricies "C" and "cutting".

```
% save('Jx','Jx','x','z')
save('C','C','Ic');
save('cutting','cutting');
```

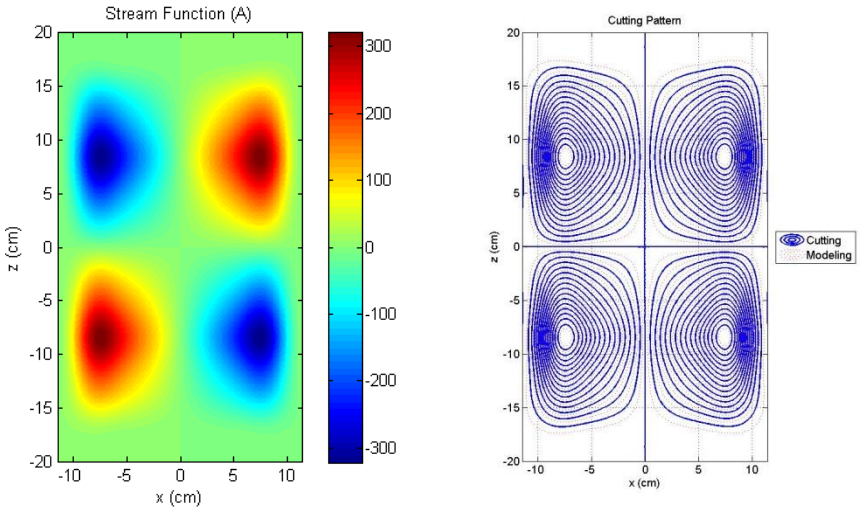

Fig. A.3. Stream function and contour plot. The stream function (left), calculated by integrating the current density in Fig. A.2, and a contour plot of the stream function (right) are shown. The contour plot provides either a cutting pattern (in blue) or a winding pattern (or Modeling – in red), depending on the type of coil being constructed. The winding pattern is useful for simulating the fields.

A.2. Simulation of Fields

The winding (simulation) pattern is then input into another MATLAB script implementing the Biot-Savart law, as shown. The contours of the "simulation" pattern are located at the center of each trace formed by the "cutting" pattern, giving an approximation of the fields produced by the actual structure. The matrix of points, C, is loaded and converted to the matrix of arcs, A, which contains the start-point of each arc segment (X1, Y1, Z1), the stop point of each arc segment (X2, Y2, Z2) and the current of each segment, I.

```
%%
clear all;clc
u0=4*pi*10^-7;
load C
r=1;
```

```
n=1;
p=1;
% arclength=zeros(2,1);
while n<(length(C)+1)
    points=C(2,n);
    B=C(:,(n+1):(n+points));
    D=[B(1,1:(length(B)-1))' B(2,1:(length(B)-1))'
B(1,2:length(B))' B(2,2:length(B))'];
    arclength(p)=sum(sqrt((D(:,1)-D(:,3)).^2+(D(:,2)-
D(:,4)).^2));
    A1((n:(n+points-2))-2*(p-1),:)=D;
    n=n+points+1;
    p=p+1;
end

ybot=-4e-2;

Atop=[A1(:,1) ybot*ones(size(A1,1),1) A1(:,2) A1(:,3)
ybot*ones(size(A1,1),1) A1(:,4)
Ic*ones(size(A1,1),1)];

Abot=[A1(:,1) -ybot*ones(size(A1,1),1) A1(:,2) A1(:,3)
-ybot*ones(size(A1,1),1) A1(:,4)
Ic*ones(size(A1,1),1)];

A=[Atop
    Abot];
```

Here the calculation points are specified. In this example, the z directed magnetic field at the y = 0.1 mm target plane is calculated over x = ±3.5 cm and z = ±3.5 cm.

```
% Solve over
x=linspace(-3.5e-2,3.5e-2,64);
y=-.1e-3;
z=linspace(-3.5e-2,3.5e-2,64);
[X,Y,Z]=meshgrid(x,y,z);
P=zeros(length(x),length(z),3);
P(:,:,1)=X;
P(:,:,2)=Y;
P(:,:,3)=Z;

B_field_x=zeros(size(x,2),size(z,2));
```

```
B_field_y=zeros(size(x,2),size(z,2));
B_field_z=zeros(size(x,2),size(z,2));
for p=1:size(A,1)
    start=zeros(length(x),length(z),3);
    stop=zeros(length(x),length(z),3);
    o=ones(length(x),length(z));
    start(:,:,1)=o*A(p,1);
    start(:,:,2)=o*A(p,2);
    start(:,:,3)=o*A(p,3);
    stop(:,:,1)=o*A(p,4);
    stop(:,:,2)=o*A(p,5);
    stop(:,:,3)=o*A(p,6);
    I=A(p,7);
    norm_PminStart=sqrt((P(:,:,1)-
start(:,:,1)).^2+(P(:,:,2)-start(:,:,2)).^2+(P(:,:,3)-
start(:,:,3)).^2);
    norm_StopminStart=sqrt((stop(:,:,1)-
start(:,:,1)).^2+(stop(:,:,2)-
start(:,:,2)).^2+(stop(:,:,3)-start(:,:,3)).^2);
    norm_PminStop=sqrt((P(:,:,1)-
stop(:,:,1)).^2+(P(:,:,2)-stop(:,:,2)).^2+(P(:,:,3)-
stop(:,:,3)).^2);
    cos_alpha2=dot(stop-start,P-
start,3)./(norm_StopminStart.*norm_PminStart);
    cos_alpha1=dot(stop-start,P-
stop,3)./(norm_StopminStart.*norm_PminStop);
    rho=norm_PminStart.*sin(acos(cos_alpha2));
    B_phi=u0*I./(4*pi.*rho).*(cos_alpha2-cos_alpha1);
    d=cross(P-start,stop-start,3);
    normd=zeros(size(d));

normd(:,:,1)=sqrt(d(:,:,1).^2+d(:,:,2).^2+d(:,:,3).^2)
;

normd(:,:,2)=sqrt(d(:,:,1).^2+d(:,:,2).^2+d(:,:,3).^2)
;

normd(:,:,3)=sqrt(d(:,:,1).^2+d(:,:,2).^2+d(:,:,3).^2)
;
    direction=cross(P-start,stop-start,3)./normd;
    B_field_x=B_field_x+B_phi.*direction(:,:,1);
    B_field_y=B_field_y+B_phi.*direction(:,:,2);
    B_field_z=B_field_z+B_phi.*direction(:,:,3);
end
```

Finally, the calculated z-directed field and its x gradient are displayed as surface plots.

```
%%
close all;
figure;surf(z*1000,x*1000,B_field_z*10000);ylabel('x
(mm)');xlabel('z (mm)');zlabel('B_z (G/A)');

[Gz,Gx]=gradient(B_field_z,abs(z(2)-z(1)),abs(x(2)-
x(1)));
figure;surf(x*1000,z*1000,rot90(Gx)*10000/100);ylabel(
'z (mm)','FontSize',14);xlabel('x
(mm)','FontSize',14);zlabel('G_x
(G/cm)','FontSize',14);
set(gca,'FontSize',12);
text(-20,-20,min(min(Gx*10000/100)),['Min/Max ='
num2str(min(min(Gx))/max(max(Gx)),'%6.2f')],'FontSize'
,14);
```

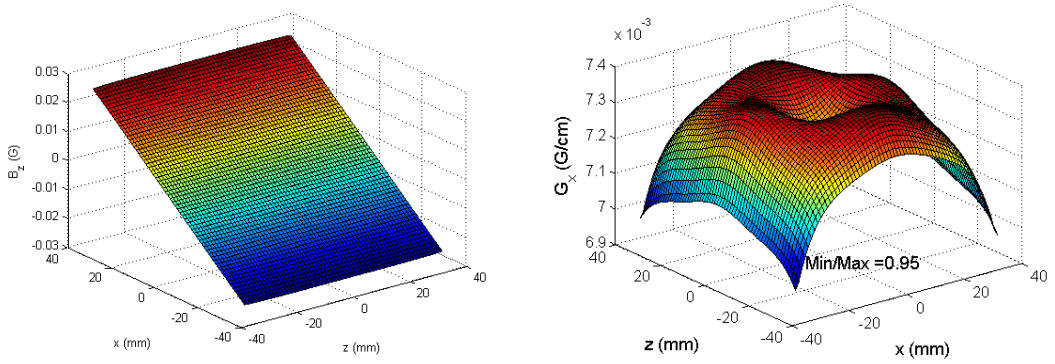

Fig. A.4. Field and gradient calculated by a Biot-Savart simulation of the arc segments of which the contour plot is composed. The number of arcs used was 41,056.

The ratio of the minimum to the maximum gradient field in the simulated region gives an estimate of the linearity of the coil. To generate the final coil geometry, the various parameters discussed in Section 1 are varied and the simulation repeated until a satisfactory result was obtained. Design of the coil is an iterative process of modifying parameters and calculating the resulting field.

A.3. Construction

The calculated cutting pattern is then converted to a format acceptable by the Protel circuit board design software using a MATLAB function called PcbAsciiFile.m written by Ke Feng (jnfengke@gmail.com). First, the output of the contour function is converted to a different format,

```
clear all;close all;clc
load cutting
r=1;
n=1;
p=1;
while n<(length(cutting)+1)
    points=cutting(2,n);
    B=cutting(:,(n+1):(n+points));
    D=[B(1,1:(length(B)-1))'      B(2,1:(length(B)-1))'
B(1,2:length(B))' B(2,2:length(B))'];
    A((n:(n+points-2))-2*(p-1),:)=D;
    n=n+points+1;
    p=p+1;
end
save('A')
```

The set of start and stop points in A are offset from the origin and then multiplied by a constant converting meters to mils. A PCB file is then generated which can be opened by the Protel software.

```
clear all;close all;clc;
% Contours to Ascii
load A
A=A+1;
A=A*39370.0787;
pcb=PcbAsciiFile('finger2.pcb');
for i=1:size(A,1);
    pcb.OutputLine(A(i,1),A(i,2),A(i,3),A(i,4),1);
end
pcb.Close
```

Once opened in the Protel circuit board design software, jogs are manually added to connect the concentric current paths. Also, the pattern is copied to occupy both sides of the boards. The pattern is used as the cutting layer and is milled into 4 oz double sided copper clad boards purchased from Injectorall Electronics Corp., Bohemia, NY.

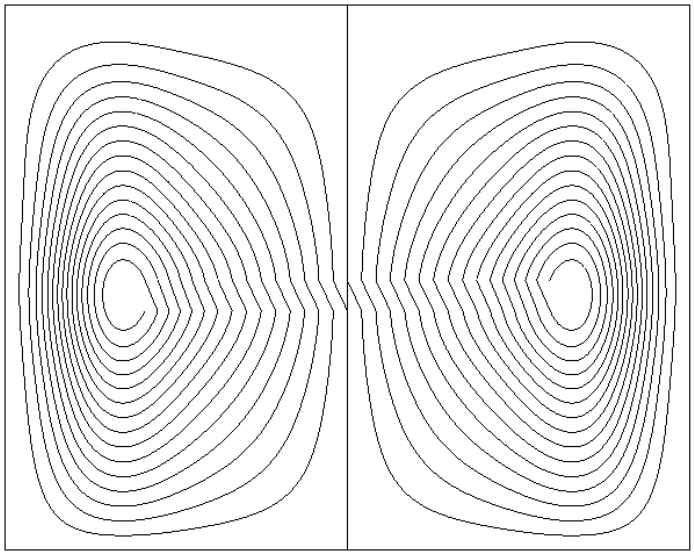

Fig. A.5. Cutting pattern from the PCB editing software. Jogs have been manually added to connect the concentric current rings generated by the contour plot. Due to symmetry, this double-sided board is milled four times to realize the biplanar gradient coil. The top and bottom layers are connected by vias at the center of the patterns.

k-space

The printed circuit boards are then assembled in a number of ways. For the implementation in this work, they were epoxy glued to additional sheets of unclad FR-4 and mounted to an acrylic former. However, a more mechanically rigid coil could be constructed by mounting the board segments to a former which could be cast in a thermally conductive epoxy resin. Coaxial cable was used to provide the input current to the PCB segments, although thicker wire would be better for higher duty cycles. Finally,

verification can be performed by MR imaging. A reference phase image from a spin-echo pulse sequence followed by a phase image with the inclusion of a pulse of the fourth gradient can be used to quantify the fourth gradient strength over the extent of the sample. The two phase images are subtracted (or the complex data are divided), giving the phase imparted by the fourth gradient pulse.